ELECTRONIC STRUCTURE AND SPECTRA OF FEW-ELECTRON QUANTUM DOTS

A Thesis
Presented to
The Academic Faculty

by

Yuesong Li

In Partial Fulfillment
of the Requirements for the Degree
Doctor of Philosophy in the
School of Physics

Georgia Institute of Technology
August 2007

ELECTRONIC STRUCTURE AND SPECTRA OF FEW-ELECTRON QUANTUM DOTS

Approved by:

Professor Uzi Landman,
Committee Chair
School of Physics
Georgia Institute of Technology

Professor Constantine Yannouleas
School of Physics
Georgia Institute of Technology

Professor Mei-Yin Chou
School of Physics
Georgia Institute of Technology

Professor Michael Pustilnik
School of Physics
Georgia Institute of Technology

Professor Minqiang Li
College of Management
Georgia Institute of Technology

Date Approved: 15 May 2007

ACKNOWLEDGEMENTS

I'd like to thank Professor Uzi Landman for the opportunity to work in his group in Georgia Tech. And I really appreciate him for his advice for my career and life. The experience in the group will greatly help me in my future work.

Also I'd like to thank Dr. Constantine Yannouleas for so much help in my research. I really enjoyed to work with him.

In the end, I want to thank all the people in the group for all the happy time.

TABLE OF CONTENTS

LIST OF TABLES

LIST OF FIGURES

xii

CHAPTER I

INTRODUCTION

1.1 Quantum dots in a simplified independent-particle picture

In this section and the next one, we give a brief review about quantum dots, emphasizing the general physical picture. In doing so, we follow closely the introduction part of the article *Few-electron quantum dots* by L.P. Kouwenhoven, D.G. Austing and S. Tarucha [1]. Quantum dots are small man-made structures in a solid, typically with sizes ranging from nanometers to a few microns. They consist of $10^3 - 10^9$ atoms with an equivalent number of electrons. In semiconductors all electrons are tightly bound to the nuclei except for a small fraction of free electrons. This small number can be anything from a single free electron, to a puddle of several thousands, in quantum dots defined in a semiconductor. Current nanofabrication technology allows us to precisely control the size and shape of these dots. The electronic properties of dots show many parallels with those of atoms. Most notably, the confinement of the electrons in all three spatial directions results in a quantized energy spectrum. Quantum dots are therefore regarded as artificial atoms [2]. For quantum dots that are fabricated between the source and drain electrical contacts, current-voltage measurements are used to observe the atom-like properties of the quantum dot. In addition, it is possible to vary the exact number of electrons on the dot by changing the voltage applied to a nearby gate electrode. This control allows one to scan through the entire periodic table of artificial elements by simply changing the voltage.

The symmetry of a quantum dot is the source of degeneracies in the energy spectrum. The three-dimensional spherically symmetric potential around atoms yields

degeneracies known as the shells, $1s, 2s, 2p, 3s, 3p, \ldots$ The electronic configuration is particularly stable when these shells are completely filled with electrons, occurring at the atomic numbers of $2, 10, 18, 36, \ldots$. These are the magic numbers of a three-dimensional spherically symmetric potential. Up to atomic number 23 the atomic shells are filled sequentially by electrons in a simple manner (mixing between levels originating from different shells starts at atomic number 24). Within a shell, Hund's rule determines whether a spin-down or a spin-up electron is added [3].

The confinement potential of dots can, to some extend, be chosen at specific requirement such as parabolic or elliptical potential. we will mainly consider the parabolic potential, which has the highest degree of symmetry, and elliptical potential, which will confine electrons to lie on a line, particularly under specific magnetic field. For parabolic confinement, the quantum dot is inside the pillar and has the shape of a two-dimensional disc [4, 5]. The attractive confinement potential is rather soft and can be approximated by a harmonic potential. (This r^2-dependence, instead of the $1/r$ attractive potential in atoms, has several consequences for the energy spectrum and relaxation times [6].) The symmetry of such a two-dimensional cylindrically symmetric, harmonic potential leads to a two-dimensional shell structure with the magic numbers $2, 6, 12, 20, \ldots$. Note that the lower degree of symmetry in two-dimensional structures leads to a lower magic number sequence.

We first introduce the central ideas related to atomic-like properties and explain how these are observed in single-electron transport. In this introductory chapter, we discuss these issues in a qualitative and phenomenological manner. A quantitative discussion is given in later chapters. Electron tunnelling from the source to the dot and from the dot to the drain is dominated by an essentially classical effect that arises from the discrete nature of charge. When relatively high potential barriers separate the dot from the source and drain contacts, tunnelling to and from the dot is weak and the number of electrons on the dot, N, will be a well defined integer. A

current flowing via a sequence of tunneling events of single electrons through the dot requires this number to fluctuate by one. The Coulomb repulsion between electrons on the dot, however, results in a considerable energy cost for adding an extra electron charge. Extra energy is therefore needed, and no current will flow until increasing the voltage provides this energy. This phenomenon is known as Coulomb blockade [7, 8]. In one scenario, the quantum dot is located in the center of the pillar and can hold up to $N = 100$ electrons. The diameter of the dot is a few hundred nanometers and its thickness is about 10 nm. The dot is sandwiched between two non-conducting barrier layers, which separate it from conducting material above and below, i.e. the source and drain contacts. A negative voltage applied to a metal gate around the pillar squeezes the diameter of the dot's lateral potential. This reduces the number of electrons, one by one, until the dot is completely empty.

Due to the Coulomb blockade, the current can flow only when electrons in the electrodes have sufficient energy to occupy the lowest possible energy state for $N + 1$ electrons on the dot. By changing the gate voltage, the ladder of the dot states is shifted through the Fermi energies of the electrodes. This leads to a series of sharp peaks in the measured current. At any given peak, the number of electrons alternates between N and $N + 1$. Between the peaks, the Coulomb blockade keeps N fixed and no current can flow. The distance between consecutive peaks is proportional to the so-called addition energy, E_{add}, which is the energy difference between the transition points of (N to $N + 1$) and ($N + 1$ to $N + 2$) electrons. Compared to atomic energy, the addition energy for a dot is equal to the difference between the ionization energy and the electron affinity [9]. The simplest model for describing the energetics is the constant-interaction (CI) model [7, 8], which crudely assumes that the Coulomb interaction between the electrons is independent of N. In this model, the addition energy is given by $E_{add} = e^2/C + \Delta E$, where ΔE is the energy difference between consecutive quantum states. The Coulomb interactions are represented as a

charging energy, e^2/C, of a single electron charge, e, on a capacitor C.

Despite its simplicity, this model is remarkably successful in providing an elementary understanding. The first peak marks the energy at which the first electron enters the dot, the second records the entry of the second electron and so on. The spacing between peaks, measured in gate voltage, is directly proportional to the addition energy. Note that the spacing is not constant and significantly more energy is needed to add an electron to a dot with 2, 6 and 12 electrons i.e. the first few magic numbers for a two-dimensional circular harmonic potential.

The orbit with the smallest radius corresponds to the lowest energy state. This state has zero angular momentum and, as the s-states in atoms, can hold up to two electrons with opposite spin. The addition of the second electron thus only costs the charging energy, e^2/C. Extra energy, is needed to add the third electron since this electron must go into the next energy state. Electrons in this orbit have an angular momentum ± 1 and two spin states so that this second shell can contain four electrons. The sixth electron fills up this shell so that extra energy is again needed to add the seventh electron.

In atomic physics, Hund's rule states that a shell is first filled with electrons with parallel spins until it is half full. After that, filling continues with anti-parallel spins. In the case of two-dimensional artificial atoms, the second shell is half-filled when $N = 4$. This maximum spin state is reflected by a somewhat enhanced peak spacing, or addition energy. Half filling of the third and forth shells occur for $N = 9$ and $N = 16$. These phenomena can be summarized in a periodic table for two-dimensional elements.

Quantum dots have been shown to provide a two-dimensional analogy for real atoms. Due to their larger dimensions, dots are suitable for experiments that cannot be carried out in atomic physics. It is especially interesting to observe the effect of a magnetic field, $\mathbf{B}$, on the atom-like properties. A magnetic flux-quantum in an atom

typically requires a B-field as high as 10^6 T, whereas for dots this is of order 1 T. (A flux quantum is $h/e = BA$, where A is the area of the dot.) The scale of a flux-quantum corresponds to a considerable change in the shape of the orbits. The change in orbital energy is roughly $\hbar eB/m^*$ (the cyclotron frequency is $\omega_c = eB/m^*$), which is as much as $1.76 meV/T$, in GaAs due to the small effective mass $m^* = 0.067 m_e$. A magnetic field has, on the other hand, a negligible effect on the Zeeman spin splitting, $g\mu_B B$, which is only about $0.025 meV/T$ in GaAs, since $g_{GaAs} = -0.44$. A magnetic field therefore is about 70 times more effective for changing the orbital energy than for changing the Zeeman spin splitting in GaAs. Therefore, the Zeeman spin splitting can be neglected in most calculations; the Zeeman splitting contribution can be added at the end as a perturbative term. However, the spin may play an important role via Hund's rule. The associated energy is the exchange energy between electrons with parallel spins. This model, which treats the quantum states, the direct Coulomb interaction and the exchange interaction separately provides a good introduction to the physics of interacting particles. *However, it should be emphasized that this picture is approximate and the true many-body nature requires a higher-level theory as the one described in the following chapters of this thesis. When we understand the interactions between a small number of electrons we can gradually increase N and see how many-body effects develop* .

1.2 Constant-interaction model

As aforementioned, the CI model provides an approximate description of the electronic states of quantum dots, and was used by experimentists as a guide to the interpretation of early experiments. The CI model is based on two important assumptions. First, the Coulomb interactions of an electron on the dot with all other electrons, in and outside the dot, are parametrized by a constant capacitance C. Second, the discrete, single-particle energy spectrum, calculated for non-interacting

electrons, is unaffected by the interactions. The CI model approximates the total ground state energy, $U(N)$, of an N-electron dot by

$$U(N) = [e(N - N_o) - C_gV_g]^2/2C + \sum_N E_{n,l}(B), \qquad (1)$$

where $N = N_o$ for $V_g = 0$. The term C_gV_g is a continuous variable and represents the charge induced on the dot by the gate voltage, V_g, through the gate capacitance, C_g. The total capacitance between the dot and the source, the drain and the gate is $C = C_s + C_d + C_g$. The last term in equation (1) is a sum over the occupied states, $E_{n,l}(B)$, which are the solutions to the single-particle Schrödinger equation described in the next section. Note that only thes single-particle states depend on the magnetic field.

The electrochemical potential of the dot is defined as $\mu_{dot}(N) = U(N) - U(N-1)$. Electrons can flow from left to right when μ_{dot} is between the potentials, μ_{left} and μ_{right}, of leads (with $eV_{sd} = \mu_{left} - \mu_{right}$, $\mu_{left} > \mu_{dot}(N) > \mu_{right}$. For small volt $V_{sd} \approx 0$, the Nth Coulomb peak is a direct measure of the lowest possible energy state of a N-electron dot. From equation (1), we obtain

$$\mu_{dot} = (N - N_o - 1/2)E_c - e(C_g/C)V_g + E_N. \qquad (2)$$

The addition energy is given by

$$\Delta\mu(N) \;=\; \mu_{dot}(N+1) - \mu_{dot}(N) = U(N+1) - 2U(N) + U(N-1) \qquad (3)$$

$$\;=\; E_c + E_{N+1} - E_N = e^2/C + \Delta E. \qquad (4)$$

with E_N being the topmost filled single-particle state for an N electrons dot. The related atomic energies are defined $A = U(N) - U(N+1)$ for the electron affinity and $I = U(N-1) - U(N)$ for the ionization energy [9]. Their relation to the addition energy is $\Delta\mu_N = I - A$.

The electrochemical potential is linearly proportional to the gate voltage with the proportionality factor $\alpha = (C_g/C)$ (equation 2). The α-factor also relates the peak

spacing in the gate voltage to the addition energy: $\Delta\mu_N = e\alpha(V_g^{N+1} - V_g^N)$, where V_g^N and V_g^{N+1} are the gate voltages of the Nth and $N+1$ Coulomb peaks, respectively.

1.3 Circular quantum dots at high magnetic field: the many-body problem

Due to the growing interest in solid-state nanostructures, driven by basic research and potential technological considerations, two-dimensional N-electron semiconductor quantum dots (QDs) in field-free conditions and under applied magnetic fields (B) have been extensively studied in the last few years, both experimentally [10, 11, 12] and theoretically. [13, 14, 15, 16, 17, 18] Experimentally, the case of parabolic QDs with a small number of electrons ($N \leq 30$) has attracted particular attention, as a result of precise control of the number of electrons in the dot that has been demonstrated in several experimental investigations.

In previous sections, we reviewed a simplified theory of quantum dots, known as the constant-interaction model. Naturally, QDs with a small number of electrons are also most attractive for more sophisticated theoretical investigations, e.g, since their ground-state properties and excitation spectra can be analyzed [13, 14, 15, 16, 17, 19, 20, 21] through exact-diagonalization (EXD) solutions of the many-body Schrödinger equation, where the Coulomb interaction is explicitly included. The hamiltonian is given as

$$H = \sum_{i=1}^{N} H_{\mathrm{sp}}(i) + \sum_{i=1}^{N}\sum_{j>i}^{N} \frac{e^2}{\kappa r_{ij}}, \tag{5}$$

with

$$H_{\mathrm{sp}}(i) = \frac{1}{2m^*}\left(\mathbf{p}_i - \frac{e}{c}\mathbf{A}_i\right)^2 + \frac{m^*}{2}\omega_0^2 \mathbf{r}_i^2, \tag{6}$$

being the single-particle part. The hamiltonian H describes N electrons (interacting via a Coulomb repulsion) confined by a parabolic potential of frequency ω_0 and subjected to a perpendicular magnetic field B, whose vector potential is given in the symmetric gauge by $\mathbf{A}(\mathbf{r}) = \frac{1}{2}(-By, Bx, 0)$. m^* is the effective electron mass, κ is the

dielectric constant of the semiconductor material, and $r_{ij} = |\mathbf{r}_i - \mathbf{r}_j|$. For sufficiently high magnetic fields, the electrons are fully spin-polarized and the Zeeman term [not shown in Eq. (5)] does not need to be considered. [22] Thus the calculations in this paper do not include the Zeeman contribution, which, however, can easily be added (for a fully polarized dot, the Zeeman contribution to the total energy is $Ng^*\mu_B B/2$, with g^* being the effective Landé factor and μ_B the Bohr magneton).

In particular, in combination with certain approximate methods, which are less demanding computationally while providing highly accurate results and a transparent physical picture (e.g., the method of successive hierarchical approximations, [16, 18] see below), EXD calculations confirmed the spontaneous formation of finite rotating electron molecules (REMs) and the description of the excited states with magic angular momenta as yrast rotational bands of these REMs [16] (sometime the REMs are referred to as "rotating Wigner molecules," RWMs). However, the number of Slater determinants in the EXD wave-function expansion increases exponentially as a function of N, and as a result EXD calculations to date have been restricted to rather low values of N, typically with $N \lesssim 10$; this has prohibited investigation of REMs with multiple rings. A similar problem appears also with other wave functions that are expressed as a discrete sum over Slater determinants, such as the *analytic* REM wave functions (see Eq. (55, 57)), or the variational Monte Carlo approach of Ref. [23].

Most EXD calculations (see, e.g., Refs. [13], [16](b), [19, 20, 24]) have been carried out in the regime of very strong magnetic field (i.e., $B \to \infty$), such that the Hilbert space can be restricted to the lowest Landau level (LLL); in this regime, the confinement does not have any influence on the composition of the microscopic many-body wave function (see section 2.2.2). EXD calculations as a function of B that include explicitly the full effect of the confinement, [14, 15, 17, 21] i.e., mixing with higher Landau levels are more involved, and thus they are scarce and are usually restricted

to very small sizes with $N \leq 4$. An exception is presented by the method of hyper-spherical harmonics, [14, 15] which, however, may not be reliable for all the sizes up to $N \sim 10$.

In this thesis, we focus on the EXD method and the REM variational method. Of course, there are other many-body methods such as Variational Quantum Monte Carlo (QMC), path integral QMC and Composite Fermion.

1.4   Three-electron anisotropic quantum dots at low magnetic field from a quantum information perspective

Three-electron quantum dots are expected to attract a lot of attention in the near future due to several developments, both experimental and theoretical. First, it was recently experimentally demonstrated[25, 26] that detailed excitation spectra of two-electron quantum dots (in addition to earlier ground-state measurements[27, 28]) can be measured as a function of the externally applied magnetic field. Thus, measuring the excitation spectra of three-electron quantum dots appears to be a next step to be taken. Second, three-qubit electron spin devices are expected to exhibit enhanced efficiency[29, 30, 31] for quantum-computing purposes compared to single-qubit and two-qubit ones.

In this part, we carry out exact diagonalization (EXD) studies for a three-electron single quantum dot under low and moderate magnetic fields. Unlike previous EXD studies[32, 33] that focused mainly on the ground states of circular quantum dots, we investigate, in addition, the excitation spectra for three electrons in quantum dots with a wide range of anisotropies. Furthermore, consideration of anisotropic quantum dots allows us to investigate the structure of the many-body wave functions with respect to electron localization and formation of Wigner molecules in a linear geometry. In particular, we investigate the feasibility of generating model quantum entangled states (i.e., the so called W states[31, 34, 35]), which are often employed

in the mathematical treatment of quantum information and which have been experimentally realized with atoms in linear ion traps.[36] We note that a main factor motivating our investigations is the different nature of the entangling agent, namely, the electromagnetic field in the case of heavy ions versus the two-body Coulomb interaction in the case of electrons.

1.5 Scope of the thesis

In the first part of the thesis, we develop a variational method, the rotating electron molecule (REM), for the investigations of the energetic, structural, and excitation properties of circular quantum dots (QD) in strong magnetic fields with an arbitrary number of electrons ($2 \leq N \leq 30$). We perform comparative calculations for quantum dots with an increasing number of parabolically confined electrons ($N = 3, 4, 6, 9, 11,$ and 17). We find that the electrons form concentric rings for the ground state, with each ring containing a certain number of electrons. Using the notation $(n_1, n_2, n_3, ...)$ for the number of electrons located on each ring, the ground-state arrangements are: (0,3) for $N = 3$, (0,4) for $N = 4$, (1,5) for $N = 6$, (2,7) for $N = 9$,(3,8) for $N = 11$, and (1,6,10) for $N = 17$. Comparison of our results to those obtained by the EXD method reveals that the REM method provides a highly accurate description of parabolically confined electrons in quantum dots for a wide range of applied magnetic fields, starting from the neighborhood of the maximum density droplet and extending to the $B \to \infty$ limit. The ground-state energy of the electrons in a QD oscillates as a function of the applied magnetic field, and the allowed values of the angular momenta are limited to a set of magic angular momentum values, L_m, which requires that the electrons are localized on concentric polygonal rings that rotate independently. The general expression for L_m is given in Eq. (9).

In the second part of the thesis, we present extensive EXD calculations for elliptical dots, double dots, and circular dots in the lowest Landau level. For three electrons

in elliptical quantum dots, we analyze the excitation spectra both as a function of the magnetic field and as a function of increasing anisotropy. A main finding is the appearance of triple-crossing points in the ground-state energy curves for stronger anisotropies. Through the spin-resolved conditional probability distributions (CPDs), we reveal that the electrons localize to form Wigner molecules in different shapes. For certain ranges of dot parameters (mainly at strong anisotropy), the Wigner molecules acquire a linear geometry, and the associated wave functions with a spin projection $S_z = 1/2$ are similar to the so called W-states that are a prototype of entangled states. For other ranges of parameters (mainly at moderate anisotropy), the Wigner molecules exhibit a more complex structure consisting of two mirror isosceles triangles. This latter structures can be considered as an embryonic unit of a zig-zag Wigner crystal in quantum wires. Also, we demonstrate that the degree of entanglement in three-electron quantum dots can be quantified via the von Neumann entropy, in analogy with studies on two-electron quantum dots.

We also examine the structures of two separated circular dots, at a distance of 70nm, that contain three electrons. Through the spin-resolved CPD, we find that the electrons are localized in the centers of the dots. The first two electrons localize at the centers of the dots, the third electron has a 50% probability to appear at each center.

Finally, we compare the results of Laughlin's method with EXD calculations for circular dots that contains 9 electrons in the LLL. While Laughlin's method states that the electrons are in a liquid state, EXD calculations clearly show that the electrons form Winger Molecules, which confirms our previous results by the REM method.

CHAPTER II

VARIATIONAL METHOD FOR PARABOLIC QUANTUM DOTS AT HIGH MAGNETIC FIELD

2.1   Introduction

2.1.1   Computational motivation

Systematic EXD calculations beyond the numerical barrier of $N \sim 10$ electrons are not expected to become feasible in the near future. In this paper, we show that a microscopic numerical method, which was introduced by us recently and is based on successive hierarchical approximations (with increasing accuracy after each step) is able to go beyond this barrier. This approach (referred to, for brevity, as the "two-step method") can provide high-quality calculations describing properties of QDs as a function of B in the whole size range $2 \le N \le 30$, *with (or without) consideration of the effect of the confinement on the mixing with higher Landau levels.* In this paper, we will consider the case of fully polarized electrons, which in typical GaAs experimental devices is appropriate for strong B such that the ground-state angular momentum $L \ge L_0 \equiv N(N-1)/2$.

The minimum value L_0 specifies the so-called maximum density droplet (MDD); its name results from the fact that it was originally defined [37] in the LLL where it is a single Slater determinant built out of orbitals with successive single-particle angular momenta 0,1,2, ..., $N-1$. We will show, however, that mixing with higher Landau levels is non-negligible for MDD ground states that are feasible in currently available experimental quantum dots; in this case the electron density of the MDD is not constant, but exhibits oscillations.

2.1.2   Nonclassical (non-rigid) rotational inertia

The existence of an exotic supersolid crystalline phase with combined solid and su-
perfluid characteristics has been long conjectured [38, 39, 40] for solid ^{4}He under
appropriate conditions. The recent experimental discovery [41] that solid ^{4}He ex-
hibits a nonclassical (nonrigid) rotational inertia (NCRI [40]) has revived an intense
interest [42, 43, 44, 45, 46] in the existence and properties of the supersolid phase in
this system, as well as in the possible emergence of exotic phases in other systems.

As we show here, certain aspects of supersolid behavior (e.g., the simultaneous
occurrence of crystalline correlations and non-rigidity under rotations) may be found
for electrons in quantum dots. As aforementioned, under a high magnetic field, the
electrons confined in a QD localize at the vertices of concentric polygonal rings and
form a rotating electron molecule. [16] We show that the corresponding rotational
inertia strongly deviates from the rigid classical value, a fact that endows the REM
with supersolid-like characteristics (in the sense of the appearance of a non-classical
rotational inertia, but without implying the presence of a superfluid component).
Furthermore, the REM at high B can be naturally viewed as the precursor of a
quantum crystal that develops in the lowest Landau level (LLL) in the thermodynamic
limit. Due to the lack of rigidity, the LLL quantum crystal exhibits a "liquid"-
like behavior. These conclusions were enabled by the development of an analytic
expression for the excitation energies of the REM that permits calculations for an
arbitrary number of electrons, given the classical polygonal-ring structure in the QD.
[47]

This chapter is organized as follows. Section 2.2 is devoted to a description of
computational methods for the properties of electrons in QDs under high magnetic
fields, with explicit consideration of effects due to the external confinement. In section
2.3, we compare results from various computationals methods with those obtained via
exact diagonalization. Illustrative examples of the formation of crystalline rotating

electron molecules with ground-state multiple concentric polygonal ring structures, and their isomers, are given in section 2.4 for QDs with $N = 6, 9, 11, 17$. The yrast band of rotational excitations (at a given B) is analyzed in section 2.5 along with the derivation of an analytic formula that provides for stronger fields (and/or higher angular momenta) accurate predictions of the energies of REMs with arbitrary numbers of electrons. In section 2.6, we discuss the non-rigid (liquid-like) characteristics of electrons in quantum dots under high magnetic fields as portrayed by their non-classical rotational inertia. We summarize our findings in section 2.7. For an earlier shorter version of this paper, see Ref. [48].

2.2 Description of computational methods that consider the external confinement

2.2.1 The REM microscopic method

In our method of successive hierarchical approximations, we begin with a *static* electron molecule (SEM), described by an unrestricted Hartree-Fock (UHF) determinant that violates the circular symmetry. [18] Subsequently, the *rotation* of the electron molecule is described by a post-Hartree-Fock step of restoration of the broken circular symmetry via projection techniques. [16, 18] Since we focus here on the case of strong B, we can approximate the UHF orbitals (first step of our procedure) by (parameter free) displaced Gaussian functions; that is, for an electron localized at $\mathbf{R}_j$ (Z_j), we use the orbital

$$u(z, Z_j) = \frac{1}{\sqrt{\pi}\lambda} \exp\left(-\frac{|z - Z_j|^2}{2\lambda^2} - i\varphi(z, Z_j; B)\right), \qquad (7)$$

with $\lambda = \sqrt{\hbar/m^*\Omega}$; $\Omega = \sqrt{\omega_0^2 + \omega_c^2/4}$, where $\omega_c = eB/(m^*c)$ is the cyclotron frequency and ω_0 specifies the external parabolic confinement. We have used complex numbers to represent the position variables, so that $z = x + iy$, $Z_j = X_j + iY_j$. The phase guarantees gauge invariance in the presence of a perpendicular magnetic field and is given in the symmetric gauge by $\varphi(z, Z_j; B) = (xY_j - yX_j)/2l_B^2$, with

14

$l_B = \sqrt{\hbar c/eB}$.

For an extended 2D system, the Z_j's form a triangular lattice. [49] For finite N, however, the Z_j's coincide [16, 18, 50] with the equilibrium positions [forming r concentric regular polygons denoted as $(n_1, n_2, ..., n_r)$] of $N = \sum_{q=1}^{r} n_q$ classical point charges inside an external parabolic confinement. [47] In this notation, n_1 corresponds to the innermost ring with $n_1 > 0$. For the case of a single polygonal ring, the notation $(0, N)$ is often used; then it is to be understood that $n_1 = N$.

The wave function of the *static* electron molecule (SEM) is a *single* Slater determinant $|\Psi^{\mathrm{SEM}}[z]\rangle$ made out of the single-electron wave functions $u(z_i, Z_i)$, $i = 1, ..., N$. Correlated many-body states with good total angular momenta L can be extracted [16] (second step) from the UHF determinant using projection operators. The projected REM state is given by

$$|\Phi_L^{\mathrm{REM}}\rangle = \int_0^{2\pi} ... \int_0^{2\pi} d\gamma_1...d\gamma_r$$
$$\times |\Psi^{\mathrm{SEM}}(\gamma_1, ..., \gamma_r)\rangle \exp\left(i \sum_{q=1}^{r} \gamma_q L_q\right). \tag{8}$$

Here $L = \sum_{q=1}^{r} L_q$ and $|\Psi^{\mathrm{SEM}}[\gamma]\rangle$ is the original Slater determinant with *all the single-electron wave functions of the qth ring* rotated (collectively, i.e., coherently) by the *same* azimuthal angle γ_q. Note that Eq. (8) can be written as a product of projection operators acting on the original Slater determinant [i.e., on $|\Psi^{\mathrm{SEM}}(\gamma_1 = 0, ..., \gamma_r = 0)\rangle$]. Setting $\lambda = l_B\sqrt{2}$ restricts the single-electron wave function in Eq. (7) to be entirely in the lowest Landau level [16] (see Appendix A). The continuous-configuration-interaction form of the projected wave functions [i.e., the linear superposition of determimants in Eq. (8)] implies a highly entangled state. We require here that B is sufficiently strong so that all the electrons are spin-polarized [22] and that the ground-state angular momentum $L \geq L_0 \equiv N(N-1)/2$ (or equivalently that the fractional filling factor $\nu \equiv L/L_0 \leq 1$).

Due to the point-group symmetries of each polygonal ring of electrons in the

SEM wave function, the total angular momenta L of the rotating crystalline electron molecule are restricted to the so-called *magic* angular momenta, i.e.,

$$L_m = L_0 + \sum_{q=1}^{r} k_q n_q, \tag{9}$$

where the k_q's are non-negative integers[51] (when $n_1 = 1$, $k_1 = 0$).

The partial angular momenta associated with the qth ring, L_q [see Eq. (8)], are given by

$$L_q = L_{0,q} + k_q n_q, \tag{10}$$

where $L_{0,q} = \sum_{i=i_q+1}^{i_q+n_q}(i-1)$ with $i_q = \sum_{s=1}^{q-1} n_s$ $(i_1 = 0)$, and $L_0 = \sum_{q=1}^{r} L_{0,q}$.

The energy of the REM state [Eq. (8)] is given[18, 50] by

$$E_L^{\mathrm{REM}} = \int_0^{2\pi} h([\gamma])e^{i[\gamma]\cdot[L]}d[\gamma] \Big/ \int_0^{2\pi} n([\gamma])e^{i[\gamma]\cdot[L]}d[\gamma], \tag{11}$$

with the hamiltonian and overlap matrix elements $h([\gamma]) = \langle \Psi^{\mathrm{SEM}}([0])|H|\Psi^{\mathrm{SEM}}([\gamma])\rangle$ and $n([\gamma]) = \langle \Psi^{\mathrm{SEM}}([0])|\Psi^{\mathrm{SEM}}([\gamma])\rangle$, respectively, and $[\gamma]\cdot[L] = \sum_{q=1}^{r} \gamma_q L_q$. The SEM energies are simply given by $E_{\mathrm{SEM}} = h([0])/n([0])$.

The many-body Hamiltonian is

$$H = \sum_{i=1}^{N} H_{\mathrm{sp}}(i) + \sum_{i=1}^{N}\sum_{j>i}^{N} \frac{e^2}{\kappa r_{ij}}, \tag{12}$$

with

$$H_{\mathrm{sp}}(i) = \frac{1}{2m^*}\left(\mathbf{p}_i - \frac{e}{c}\mathbf{A}_i\right)^2 + \frac{m^*}{2}\omega_0^2 \mathbf{r}_i^2, \tag{13}$$

being the single-particle part. The hamiltonian H describes N electrons (interacting via a Coulomb repulsion) confined by a parabolic potential of frequency ω_0 and subjected to a perpendicular magnetic field B, whose vector potential is given in the symmetric gauge by $\mathbf{A}(\mathbf{r}) = \frac{1}{2}(-By, Bx, 0)$. m^* is the effective electron mass, κ is the dielectric constant of the semiconductor material, and $r_{ij} = |\mathbf{r}_i - \mathbf{r}_j|$. For sufficiently high magnetic fields, the electrons are fully spin-polarized and the Zeeman term [not shown in Eq. (12)] does not need to be considered. [22] Thus the calculations in this

paper do not include the Zeeman contribution, which, however, can easily be added (for a fully polarized dot, the Zeeman contribution to the total energy is $Ng^*\mu_B B/2$, with g^* being the effective Landé factor and μ_B the Bohr magneton).

The crystalline polygonal-ring arrangement $(n_1, n_2, ..., n_r)$ of classical point charges is portrayed directly in the electron density of the broken-symmetry SEM, since the latter consists of humps centered at the localization sites Z_j's (*one hump* for each electron). In contrast, the REM has good angular momentum and thus its electron density is circularly uniform. To probe the crystalline character of the REM, we use the conditional probability distribution (CPD) defined as

$$P(\mathbf{r}, \mathbf{r}_0) = \langle\Phi| \sum_{i \neq j} \delta(\mathbf{r}_i - \mathbf{r})\delta(\mathbf{r}_j - \mathbf{r}_0)|\Phi\rangle/\langle\Phi|\Phi\rangle, \qquad (14)$$

where $\Phi(\mathbf{r}_1, \mathbf{r}_2, ..., \mathbf{r}_N)$ denotes the many-body wave function under consideration. $P(\mathbf{r}, \mathbf{r}_0)$ is proportional to the conditional probability of finding an electron at $\mathbf{r}$, given that another electron is assumed at $\mathbf{r}_0$. This procedure subtracts the collective rotation of the electron molecule in the laboratory frame of referenece, and, as a result, the CPDs reveal the structure of the many body state in the intrinsic (rotating) reference frame.

2.2.2 Exact diagonalization in the lowest Landau level

We describe here a widely used approximation[13, 19, 52] for calculating the ground state at a given B, which takes advantage of the simplifications at the $B \to \infty$ limit, i.e., when the relevant Hilbert space can be restricted to the lowest Landau level [then $\hbar\omega_0 << \hbar\omega_c/2$ (for $B \to \infty$) and the confinement can be neglected at a first step]. Then, the many-body hamiltonian [see Eq. (12)] reduces to

$$H_{\text{LLL}}^{B \to \infty} = N\frac{\hbar\omega_c}{2} + \sum_{i=1}^{N} \sum_{j>i}^{N} \frac{e^2}{\kappa r_{ij}}. \qquad (15)$$

Due to the form of the limiting Hamiltonian in Eq. (15), one can overlook the zero-point-energy term and perform an exact diagonalization only for the Coulomb

interaction part. The corresponding interaction energies can be written as

$$\widetilde{E}_{\mathrm{int,LLL}}^{\mathrm{EXD}}(L) = \widetilde{\mathcal{E}}_{\mathrm{int,LLL}}^{\mathrm{EXD}}(L)\frac{e^2}{\kappa l_B}, \tag{16}$$

where $\widetilde{\mathcal{E}}_{\mathrm{int,LLL}}^{\mathrm{EXD}}$ is dimensionless. The subscript "int" identifies the $e - e$ interaction as the source of this term.

In this approximation scheme, at finite B the external confinement $\hbar\omega_0$ is taken into consideration only through the lifting of the single-particle degeneracy within the LLL, while disregarding higher Landau levels. As a result, the effect of the confinement enters here only as follows: (I) in the interaction term [see Eq. (16)], one scales the effective magnetic length, i.e., one replaces l_B by $\lambda/\sqrt{2}$ (see section 2.2.1 for the definition of l_B and λ) without modifying the dimensionless part $\widetilde{\mathcal{E}}_{\mathrm{int,LLL}}^{\mathrm{EXD}}$, and (II) the contribution, $E_{\mathrm{sp}}^{n=0}(B,L)$ (referenced to $N\hbar\Omega$), of the single-particle hamiltonian $\sum_{i=1}^{N} H_{\mathrm{sp}}(i)$ to the total energy [see Eq. (12)] is added to $\widetilde{E}_{\mathrm{int,LLL}}^{\mathrm{EXD}}(L)$ [corresponding to the second term on the right-hand side of Eq. (12)]. $E_{\mathrm{sp}}^{n=0}(B,L)$ is the sum of Darwin-Fock single-particle energies $\epsilon_{n,l}^{\mathrm{DF}}$ with zero nodes ($n = 0$; the corresponding single-particle states become degenerate at $B \to \infty$ and form the lowest Landau level). Since

$$\epsilon_{n,l}^{\mathrm{DF}} = (2n + 1 + |l|)\hbar\Omega - l\hbar\omega_c/2, \tag{17}$$

the $E_{\mathrm{sp}}^{n=0}(B,L)$ is linear in the total angular momentum $L = \sum_{i=1}^{N} l_i$, i.e.,

$$E_{\mathrm{sp}}^{n=0}(B,L) = \hbar(\Omega - \omega_c/2)L. \tag{18}$$

Note that $E_{\mathrm{sp}}^{n=0}(B \to \infty, L) \to 0$.

We denote the final expression of this approximation by $\widetilde{E}_{\mathrm{tot,LLL}}^{\mathrm{EXD}}$; it is given by

$$\widetilde{E}_{\mathrm{tot,LLL}}^{\mathrm{EXD}}(B,L) = E_{\mathrm{sp}}^{n=0}(B,L) + \sqrt{2}\widetilde{\mathcal{E}}_{\mathrm{int,LLL}}^{\mathrm{EXD}}(L)\frac{e^2}{\kappa\lambda}. \tag{19}$$

An approximate ground-state energy for the system can be found through Eq. (19) by determining the angular-momentum value L_{gs} that minimizes this expression. In

18

the following, this ground-state energy at a given B will be denoted simply by omitting the variable L on the left-hand-side of Eq. (19), i.e., $\widetilde{E}_{\mathrm{tot,LLL}}^{\mathrm{EXD}}(B) \equiv \widetilde{E}_{\mathrm{tot,LLL}}^{\mathrm{EXD}}(B, L_{\mathrm{gs}})$.

We note that, although few in number, full EXD calculations for finite B that take into consideration both the confinement $\hbar\omega_0$ and the actual complexity of the Darwin-Fock spectra (including levels with $n > 0$) have been reported [14, 15, 17, 21] in the literature for several cases with $N = 3$ and $N = 4$ electrons. These calculations will be of great assistance in evaluating the accuracy of the REM method (see section 2.3).

In the above Eq. (19), we have used exact diagonalization in the lowest Landau level for evaluating the interelectron contribution to the total energy. In alternative treatments, one may obtain the interelectron energy contribution through the use of various approximate wave functions restricted to the LLL. These include the use of the Laughlin wave function and descendants thereof (e.g., composite fermions), or the rotating electron wave functions at the limit $B \to \infty$, which is reached by setting $\lambda = l_B\sqrt{2}$ in the right-hand-side of Eq. (7) (defining the displaced orbital). For these cases, we will use the obvious notations $\widetilde{E}_{\mathrm{tot,LLL}}^{\mathrm{Laughlin}}(B, L)$, $\widetilde{E}_{\mathrm{tot,LLL}}^{\mathrm{CF}}(B, L)$, and $\widetilde{E}_{\mathrm{tot,LLL}}^{\mathrm{REM}}(B, L)$.

2.3 Comparison of approximate results with exact diagonalization calculations

2.3.1 Ground-state energies in external confinement

Before proceeding with the presentation of results for $N > 10$, we demonstrate the accuracy of the two-step method through comparisons with existing EXD results for smaller sizes. In Fig. 1, our calculations for ground-state energies as a function of B are compared to EXD calculations [14] for $N = 4$ electrons in an external parabolic confinement. The thick dotted line (red) represents the broken-symmetry UHF approximation (first step of our method), which naturally is a smooth curve lying above the EXD one [solid line (green)]. The results obtained after restoration of

symmetry [dashed-dotted line (blue); marked as REM] agree very well with the EXD one in the whole range 2 T< B < 15 T. [53] We recall here that, for the parameters of the QD, the electrons form in the intrinsic frame of reference a square about the origin of the dot, i.e., a (0,4) configuration, with the zero indicating that no electron is located at the center. According to Eq. (9), $L_0 = 6$, and the magic angular momenta are given by $L_m = 6 + 4k$, $k = 0, 1, 2, ...$

To further evaluate the accuracy of the two-step method, we also display in Fig. 1 [thin dashed line (violet)] ground-state energies calculated with the commonly used [13, 19, 52] approximation $\widetilde{E}_{\text{tot,LLL}}^{\text{EXD}}(B)$ (see section 2.2.2). We find that the energies $\widetilde{E}_{\text{tot,LLL}}^{\text{EXD}}(B)$ tend to substantially overestimate the REM (and EXD) energies for lower values of B (e.g., by as much as 5.5% at $B \sim 4$ T). On the other hand, for higher values of B (> 12 T), the energies $\widetilde{E}_{\text{tot,LLL}}^{\text{EXD}}(B)$ tend to agree rather well with the REM ones. A similar behavior is exhibited also by the $\widetilde{E}_{\text{tot,LLL}}^{\text{REM}}(B)$ energies [the interaction energies are calculated within the LLL using the REM wave function; dotted line (black)]. We have found that the overestimation exhibited by the $\widetilde{E}_{\text{tot,LLL}}^{\text{EXD}}(B)$ energies is due to the fact that the actual dimensionless Coulomb coefficient $\widetilde{\mathcal{E}}_{\text{int,LLL}}^{\text{EXD}}(L)$ [See Eq. (19)] is not independent of the magnetic field, but decreases slowly as B decreases when the effect of the confinement is considered (see Appendix A). A similar agreement between REM and EXD results, and a similar inaccurate behavior of the limiting-case approximation, was found by us also for $N = 3$ electrons in the range 2 T $< B <$ 16 T shown in Fig. 2 (the EXD calculation was taken from Ref. [21]).

In all cases, the total energy of the REM is lower than that of the SEM (see, e.g., Figs. 1 and 2). Indeed, a theorem discussed in Sec. III of Ref. [54], pertaining to the energies of projected wave functions, guarantees that this lowering of energy applies for all values of N and B.

Table 1: Comparison of yrast-band energies obtained from REM and EXD calculations for $N = 6$ electrons in the lowest Landau level, that is in the limit $B \to \infty$. In this limit the external confinement can be neglected and only the interaction energy contributes to the yrast-band energies. Energies in units of $e^2/(\kappa l_B)$. For the REM results, the (1,5) polygonal-ring arrangement was considered. For $L < 140$, see Table 2.4 in Ref. [16](b) and Table 2.2 in Ref. [18](c). The values of the fractional filling may be obtained for each L as $\nu = N(N-1)/(2L)$.

L	REM	EXD	Error (%)
140	1.6059	1.6006	0.33
145	1.5773	1.5724	0.31
150	1.5502	1.5455	0.30
155	1.5244	1.5200	0.29
160	1.4999	1.4957	0.28
165	1.4765	1.4726	0.27
170	1.4542	1.4505	0.26
175	1.4329	1.4293	0.25
180	1.4125	1.4091	0.24
185	1.3929	1.3897	0.23
190	1.3741	1.3710	0.23
195	1.3561	1.3531	0.22
200	1.3388	1.3359	0.21

2.3.2 Yrast rotational band at $B \to \infty$

As a second accuracy test, we compare in Table 2.1 REM and EXD results for the interaction energies of the yrast band for $N = 6$ electrons in the lowest Landau level [an yrast state is the lowest energy state for a given magic angular momentum L_m, Eq. (9)]. The relative error is smaller than 0.3%, and it decreases steadily for larger L values.

2.4 Illustrative examples from microscopic REM calculations

2.4.1 Which ring isomer has the lowest ground-state energy?: REM versus UHF energies

For a given number N of electrons, there exist[47] in general more than one polygonal-ring isomers, associated with stable and metastable equilibrium configurations of N electrons inside an external harmonic confinemnet $\hbar\omega_0$. Figure 3 displays UHF and

REM ground-state energies for $N = 6$ and $N = 9$ electrons associated with the various classical polygonal-ring configurations. For $N = 6$, one has two isomers, i.e., a (0,6) configuration and a (1,5) configuration (with one lectron at the center). For $N = 9$ electrons, there exist three different isomers, i.e., (0,9), (1,8), and (2,7). From the bottom panel in Fig. 3, we observe that for $N = 9$ electrons, the lowest REM energies correspond to the classically stable isomer, i.e., to the (2,7) configuration with two electrons in the inner ring and seven electrons in the outer ring. In particular, we note that the (0,9) isomer (which may be associated with a single-vortex state) yileds REM energies far above the (2,7) one in the whole magnetic-field range $5 \text{ T} < B < 25 \text{ T}$, and in particular for magnetic fields immediately above those associated with the MDD (the so-called MDD break-up range); the MDD for $N = 9$ electrons has an angular momentum $L_0 = 36$ and corresponds to the first energy oscillation in the figure.

We have found that the $(0, N)$ isomer is not associated with REM ground energies for any magnetic-field range in all cases with $N \geq 7$. The only instance when the $(0, N)$ configuration is associated with a REM ground-state energy is the $N = 6$ case [see Fig. 3, top frame], where the REM energy of the (0,6) configuration provides the ground-state energy in the range $6.1 \text{ T} < B < 7.7 \text{ T}$, immediately after the break-up of the MDD.

For comparison, we have also plotted in Fig. 3 the UHF energies as a function of the magnetic field. Most noticeable is the fact that the REM ground states, compared to the UHF ones, may result in a different ordering of the isomers. For example, in the range $5 \text{ T} < B < 6.1 \text{ T}$, the UHF indicates, by a small energetic advantage, the (0,6) as the ground-state configuration associated with the MDD, while the REM specifies the (1,5) arrangement as the ground-state configuration. A similar switching of the ground-state isomers is also seen between the (1,8) and (2,7) configurations in the case of $N = 9$ electrons in the magnetic-field range $5 \text{ T} < B < 11.5 \text{ T}$. We conclude

that transitions between the different electron-molecule isomers derived from UHF energies alone[55, 56] are not reliable.

2.4.2   The case of $N = 9$ electrons

In figure 4 we show ground-state energies for the case of $N = 9$ electrons, which have a nontrivial double-ring configuration (n_1, n_2). Here, the most stable configuration for classical point charges[47] is $(2, 7)$, for which we have carried UHF (SEM) and REM (projected) calculations in the magnetic field range $5 \text{ T} < B < 25 \text{ T}$. We also display in Fig. 4 the energies $\widetilde{E}_{\text{tot,LLL}}^{\text{REM}}(B)$ [dotted curve (black)], which, as in the $N = 4$ and $N = 3$ cases discussed in the section 2.3, overestimate the ground-state energies, in particular for smaller B. [57] In keeping with the findings for smaller sizes [16]$^{(c)}$ [with $(0, N)$ or $(1, N - 1)$ configurations], both the UHF and the REM ground-state energies of the $N = 9$ case approach as $B \rightarrow \infty$ the *classical* equilibrium energy of the (2,7) polygonal configuration [i.e., 16.75 meV; $4.088 E_0$ in the units of Ref. [47], $E_0 \equiv (m^* \omega_0^2 e^4 / 2\kappa^2)^{1/3}$].

In analogy with smaller sizes [see, e.g., Figs. 1 and 2 for $N = 4$ and $N = 3$], the REM ground-state energies in Fig. 4 exhibit oscillations as a function of B. These oscillations reflect the incompressibility of the many-body states associated with magic angular momenta. The magic angular momenta are specified by the number of electrons on each ring, and in general they are given by $L_m = N(N-1)/2 + \sum_{q=1}^{r} k_q n_q$, where the n_q's are the number of electrons located in the qth ring and the k_q's are non-negative integers; in particular, $L_m = 36 + 2k_1 + 7k_2$ for the $N = 9$ case in Fig. 4. An analysis of the actual values taken by the set of indices $\{k_1, k_2\}$ reveals several additional trends that further limit the allowed values of ground-state L_m's. In particular, starting with the values $\{k_1 = 0, k_2 = 0\}$ at $B = 5 \text{ T}$ ($L_m^{\text{MDD}} = 36$), the indices $\{k_1, k_2\}$ reach the values $\{2, 24\}$ at $B = 25 \text{ T}$ ($L_m = 208$). As seen form Table 2.2, the outer index k_2 has a short period, while the inner index k_1 exhibits a

Table 2: Ground-state magic angular momenta and their decomposition $\{k_1, k_2\}$ for $N = 9$ in the nagnetic-field range 5 T $\leq B \leq$ 25 T. These results correspond to the REM [see lower curve in Fig. 2.4, with the electrons arranged in a (2,7) structure]. The parameters used are as in Fig. 2.4.

L_m	k_1	k_2	L_m	k_1	k_2
36	0	0	129	1	13
43	0	1	136	1	14
50	0	2	143	1	15
57	0	3	150	1	16
64	0	4	157	1	17
71	0	5	164	1	18
78	0	6	171	1	19
87	1	7	173	2	19
94	1	8	180	2	20
101	1	9	187	2	21
108	1	10	194	2	22
115	1	11	201	2	23
122	1	12	208	2	24

longer period and increases much more slowly than k_2. This behavior minimizes the total kinetic energy of the independently rotating rings (having a variable radius, see section 2.5 below).

Table 3: Ground-state magic angular momenta and their decomposition $\{k_1, k_2\}$ for $N = 9$ electrons associated with the $\widetilde{E}_{\text{tot,LLL}}^{\text{REM}}$ curve [top curve in Fig. 2.4; see section 2.2.2 for an explanation of notation; the electrons are arranged in a (2,7) structure].

L_m	k_1	k_2	L_m	k_1	k_2
36	0	0	57	0	3
45	1	1	64	0	4
52	1	2	71	0	5

We also list in Table 2.3 the first few pairs of indices $\{k_1, k_2\}$ associated with the $\widetilde{E}_{\text{tot,LLL}}^{\text{REM}}$ curve (see top dotted curve in Fig. 4). It can be seen that the magic angular momenta are different from those associated with the REM curve, when the confinement is taken into consideration using the full projected wave function in Eq. (8). The magic angular momenta of the $\widetilde{E}_{\text{tot,LLL}}^{\text{REM}}$ curve coincide with the L_m's of the EXD within the LLL, and thus are characterized by having $L_0 + N = 45$ (instead of $L_0 + n_2 = 43$) as the magic angular momentum immediately following that of the

MDD (i.e., $L_0 = 36$). The $L_0 + N$ magic angular momentum is associated with the $(0, N)$ ring arrangement, which can be interpreted as a single "vortex-in-the-center" state.

Based on EXD calculations restricted to the lowest Landau level [58, 24, 59] (that is, $\widetilde{E}_{\text{int,LLL}}^{\text{EXD}}$ or $\widetilde{E}_{\text{tot,LLL}}^{\text{EXD}}$ in our notation), it has been conjectured that for QDs with $N < 15$, the break-up of the MDD with increasing B proceeds through the formation of the above mentioned single central vortex state. However, our REM calculations show (see also the case of $N = 11$ electrons in section 2.4.3 and the case of $N = 17$ electrons in section 2.4.4) that taking into account properly the influence of the confinement does not support such a scenario. Instead, the break-up of the MDD resembles an edge reconstruction and it proceeds (for all dots with $N > 6$) through the gradual detachement of the *outer ring* associated with the classical polygonal configuration (see Table 2.2 for the case of $N = 9$ electrons). The only case we found where the break-up of the MDD proceeds via a (0,6) vortex state is the one with $N = 6$ electrons (see section 2.4.1),; and naturally the cases with $N \leq 5$.

As another illustration of the subtle, but important, differences that exist between wave functions defined exclusively within the LLL and those specified by the REM wave function for finite B in Eq. (8), we display in Fig. 5 for $N = 9$ electrons the radial electron densities of the MDD at $B \to \infty$ and at $B = 5.5$ T. While the electron density of the MDD in the LLL ($B \to \infty$) is constant in the central region [up to $r \approx 3l_B$, see Fig. 5(a)], the corresponding density at $B = 5.5$ T displays the characteristic oscillation corresponding to the (2,7) multi-ring structure [see Fig. 5(b)]; the latter behavior is due to the mixing of higher Landau levels. To further illustrate the (2,7) crystalline character of the MDD when higher Landau levels are considered, we display in Fig. 6 the corresponding CPDs associated with the REM wave function of the MDD at $B = 5.5$ T and an external confinement of $\hbar\omega_0 = 3.6$ meV. Our conclusions concerning the MDD electron densities (and CPDs) are supported by

EXD calculations for $N = 4$ electrons.[60] Note that, while the ring structure is well developed in the CPDs shown in Fig. 6, the internal (2,7) structure of the rings (see in particular the outer ring in the left panel in Fig. 6) is rather weak, as expected for the lowest angular momentum L_0 (MDD). However, the ring structure is easily discernible in contrast to the CPDs for the MDD *restricted to the LLL* where structureless CPDs (as well as structureless electron densities) are found.

2.4.3 The case of $N = 11$ electrons

Table 4: Ground-state magic angular momenta and their decomposition $\{k_1, k_2\}$ for $N = 11$ in the nagnetic-field range 5 T $\leq B \leq$ 25 T. The results correspond to the REM (see lower curve in Fig. 2.7). The parameters used are as in Fig. 2.7.

L_m	k_1	k_2	L_m	k_1	k_2
55	0	0	165	2	13
63	0	1	173	2	14
71	0	2	181	2	15
79	0	3	189	2	16
90	1	4	197	2	17
98	1	5	205	2	18
106	1	6	213	2	19
114	1	7	224	3	20
122	1	8	232	3	21
130	1	9	240	3	22
138	1	10	248	3	23
146	1	11	256	3	24
154	1	12			

Figure 7 presents the case for the ground-state energies of a QD with $N = 11$ electrons, which have a nontrivial double-ring configuration (n_1, n_2). The most stable[47] classical configuration is $(3, 8)$, for which we have carried UHF (SEM) and REM (projected) calculations in the magnetic field range 5 T $< B <$ 25 T. Figure 7 also displays the LLL ground-state energies $\widetilde{E}_{\text{tot,LLL}}^{\text{REM}}(B)$ [dotted curve (black)], which, as in previous cases, overestimate the ground-state energies for smaller B. The approximation $\widetilde{E}_{\text{tot,LLL}}^{\text{REM}}(B)$, however, can be used to calculate ground-state energies for higher values of B. In keeping with the findings for smaller sizes [16][(c)] [with $(0, N)$ or $(1, N-1)$

configurations], we found that both the UHF and the REM ground-state energies approach, as $B \rightarrow \infty$, the *classical* equilibrium energy of the (3,8) polygonal configuration [i.e., 19.94 meV; $4.865 E_0$ in the units of Ref. [47], $E_0 \equiv (m^* \omega_0^2 e^4 / 2\kappa^2)^{1/3}$].

In analogy with smaller sizes [see, e.g., Figs. 1, 2, and 4 for $N = 4$, 3, and 9, respectively], the REM ground-state energies in Fig. 7 exhibit oscillations as a function of B (see in particular the inset). As discussed in section 2.4.2, these oscillations are associated with magic angular momenta, specified by the number of electrons on each ring. For $N = 11$ they are given by Eq. (9), i.e., $L_m = 55 + 3k_1 + 8k_2$, with the k_q's being nonnegative integers. As was the case with $N = 9$ electrons, an analysis of the actual values taken by the set of indices $\{k_1, k_2\}$ reveals several additional trends that further limit the allowed values of ground-state L_m's. In particular, starting with the values $\{0, 0\}$ at $B = 5$ T ($L_0 = 55$), the indices $\{k_1, k_2\}$ reach the values $\{3, 24\}$ at $B = 25$ T ($L_m = 256$). As seen from Table 2.4, the outer index k_2 changes faster than the inner index k_1. This behavior minimizes the total kinetic energy of the independently rotating rings; indeed, the kinetic energy of the inner ring (as a function of k_1) rises faster than that of the outer ring (as a function of k_2) due to smaller moment of inertia (smaller radius) of the inner ring [see Eq. (20)].

In addition to the overestimation of the ground-state energy values, particularly for smaller magnetic fields (see Fig. 7 and our above discussion), the shortcomings of the LLL approximation pertaining to the ground-state ring configurations [see section 2.2, Eq. (19)], as discussed by us above for $N = 9$, persist also for $N = 11$. In particular, we find that according to the LLL approximation the ground-state angular-momentum immediately after the MDD ($L_0 = 55$) is $L_m = 66$, i.e., the one associated with the $(0, N)$ vortex-in-the-center configuration. This result, erroneously stated in Ref. [59] as the ground state, disagrees with the correct result that includes the effect of the confinement – listed in Table 2.4, where the ground-state angular momentum immediately following the MDD is $L_m = 63$. This angular momentum corresponds

to the classicaly most stable (3,8) ring configuration – that is a configuration with no vortex at all.

Figure 8 displays the REM conditional probability distributions for the ground state of $N = 11$ electrons at $B = 10$ T ($L_m = 106$). The (3,8) ring configuration is clearly visible. We note that when the observation point is placed on the outer ring (left panel), the CPD reveals the crystalline structure of this ring only; the inner ring appears to have a uniform density. To reveal the crystalline structure of the inner ring, the observation point must be placed on this ring; then the outer ring appears to be uniform in density. This behavior suggests that the two rings rotate independently of each other, a property that we will explore in section 2.5 to derive an approximate expression for the yrast rotational spectra associated with an arbitrary number of electrons.

2.4.4   The case of $N = 17$ electrons

Figure 9 presents (for 5 T $\leq B \leq$ 15 T) REM and UHF ground-state energies for $N = 17$ electrons, which have a (1,6,10) three-ring configuration as the most stable classical arrangement. [47]

In analogy with smaller sizes [see, e.g., previous figures for $N \leq 12$] the REM ground-state energies in Fig. 9 exhibit oscillations as a function of B, and each oscillation is associated with a given particular (magic) value of the angular momentum. Earlier in this section we discussed the physical origins of the magic angular momenta. As before, the magic angular momenta are specified by the number of electrons on each ring [(9)], with $L_0 = 136$ and $L_m = 136 + 6k_2 + 10k_3$ for $N = 17$; k_q's being non-negative integers (the central electron does not contribute to the total angular momentum). Analysis of the particular values taken by the set of indices $\{k_2, k_3\}$ reveals similar trends to those found for the cases with $N = 9$ and $N = 11$ electrons. In particular, starting with the values $\{0,0\}$ at $B = 5$ T ($L_0 = 136$), the indices

Table 5: Ground-state magic angular momenta and their decomposition $\{k_2, k_3\}$ for $N = 17$ electrons in the nagnetic-field range 5 T $\leq B \leq$ 15 T. The rersults correspond to the REM (see lower curve in Fig. 2.9). The parameters used are as in Fig. 2.9.

L_m	k_2	k_3	L_m	k_2	k_3
136	0	0	238	2	9
146	0	1	248	2	10
156	0	2	264	3	11
166	0	3	274	3	12
172	1	3	284	3	13
182	1	4	294	3	14
192	1	5	310	4	15
202	1	6	320	4	16
212	1	7	330	4	17
218	2	7	340	4	18
228	2	8	346	5	18

$\{k_2, k_3\}$ reach the values $\{k_2 = 5, k_3 = 18\}$ at $B = 15$ T ($L_m = 346$). As seen from Table 2.5, the outer index k_3 changes faster, than the inner index k_2. This behavior minimizes the total kinetic energy of the independently rotating rings, as was already discussed for $N = 9$ and $N = 11$ electrons.

We have also calculated the ground-state energies for $N = 17$ electrons in the LLL approximation, i.e., we calculated the quantity $\widetilde{E}_{\text{tot,LLL}}^{\text{REM}}(B)$ (not shown in Fig. 9). We find once more that $\widetilde{E}_{\text{tot,LLL}}^{\text{REM}}(B)$ overestimates the ground-state energies in the magnetic-field range covering the MDD and the range immediately above the MDD. For $N = 17$, however, the shortcoming of the LLL approximation is not reflected in the determination of the ground-state ring configurations. We find that for $N = 17$ the LLL approximation yields a (1,6,10) ring configuration (with $L_m = 146$) for the ground state immediately following the MDD, in agreement with the REM configurations listed in Table 2.5.

2.5 REM yrast band excitation spectra and derivation of analytic approximation formula

In Fig. 10, we display the CPD for the REM wave function of $N = 17$ electrons. This case has a nontrivial three-ring structure (1,6,10), [47] which is sufficiently complex to allow generalizations for larger numbers of particles. The remarkable combined character (partly crystalline and partly fluid leading to a non-classical rotational inertia, see section 2.6) of the REM is illustrated in the CPDs of Fig. 10. Indeed, as the two CPDs [reflecting the choice of taking the observation point [$\mathbf{r}_0$ in Eq. (14)] on the outer (left frame) or the inner ring (right frame)] reveal, the polygonal electron rings rotate *independently* of each other. Thus, e.g., to an observer located on the inner ring, the outer ring will appear as having a uniform density, and vice versa. The wave functions obtained from exact diagonalization exhibit also the property of independently rotating rings [see e.g., the $N = 12$ and $L = 132$ ($\nu = 1/2$) case in Fig. 11], which is a testimony to the ability of the REM wave function to capture the essential physics [61] of a finite number of electrons in high B. In particular, the conditional probability distribution obtained for exact diagonalization wave functions in Fig. 11 exhibits the characteristics expected from the CPD evaluated using REM wave functions for the (3,9) configuration and with an angular-momentum decomposition into shell contributions [see Eqs. (8) and (10)] $L_1 = 3 + 3k_1$ and $L_2 = 63 + 9k_2$ ($L_1 + L_2 = L_m$; for $L_m = 132$ the angular-momentum decomposition is $L_1 = 6$ and $L_2 = 126$).

In addition to the conditional probabilities, the solid/fluid character of the REM is revealed in its excited rotational spectrum for a given B. From our microscopic calculations based on the wave function in Eq. (8), we have derived (see below) an approximate (denoted as "app"), but *analytic* and *parameter-free*, expression [see Eq. (25) below] which reflects directly the nonrigid (nonclassical) character of the REM for arbitrary size. This expression allows calculation of the energies of REMs for

arbitrary N, given the corresponding equilibrium configuration of confined classical point charges.

We focus on the description of the yrast band at a given B. Motivated by the aforementioned nonrigid character of the rotating electron molecule, we consider the following kinetic-energy term corresponding to a $(n_1, ..., n_q, ..., n_r)$ configuration (with $\sum_{q=1}^{r} n_q = N$):

$$E_{\text{app}}^{\text{kin}}(N) = \sum_{q=1}^{r} \hbar^2 L_q^2/(2\mathcal{J}_q(a_q)) - \hbar\omega_c L/2, \tag{20}$$

where L_q is the partial angular momentum associated with the qth ring about the center of the dot and the total angular momentum is $L = \sum_{q=1}^{r} L_q$. $\mathcal{J}_q(a_q)) \equiv n_q m^* a_q^2$ is the rotational moment of inertia of each *individual* ring, i.e., the moment of inertia of n_q classical point charges on the qth polygonal ring of radius a_q. To obtain the total energy, E_L^{REM}, we include also the term $E_{\text{app}}^{\text{hc}}(N) = \sum_{q=1}^{r} \mathcal{J}_q(a_q)\Omega^2/2$ due to the effective harmonic confinement Ω [see discussion of Eq. (7)], as well as the interaction energy E_{app}^C,

$$E_{\text{app}}^C(N) = \sum_{q=1}^{r} \frac{n_q S_q}{4} \frac{e^2}{\kappa a_q} + \sum_{q=1}^{r-1}\sum_{s>q}^{r} V_C(a_q, a_s). \tag{21}$$

The first term is the intra-ring Coulomb-repulsion energy of n_q point-like electrons on a given ring, with a structure factor

$$S_q = \sum_{j=2}^{n_q} (\sin[(j-1)\pi/n_q])^{-1}. \tag{22}$$

The second term is the inter-ring Coulomb-repulsion energy between rings of uniform charge distribution corresponding to the specified numbers of electrons on the polygonal rings. The expression fo V_C is

$$\begin{aligned} V_C(a_q, a_s) &= n_q n_s \, {}_2F_1[3/4, 1/4; 1; 4a_q^2 a_s^2 (a_q^2 + a_s^2)^{-2}] \\ &\times e^2 (a_q^2 + a_s^2)^{-1/2}/\kappa, \end{aligned} \tag{23}$$

where $_2F_1$ is the hypergeometric function.

For large L (and/or B), the radii of the rings of the rotating molecule can be found by neglecting the interaction term in the total approximate energy, thus minimizing only $E_{\text{app}}^{\text{kin}}(N) + E_{\text{app}}^{\text{hc}}(N)$. One finds

$$a_q = \lambda\sqrt{L_q/n_q};\tag{24}$$

i.e., the ring radii depend on the partial angular momentum L_q, reflecting the *lack of radial rigidity*. Substitution into the above expressions for $E_{\text{app}}^{\text{kin}}$, $E_{\text{app}}^{\text{hc}}$, and E_{app}^{C} yields for the total approximate energy the final expression:

$$\begin{aligned}
E_{\text{app},L}^{\text{REM}}\ (N) = {}& \hbar(\Omega - \omega_c/2)L + \\
& \sum_{q=1}^{r}\frac{C_{V,q}}{L_q^{1/2}} + \sum_{q=1}^{r-1}\sum_{s>q}^{r}V_C(\lambda\sqrt{\frac{L_q}{n_q}},\lambda\sqrt{\frac{L_s}{n_s}}),
\end{aligned}\tag{25}$$

where the constants

$$C_{V,q} = 0.25 n_q^{3/2}S_q e^2/(\kappa\lambda).\tag{26}$$

For simpler $(0, N)$ and $(1, N-1)$ ring configurations, Eq. (25) reduces to the expressions reported earlier.[7(c), 62]

2.6 A non-rigid crystalline phase: Non-classical rotational inertia of electrons in quantum dots

In Fig. 12 (left frame), and for a sufficiently high magnetic field (e.g., $B = 100$ T such that the Hilbert space of the system reduces to the lowest Landau level), we compare the approximate analytic energies $E_{\text{app},L}^{\text{REM}}$ with the microscopic energies E_L^{REM} calculated from Eq. (11) using the same parameters as in Fig. 9 for $N = 17$ electrons. The two calculations agree well, with a typical difference of less than 0.5% between them. More important is the marked difference between these results and the total energies of the *classical* (rigid rotor) molecule (E_L^{rig}), plotted in the right

frame of Fig. 12; the latter are given by

$$E_L^{\text{rig}} = \hbar^2 L^2/(2\mathcal{J}_{\text{rig}}) + 0.5 \sum_{i=1}^{N} m^* \omega_0^2 |Z_i|^2 +$$

$$\sum_{i=1}^{N} \sum_{j>i}^{N} e^2/(\kappa |Z_i - Z_j|), \tag{27}$$

with the rigid moment of inertia being [63]

$$\mathcal{J}_{\text{rig}} = \sum_{i=1}^{N} m^* |Z_i|^2. \tag{28}$$

The disagreement between the REM and the classical energies is twofold: (i) The L dependence is different, and (ii) The REM energies are three orders of magnitude smaller than the classical ones. That is, the energy cost for the rotation of the REM is drastically smaller than for the classical rotation, thus exhibiting non-classical rotational behavior. In analogy with Ref. [40], we define a "non-rigidity" index

$$\alpha = (E_L^{\text{rig}} - E_L^{\text{REM}})/E_L^{\text{rig}}. \tag{29}$$

For the case displayed in Fig. 12, we find that this index varies (for $1116 \leq L \leq 3716$) from $\alpha = 0.978$ to $\alpha = 0.998$, indicating that the rotating electron molecule, while possessing crystalline correlations is (rotationally) of a high non-rigid nature. We remark that our definition of α in Eq. (29) was motivated by a similar form of an index of supefluid fraction introduced in Ref. [40]; we do not mean to imply the presence of a superfluid component for electrons in quantum dots.

In the context of the appearance of supersolid behavior of ^{4}He under appropriate conditions, formation of a supersolid fraction is often discussed in conjunction with the presence of (i) real defects and (ii) real vacancies. [38, 39] Our REM wave function [Eq. 8] belongs to a third possibility, namely to *virtual* defects and vacancies, with the number of particles equal to the number of lattice sites (in the context of ^{4}He, the possibility of a supersolid with equal number of particles and lattice sites is mentioned in Ref. [42]). Indeed, the azimuthal shift of the electrons by $(\gamma_1, \gamma_2, ..., \gamma_r)$ [see Eq.

(8)] may be viewed as generating *virtual* defects and vacancies with respect to the original electron positions at $(\gamma_1 = 0, \gamma_2 = 0, ..., \gamma_r = 0)$ on the polygonal rings.

A recent publication [52] has explored the quantal nature of the 2D electron molecules in the lowest Landau level $(B \to \infty)$ using a modification of the second-quantized LLL form of the REM wave functions. [16] In particular, the modification consisted of a multiplication of the *parameter free* REM wave function by variationally adjustable Jastrow-factor vortices. Without consideration of the rotational properties of the modified wave function, the inherently quantal nature of the molecule was attributed exclusively to the Jastrow factor. However, as shown above, the original REM wave function [Eq. (8)] already exhibits a characteristic non-classical rotational inertia (NCRI). Consequently, the additional *variational* freedom introduced by the Jastrow prefactor may well lead energetically to a slight numerical improvement, but it does not underlie the *essential quantal* physics of the system. Indeed, as discussed previously and illustrated in detail above, the important step is the projection of the static electron molecule onto a state with good total angular momentum [see Eqs. (7) and (8)].

2.7 Summary

The focus of this part pertains to the development of methods that permit investigations of the energetic, structural, and excitation properties of quantum dots in strong magnetic fields with an (essentially) arbitrary number of electrons. Towards this aim, we utilized several computational methods, and have assessed their adequacy. The methods that we have used are: (1) Exact diagonalization which is limited to a rather small number of particles; (2) The "two-step" successive-hierarchical-approximations method (see section 2.2.1), in which a UHF step leading to broken-symmetry solutions (static electron molecule) is followed by restoration (via projection techniques) of circularly symmetric states with good angular momenta (rotating

34

electron molecule; REM); (3) An approximation method based on diagonalization of the electron-electron interaction term restricted to the lowest Landau level (LLL). In this method, the total energy includes, in addition to the LLL diagonalization term, a contribution from the harmonic confinement that is linear in the total angular momentum; (4) An analytic expression [see Eq. (25)] whose derivation is based on the REM.

We performed comparative calculations for quantum dots with an increasing number of parabolically confined electrons ($N = 3$, 4, 6, 9, 11, and 17). The ground-state arrangements of the electrons become structurally more complex as the number of electrons in the dot increases. Using the notation $(n_1, n_2, n_3, ...)$ for the number of electrons located on concentric polygonal rings (see section 2.2.1), the ground-state arrangements are: (0,3) for $N = 3$, (0,4) for $N = 4$, (1,5) for $N = 6$, (2,7) for $N = 9$, (3,8) for $N = 11$, and (1,6,10) for $N = 17$.

Analysis of the results of our calculations revealed that, for all sizes studied by us, the two-step REM method provides a highly accurate description of electrons parabolically confined in quantum dots for a whole range of applied magnetic fields, starting from the neighborhood of the so-called maximum density droplet and extending to the $B \rightarrow \infty$ limit. In contrast, the LLL-diagonalization approximation was found to be rather inaccurate for weaker magnetic fields, where it grossly overestimates the total energies of the electrons; the accuracy of this latter method improves at higher field strengths.

The ground-state energy of the electrons in a QD oscillates as a function of the applied magnetic field, and the allowed values of the angular momenta are limited to a set of magic angular momentum values, L_m, which are a natural consequence of the geometrical arrangement of the electrons in the rotating electron molecule. Accordingly, the electrons are localized on concentric polygonal rings which rotate

35

independently of each other (as observed from the conditional probability distributions, see section 2.4). Underlying the aforementioned oscillatory behavior is the incompressibility of the many-body states associated with the magic angular momenta. The general expression for L_m is given in Eq. (9), for a given number N and occupancy of the polygonal rings $\{n_q\}$. For the ground-state L_m's, the values of the non-negative integers k_q in Eq. (9) are taken such as to minimize the total kinetic energy of the electrons. Since the moment of inertia of an outer ring is larger than that of an inner ring of smaller radius, the rotational energy of the outer ring will increase more slowly with increasing angular momentum. Therefore, the k_q index in Eq. (9) of an outer ring will very up to relatively large values while the values corresponding to inner rings remain small (see section 2.4). As a consequence, we find through REM calculations with proper treatment of the confining potential that for $N > 6$, with increasing strength of the magnetic field, the maximum density droplet converts into states with no central vortex, in contrast to earlier conclusions[24, 58, 59] drawn on the basis of approximate calculations restricted to the lowest Landau level. Instead we find that the break-up of the MDD with increasing B proceeds through the gradual detachment of the outer ring associated with the corresponding classical polygonal configuration.

In addition to the ground-state geometric arrangements, we have studied for certain sizes higher-energy structural isomers (see, e.g., the cases of $N = 6$ and $N = 9$ confined electrons in Fig. 2.3). We find that for all cases with $N \geq 7$ multi-ring confined-electron structures $(n_1, n_2, ..., n_r)$, with $n_1, n_2, ..., n_r \neq 0$ and $r \geq 2$, are energetically favored. For $N = 6$, a (1,5) structure is favored except for a small B-range (e.g., 6.1 T $< B <$ 7.7 T for the parameters in Fig. 2.3), where the (0,6) single-ring structure is favored. For $N \leq 5$ the $(0, N)$ single-ring structure is favored for all B values.

In the REM calculations, we have utilized an analytic many-body wave function

[Eq. (8)] which allowed us to carry out computations for a sufficiently large number of electrons ($N = 17$ electrons having a nontrivial three-ring polygonal structure), leading to the derivation and validation of an analytic expression Eq. (25) for the total energy of rotating electron crystallites of arbitrary N.

The non-rigidity implied by the aforementioned independent rotations of the individual concentric polygonal rings motivated us to quantify (see section 2.6) the degree of non-rigidity of the rotating electron molecules at high B, in analogy with the concept of non-classical rotational inertia used in the analysis[40, 42] of supersolid [4]He. These findings for finite dots suggest a strong quantal nature for the extended Wigner crystal in the lowest Landau level, designating it as a useful paradigm for exotic quantum solids.

Figure 1: Two-step-method versus EXD calculations: Ground-state energies for $N = 4$ electrons (referenced to $4\hbar\Omega$) as a function of the magnetic field B. Thick dashed line (red): broken-symmetry UHF (SEM). Solid line (green): EXD (from Ref. [14]). Thick dashed-dotted line (blue): REM. Thin dashed line (violet, marked LLL): the commonly used approximate energies $\widetilde{E}^{\text{EXD}}_{\text{tot,LLL}}(B)$ [see Eq. (19)]. Thin dotted line (black): $\widetilde{E}^{\text{REM}}_{\text{tot,LLL}}(B)$ (see section 2.2.2). For $B < 8$ T, the $\widetilde{E}^{\text{EXD}}_{\text{tot,LLL}}(B)$ and $\widetilde{E}^{\text{REM}}_{\text{tot,LLL}}(B)$ curves coincide; we have checked that these curves approach each other also at larger values of B, outside the plotted range. Numbers near the bottom curves denote the value of magic angular momenta [L_m, see Eq. (9)] of the ground state. Corresponding fractional filling factors are specified by $\nu = N(N-1)/(2L_m)$. Parameters used: confinement $\hbar\omega_0 = 3.60$ meV, dielectric constant $\kappa = 13.1$, effective mass $m^* = 0.067m_e$.
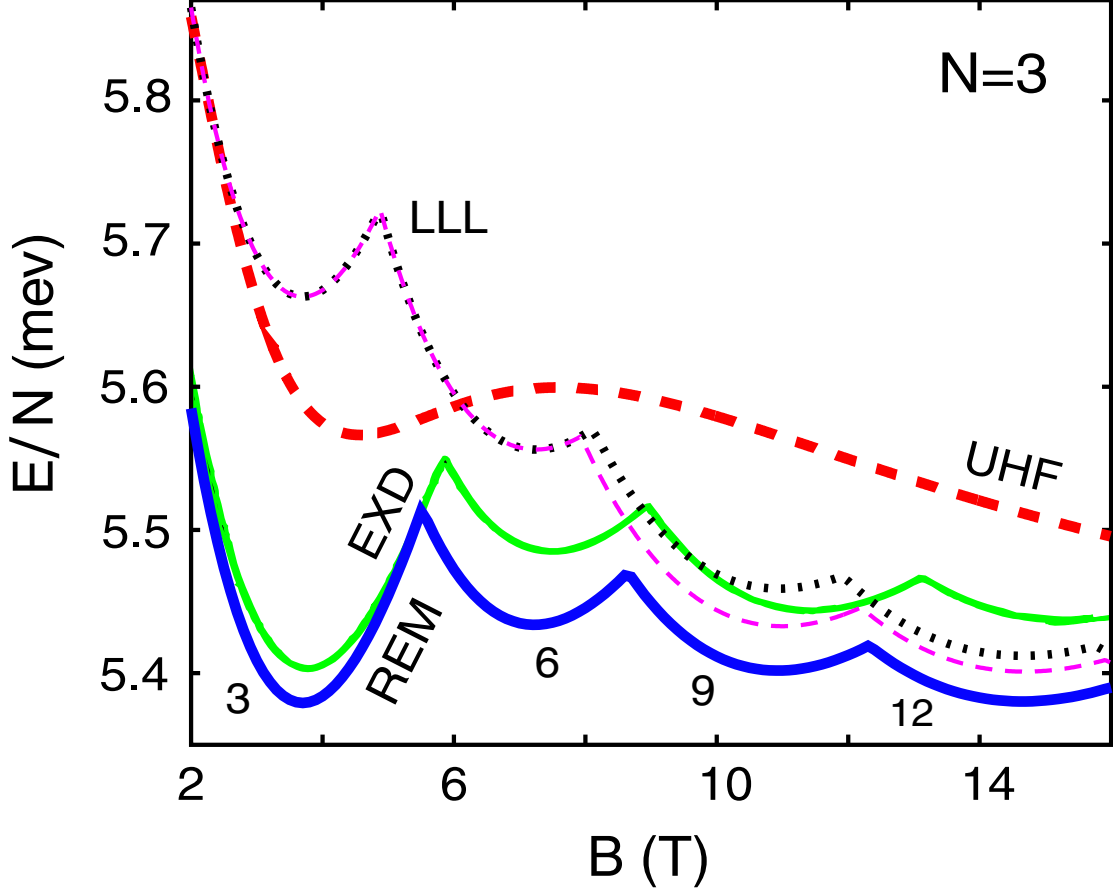
Figure 2: Two-step method versus EXD calculations: Ground-state energies (per particle, referenced to $\hbar\Omega$) for $N = 3$ electrons. The electrons are arranged in a (0,3) structure in the intrinsic frame of reference. Thick dashed line (red): broken-symmetry UHF (SEM). Thinner solid line (green): EXD (from Ref. [21]). Thick solid line (blue): REM. Thin dashed line (violet): the commonly used approximate energies $\widetilde{E}_{\rm tot,LLL}^{\rm EXD}(B)$ (see text). Thin dotted line (black): $\widetilde{E}_{\rm tot,LLL}^{\rm REM}(B)$ (see text). For $B < 8$ T, the $\widetilde{E}_{\rm tot,LLL}^{\rm EXD}(B)$ and $\widetilde{E}_{\rm tot,LLL}^{\rm REM}(B)$ curves coincide; we have checked that these curves approach each other also at larger values of B, outside the plotted range. Numbers denote the value of magic angular momenta (L_m) of the ground state. Corresponding fractional filling factors are specified by $\nu = N(N - 1)/(2L_m)$. Parameters used: confinement $\hbar\omega_0 = 3.37$ meV, dielectric constant $\kappa = 12.4$, effective mass $m^* = 0.067m_e$.
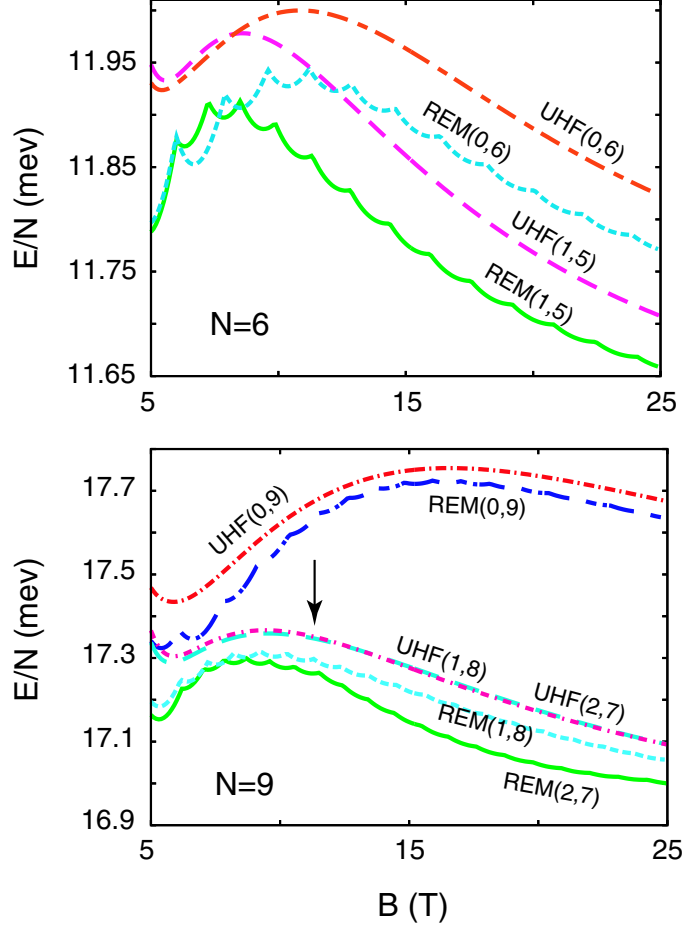
Figure 3: Comparison of REM and UHF ground-state energies per particle (referenced to $\hbar\Omega$) associated with different ring isomers for $N = 6$ and $N = 9$ electrons as a function of the magnetic field B. The curves are labeled with the computational method and the isomer (n_1, n_2). To the left of the vertical arrow (at $B = 11.5$ T), the UHF(1,8) curve is energetically favored. To the right of the vertical arrow, the UHF(2,7) curve is energetically favored. Parameters used: confinement $\hbar\omega_0 = 3.60$ meV, dielectric constant $\kappa = 13.1$, effective mass $m^* = 0.067 m_e$.
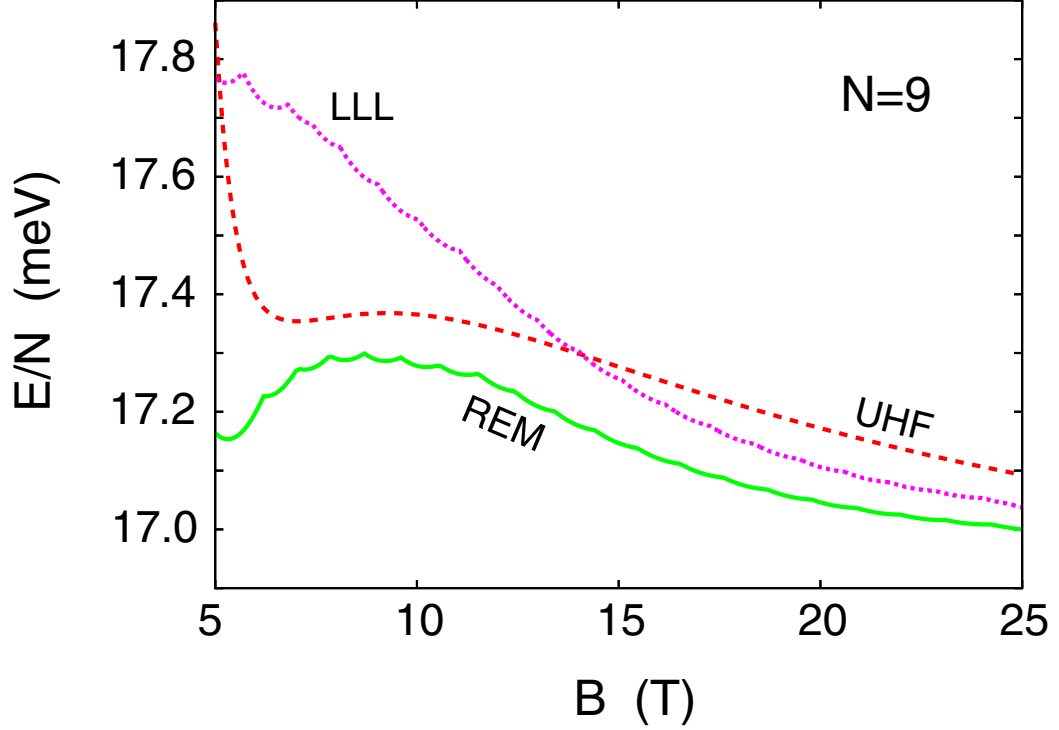
Figure 4: Ground-state energies [i.e., for the (2,7) configuration] for $N = 9$ electrons (per particle, referenced to $\hbar\Omega$) as a function of the magnetic field B. Dashed line (red): UHF (SEM). Solid line (blue): REM. Dotted line (black): approximate energies $\widetilde{E}_{\text{tot,LLL}}^{\text{REM}}(B)$ (see text). Parameters used: confinement $\hbar\omega_0 = 3.60$ meV, dielectric constant $\kappa = 13.1$, effective mass $m^* = 0.067m_e$.
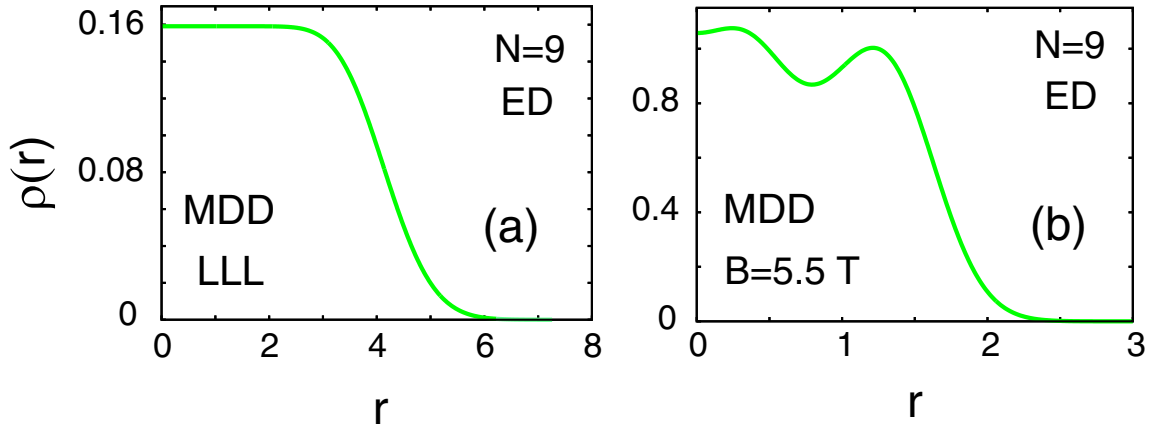
Figure 5: REM radial electron densities for the MDD ($L_m = L_0 = 36$) of $N = 9$ electrons [in the (2,7) ground-state configuration] at (a) $B \to \infty$, i.e., in the lowest Landau level and (b) at $B = 5.5$ T. Parameters used in (b): confinement $\hbar\omega_0 = 3.60$ meV, dielectric constant $\kappa = 13.1$, effective mass $m^* = 0.067m_e$. Lengths: (a) in units of the magnetic length l_B; (b) in units of $R_0 = (2e^2/m^*\kappa\omega_0^2)^{1/3}$. Electron densities: (a) in units of $1/l_B^2$; (b) in units of $1/R_0^2$. Normalization: $2\pi \int_0^\infty \rho(r)r dr = N$.
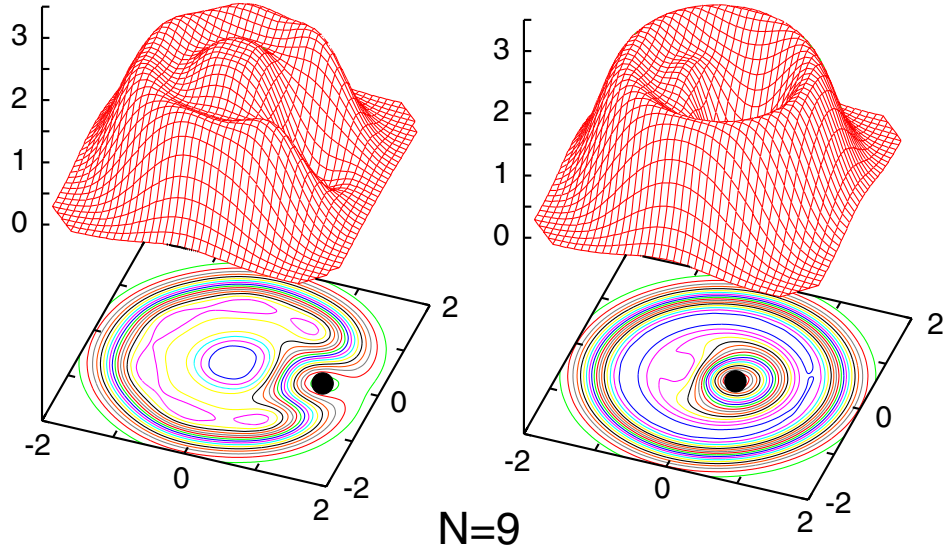
Figure 6: Conditional probability distributions obtained from REM wave functions of the MDD ($L_0 = 36$) for $N = 9$ electrons at $B = 5.5$ T [see Fig. 5(b)]. The electrons are arranged in a (2,7) structure. The observation point is denoted by a solid dot. On the left, the observation point is located on the outer shell, and on the right it is located on the inner shell. Parameters used: confinement $\hbar\omega_0 = 3.60$ meV, dielectric constant $\kappa = 13.1$, effective mass $m^* = 0.067m_e$. Lengths in units of $R_0 = (2e^2/(\kappa m^* \omega_0^2))^{1/3}$. CPDs (vertical axes) in arbitrary units.
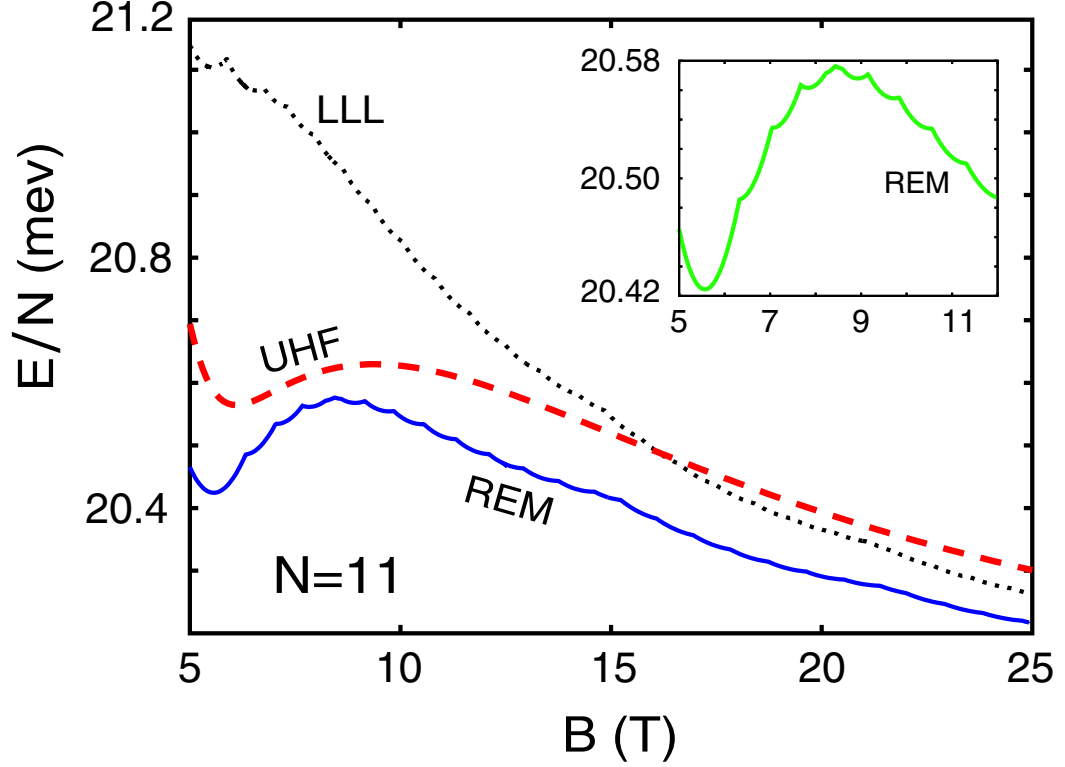
Figure 7: Ground-state energies for $N = 11$ electrons (per particle, referenced to $\hbar\Omega$) as a function of the magnetic field B. Dashed line (red): UHF (SEM). Solid line (blue): REM. Dotted line (black): Approximate energies $\widetilde{E}_{\text{tot,LLL}}^{\text{REM}}(B)$ (see text). Parameters used: confinement $\hbar\omega_0 = 3.60$ meV, dielectric constant $\kappa = 13.1$, effective mass $m^* = 0.067 m_e$. The inset shows a magnification of the REM curve in the range 5 T $< B < 12$ T.
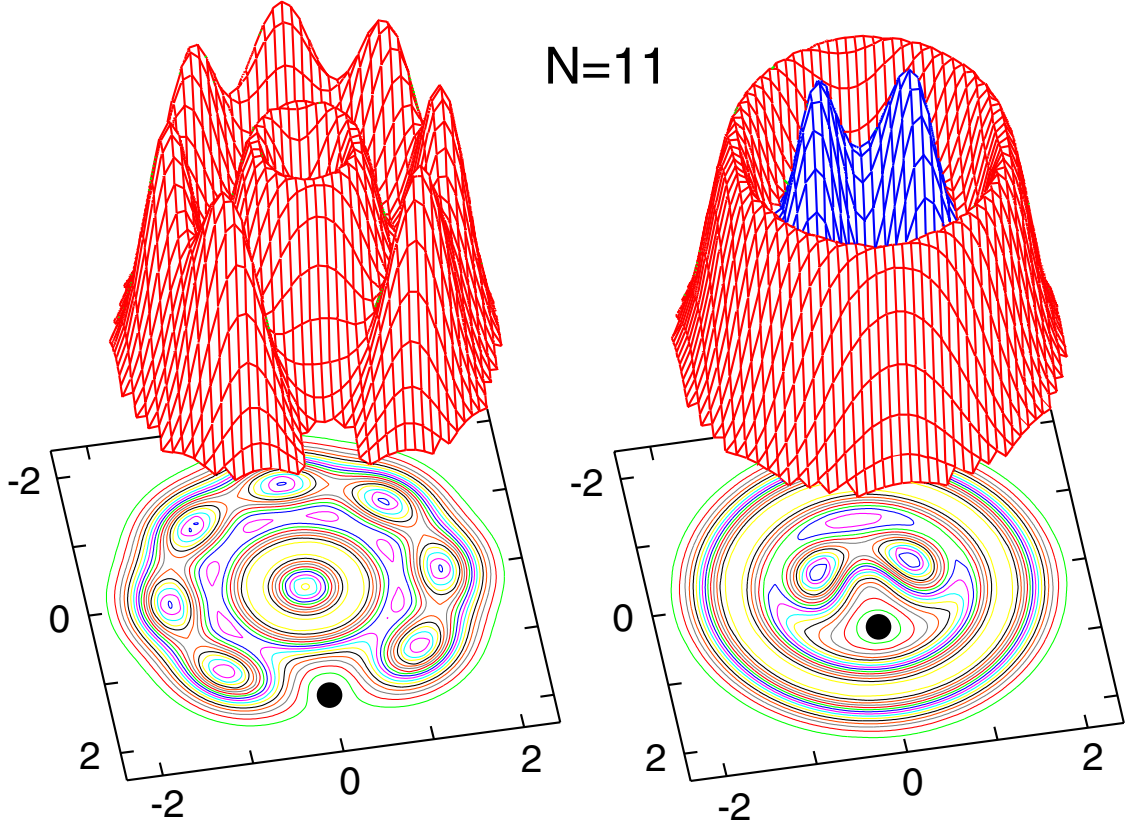
Figure 8: REM conditional probability distributions for $N = 11$ electrons at $B = 10$ T ($L = 106$). The electrons are arranged in a (3,8) structure. The observation point (solid dot) is placed on (left) the outer ring at $r_0 = 1.480R_0$, and (right) on the inner ring at $r_0 = 0.557R_0$. Parameters used: confinement $\hbar\omega_0 = 3.60$ meV, dielectric constant $\kappa = 13.1$, effective mass $m^* = 0.067m_e$. Lengths in units of $R_0 = (2e^2/m^*\kappa\omega_0^2)^{1/3}$. CPDs (vertical axes) in arbitrary units.
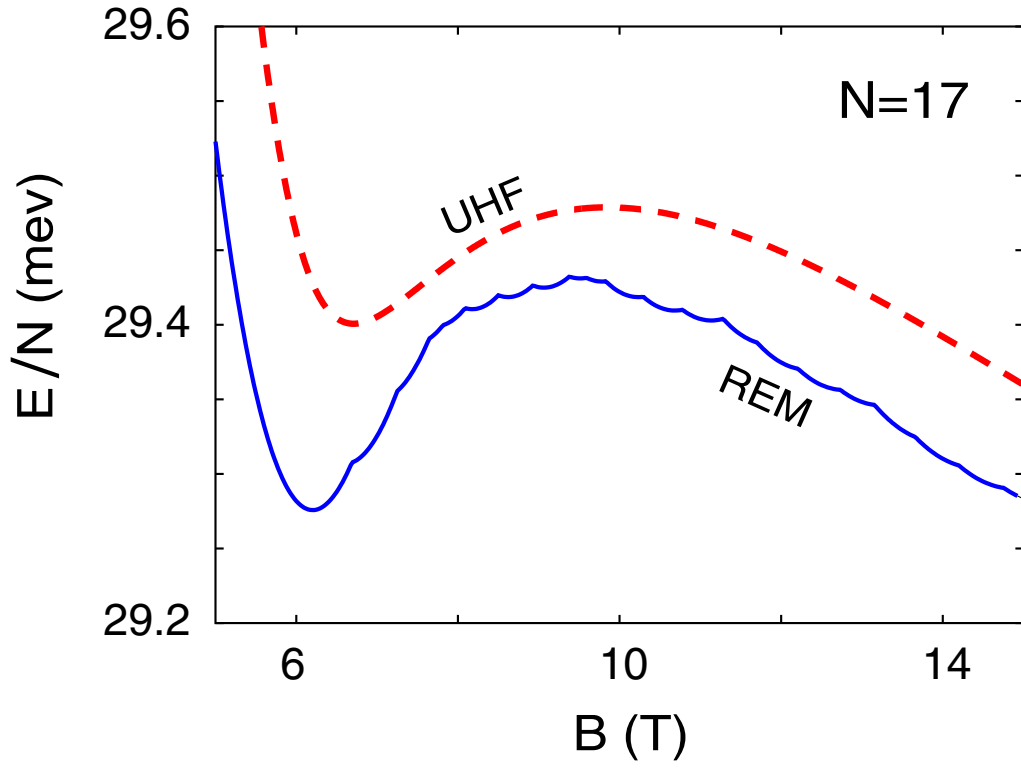
Figure 9: Ground-state energies (per particle, referenced to $\hbar\Omega$) for $N = 17$ electrons as a function of the magnetic field B. The electrons are arranged in a (1,6,10) structure. Dashed line (red): UHF. Solid line (blue): REM. Parameters used: confinement $\hbar\omega_0 = 3.6$ meV, dielectric constant $\kappa = 13.1$, effective mass $m^* = 0.067m_e$.

N=17
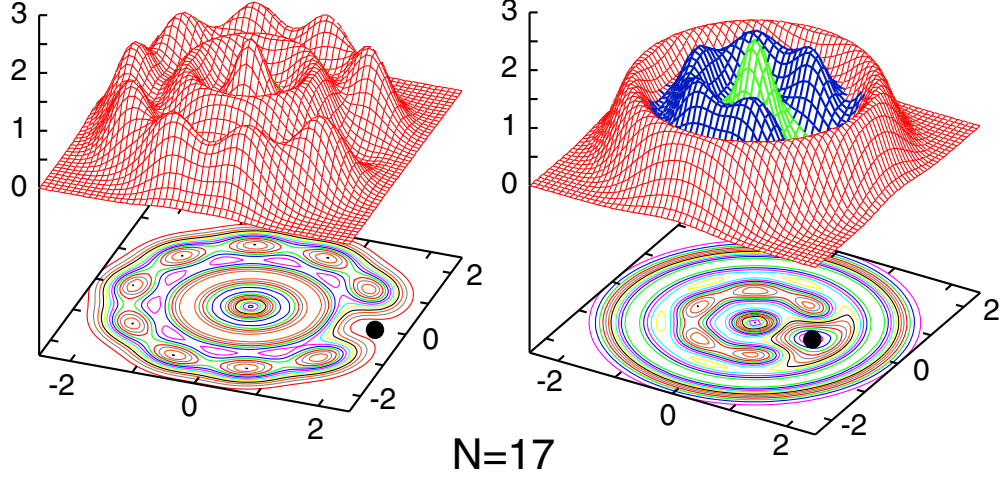
Figure 10: Grond-state conditional probability distributions, CPDs, obtained from REM wave functions for the ground state of $N = 17$ electrons at $B = 10$ T ($L = 228$). The electrons are arranged in a (1,6,10) structure. The observation point (solid dot) is placed on the outer ring at $r_0 = 1.858R_0$ (left frame), and on the inner ring at $r_0 = 0.969R_0$ (right frame). The rest of the parameters are the same as in Fig. 9. Lengths in units of $R_0 = (2e^2/(\kappa m^* \omega_0^2))^{1/3}$. CPDs (vertical axes) in arbitrary units.

N=12
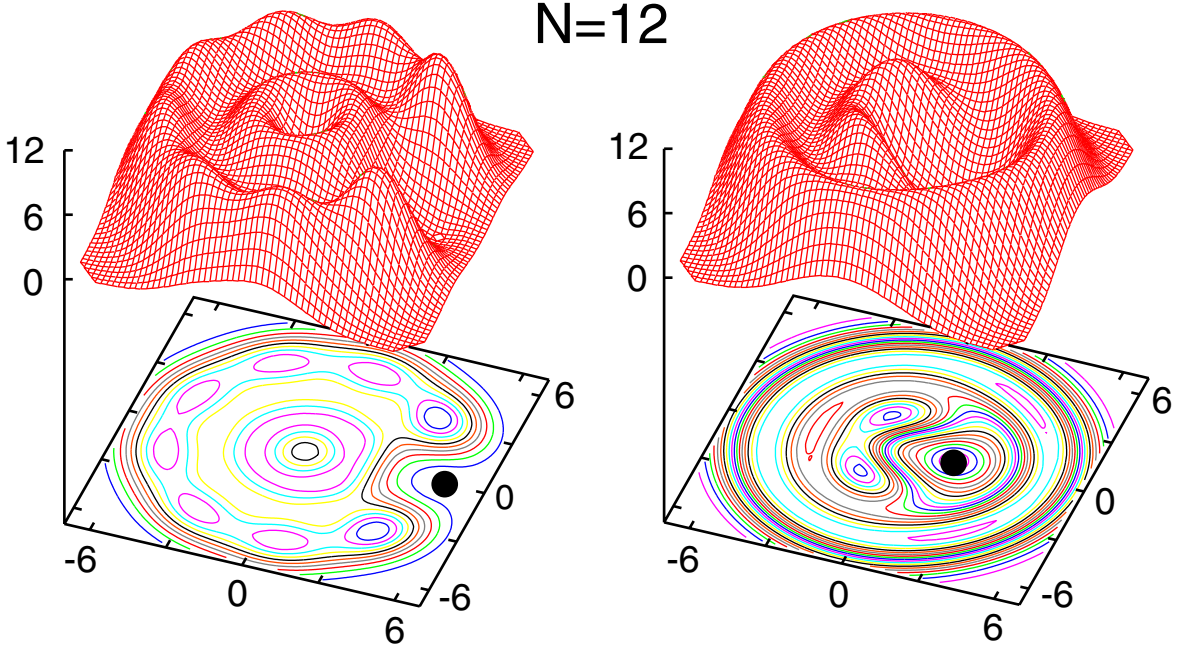
Figure 11: CPDs for $N = 12$ electrons and with angular momentum $L = 132$ ($\nu = 1/2$) calculated with EXD in the lowest Landau level. The electrons are arranged in a (3,9) structure. The observation point (solid dot) is placed on the outer ring at $r_0 = 5.22l_B$ (left frame), and on the inner ring at $r_0 = 1.87l_B$ (right frame). Lengths in units of l_B. CPDs (vertical axes) in arbitrary units.

46
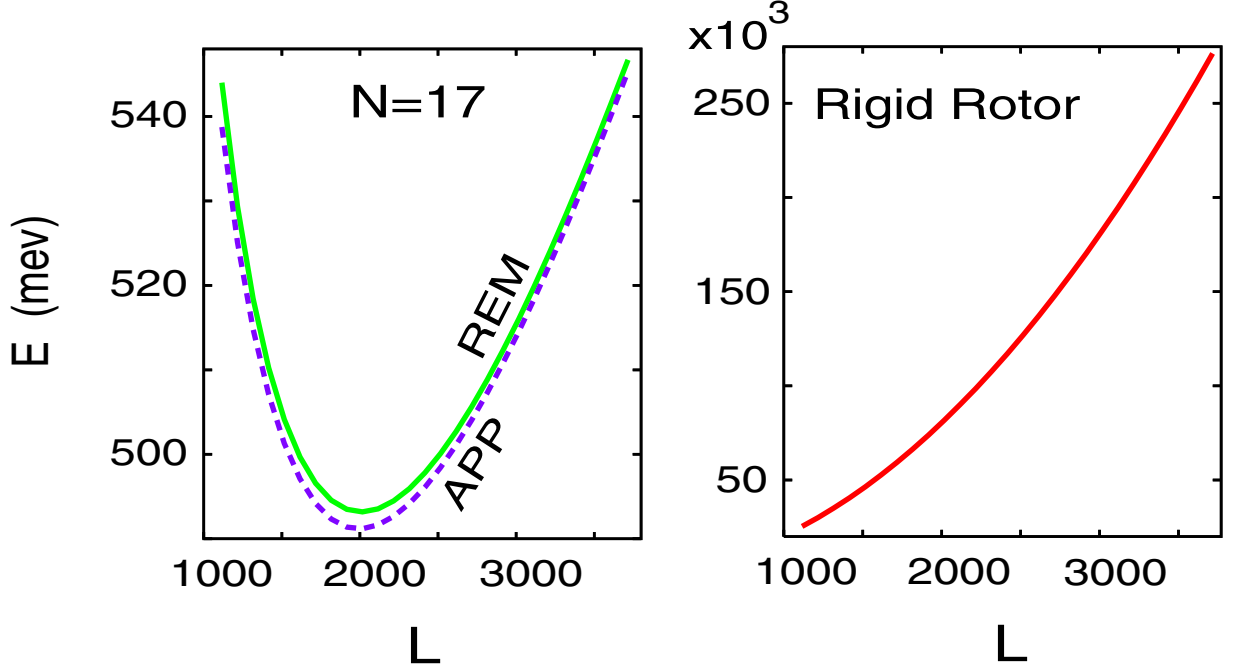
Figure 12: Left: Yrast spectrum for $N = 17$ electrons at a high magnetic field $B = 100$ T. Approximate analytic expression [Eq. (25), dashed line (violet)] compared with microscopic REM calculations [Eq. (11), solid line (green)]. Right: The corresponding classical (rigid rotor) energy E_L^{rig} for $N = 17$ electrons (see text). The microscopic REM energies are referenced relative to the zero-point energy, $17\hbar\Omega$. Energies were calculated for magic angular momenta $L = L_1 + L_2 + L_3$ with $L_1 = 0$, $L_2 = 21 + 6k_2$ and $k_2 = 30$, and $L_3 = 115 + 10k_3$. The parameters are the same as in Fig. 9. Note the much larger energy scale for the classical case (right frame), leading to a non-rigidity index for the REM of $\alpha \sim 0.99$ (see text).

CHAPTER III

EXACT DIAGONALIZATION FOR ELLIPTICAL DOTS

3.1 Outline of the exact diagonalization many-body method

We consider three electrons under zero or low magnetic field (B) in a single quantum dot. The corresponding many-body Hamiltonian is written as

$$\mathcal{H} = \sum_{i=1}^{3} H(i) + \sum_{j>i=1}^{3} \frac{e^2}{\kappa|\mathbf{r}_i - \mathbf{r}_j|}, \tag{30}$$

where κ is the dielectric constant of the semiconductor material (12.5 for GaAs). The single-particle Hamiltonian is given by

$$H = T + V(x,y) + \frac{g^* \mu_B}{\hbar} B\sigma, \tag{31}$$

where the last term is the Zeeman interaction, with g^* being the effective Landé factor, μ_B the Bohr magneton, B the perpendicular magnetic field, and $\sigma = \pm 1/2$ the spin projection of an individual electron. The kinetic contribution in Eq. (31) is given by

$$T = \frac{[\mathbf{p} - (e/c)\mathbf{A}(\mathbf{r})]^2}{2m^*}, \tag{32}$$

with m^* being the effective mass ($0.067 m_e$ for GaAs) and the vector potential $\mathbf{A}(\mathbf{r}) = 0.5(-By\hat{\imath} + Bx\hat{\jmath})$ being taken according to the symmetric gauge. The external confining potential is denoted as $V(x,y)$, where $\mathbf{r} = x\hat{\imath} + y\hat{\jmath}$.

The external potential is modeled by an anisotropic 2D Harmonic oscillator

$$V(x,y) = \frac{1}{2}m^*(\omega_x^2 x^2 + \omega_y^2 y^2), \tag{33}$$

which reduces to a circular parabolic QD for $\omega_x = \omega_y = \omega_0$. The ratio $\eta = \omega_x/\omega_y$ characterizes the degree of anisotropy of the quantum dot, and it will be referred

to thereafter as the anisotropy parameter. Results will be presented for three cases: $\eta = 1$ (circular), $\eta = 0.724$ (slightly anisotropic), and $\eta = 1/2$ (strongly anisotropic).

We find the eigenstates of the many-body Hamiltonian (30) using an exact diagonalization method. Accordingly, we expand the many-body wave function as a linear superposition,

$$\Psi^{\text{EXD}}(\mathbf{r}_1, \mathbf{r}_2, \mathbf{r}_3) = \sum_{1 \leq i < j < k \leq 2K} \mathcal{A}_{ijk} |\psi(1; i)\psi(2; j)\psi(3; k)\rangle, \tag{34}$$

where $|\psi(1; i)\psi(2; j)\psi(3; k)\rangle$ denotes a Slater determinant made out of the three spin-orbitals $\psi(1; i)$, $\psi(2; j)$, and $\psi(3; k)$. For the spin orbitals, we use the notation $\psi(1; i) = \varphi_i(1 \uparrow)$ if $1 \leq i \leq K$ and $\psi(1; i) = \varphi_{i-K}(1 \downarrow)$ if $K + 1 \leq i \leq 2K$ [and similarly for $\psi(2; j)$ and $\psi(3; k)$]. K is the maximum number of space orbitals $\varphi_i(\mathbf{r})$ that are considered, with $\varphi_i(l \uparrow) \equiv \varphi_i(\mathbf{r}_l)\alpha$ and $\varphi_i(l \downarrow) \equiv \varphi_i(\mathbf{r}_l)\beta$ where α and β denote up and down spins, respectively. The space orbitals $\varphi_i(\mathbf{r})$ are taken to coincide with the real eigenfunctions of a 2D anisotropic oscillator, that is, the index $i \equiv (m, n)$ and $\varphi_i(\mathbf{r}) = X_m(x)Y_n(y)$, with $X_m(Y_n)$ being the eigenfunctions of the corresponding one-dimensional oscillators in the $x(y)$ direction with frequency $\omega_x(\omega_y)$. The parity operator $\mathcal{P}$ yields $\mathcal{P}X_m(x) = (-1)^m X_m(x)$, and similarly for $Y_n(y)$.

The total energies E_{EXD} and the coefficients $\mathcal{A}_{ijk}$'s are obtained through a direct numerical diagonalization of the matrix eigenvalue equation corresponding to the Hamiltonian in Eq. (30). For the solution of this large scale, but sparse, matrix eigenvalue problem, we have used the ARPACK computer code.[64]

The EXD wave function (34) preserves by construction the third projection S_z of the total spin, since only Slater determinants with a given S_z value are used in the expansion. The exact diagonalization automatically produces eigenfunctions of the square, $\hat{\mathbf{S}}^2$, of the total spin $\hat{\mathbf{S}} = \sum_{i=1}^{3} \hat{\sigma}_i$. The corresponding eigenvalues $\hbar^2 S(S + 1)$ are calculated with the help of the expression

$$\hat{\mathbf{S}}^2|\text{SD}\rangle = \left[(N_\alpha - N_\beta)^2/4 + N/2 + \sum_{i<j} \varpi_{ij} \right] |\text{SD}\rangle, \tag{35}$$

where $|SD\rangle$ denotes a Slater determinant and the operator ϖ_{ij} interchanges the spins of electrons i and j provided that their spins are different; N_α and N_β denote the number of spin-up and spin-down electrons, respectively, while N denotes the total number of electrons.

Since the spin orbitals ψ's are orthogonal, the Coulomb matrix elements between two Slater determinants are calculated using the Slater rules,[65] and the necessary two-body matrix elements between space orbitals

$$\int \int d\mathbf{r}_1 d\mathbf{r}_2 \varphi_i^*(\mathbf{r}_1) \varphi_j^*(\mathbf{r}_2) \frac{1}{|\mathbf{r}_1 - \mathbf{r}_2|} \varphi_k(\mathbf{r}_1) \varphi_l(\mathbf{r}_2) \tag{36}$$

are calculated numerically via a center-of-mass transformation which eliminates the divergence at $|\mathbf{r}_1 - \mathbf{r}_2| = 0$. We have found that this method produces numerically stable results in comparison with algebraic expressions.[66]

3.2 Energy spectra of anistropic quantuam dots

In this section, we study the ground-state and excitation spectra as a function of an increasing magnetic field B with an emphasis on the role of correlation effects and the influence of the anisotropy.

To better understand the importance of correlations, we first display in Fig. 13 the spectra in the absence of the Coulomb interaction (non-interacting electrons) and for the case of a circular quantum dot. The main trend is the formation of three-particle Landau bands (each with an infinite number of states) that tend for $B \to \infty$ to the asymptotic energy levels $(\mathcal{M}+3/2)\hbar\omega_c$, $\mathcal{M} = 0, 1, 2, \ldots$ In this limit, the states (S, L), belonging to the same Landau band $\mathcal{M}$, become degenerate in energy, converging to the the corresponding familiar Landau level (with index $\mathcal{M}$). Apart from an overall constatnt, the picture in Fig. 13 is the same as that found in the phenomenological "constant interaction." model[67] An important property is the absence of crossings between individual levels within each Landau band. A consequence of this is that the
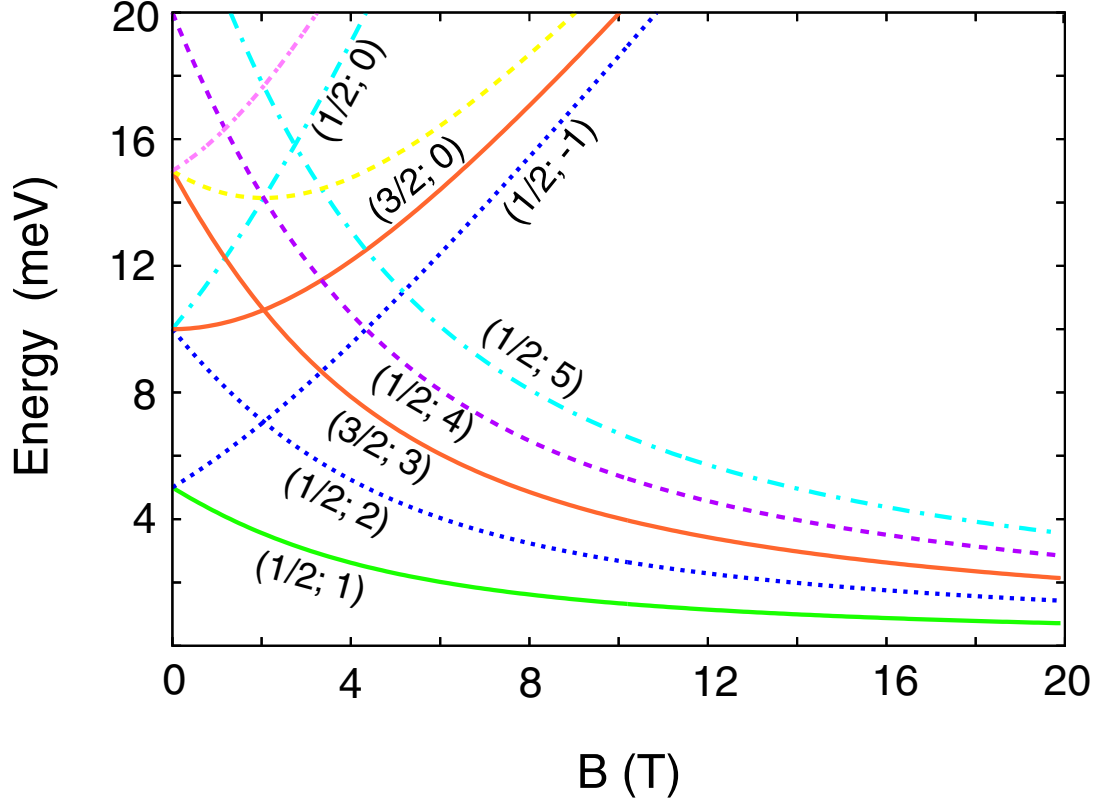
Figure 13: Ground-state and excitation energy spectra (after the substraction of $3\hbar\sqrt{(\omega_x^2 + \omega_y^2)/2 + \omega_c^2/4}$) as a function of the magnetic field for $N = 3$ non-interacting electrons in a circular quantum dot ($\eta = 1$). Parameters: external confinement $\hbar\omega_x = \hbar\omega_y = 5$ meV; dielectric constant $\kappa = \infty$; effective mass $m^* = 0.067 m_e$, effective Landé coefficient $g^* = 0$. The labels $(S; L)$ denote the quantum numbers for the total spin and the total angular momentum. Different Landau bands are denoted by the different $\mathcal{M}$ values.

ground state at any B has the same quantum numbers as the one at $B = 0$, i.e., it has total spin $S = 1/2$ and total angular momentum $L = 1$.

Turning on the interaction introduces correlation effects that lead to important modifications of these spectra. Fig. 14 displays the corresponding spectra for the same circular quantum dot, but in the presence of a Coulomb repulsion with $\kappa = 12.5$ (GaAs). Of course, a first effect is the increase in the total energy, but the main difference from the non-interacting case in Fig. 13 is the presence of crossings between levels within the same Landau band. As a result, within the plotted range of magnetic fields, the ground-state total-spin quantum number remains $S = 1/2$ at the first
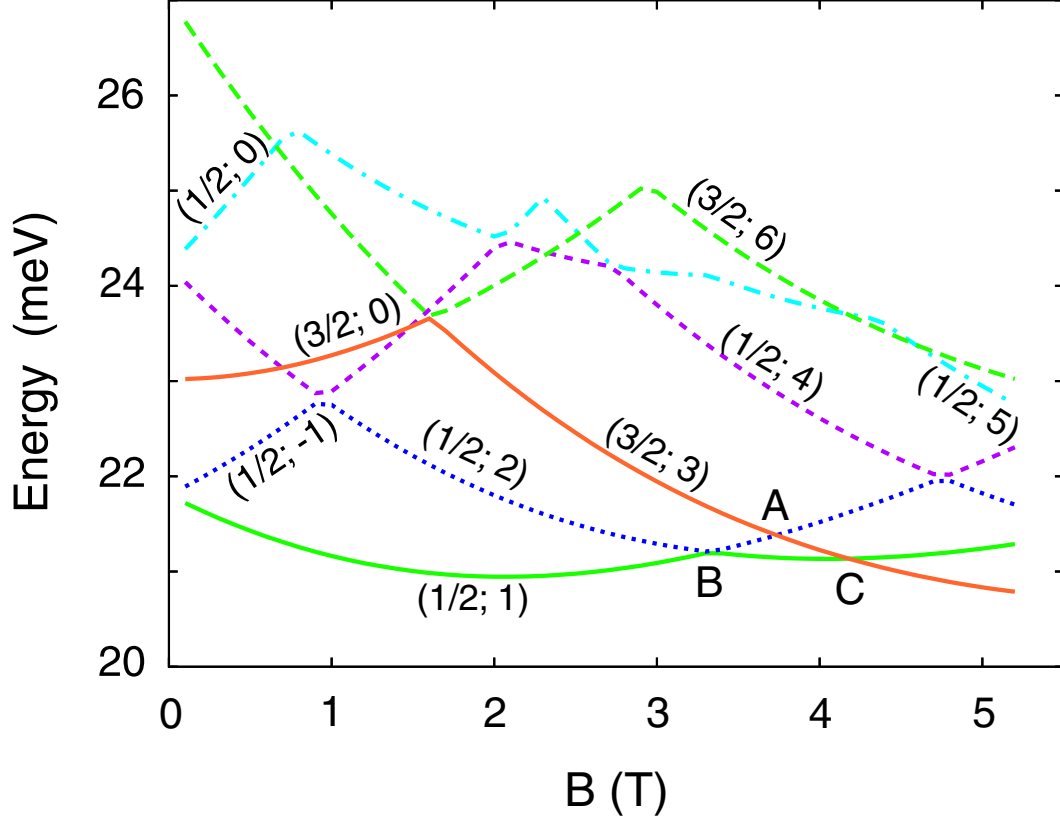
Figure 14: Ground-state and excitation energy spectra (after the substraction of $3\hbar\sqrt{(\omega_x^2 + \omega_y^2)/2 + \omega_c^2/4}$) as a function of the magnetic field for $N = 3$ interacting electrons in a circular quantum dot ($\eta = 1$). Parameters: external confinement $\hbar\omega_x = \hbar\omega_y = 5$ meV; dielectric constant $\kappa = 12.5$; effective mass $m^* = 0.067m_e$; effective Landé coefficient $g^* = 0$. The labels $(S; L)$ denote the quantum numbers for the total spin and the total angular momentum.

ground-state crossing (at point B), and then it changes to $S = 3/2$ (at the second ground-state crossing at point C). At the same time, the total angular momentum changes from $L = 1$, to $L = 2$, and then to $L = 3$, respectively. As long as the effective Landé coefficient $g^* = 0$, which is the case for the results presented in this section, this threefold alternation in the spin and angular momentum quantum numbers repeats itself ad-infinitum. We note that experimental observation of this threefold altenation may be forthcoming, since quantum dots with a vanishing Landé coefficient have been recently fabricated[25] and were used already to measure two-electron excitation spectra.

The crossings of the curves associated with the three different pairs of quantum numbers $(S, L) = (1/2, 1)$, $(1/2; 2)$, and $(3/2; 3)$ form a small triangle (labeled as ABC), which is located about $B \sim 3.8$ T. Anticipating the investigations for non-circular dots below, we note that this triangle tends to collapse to a single point with increasing anisotropy.
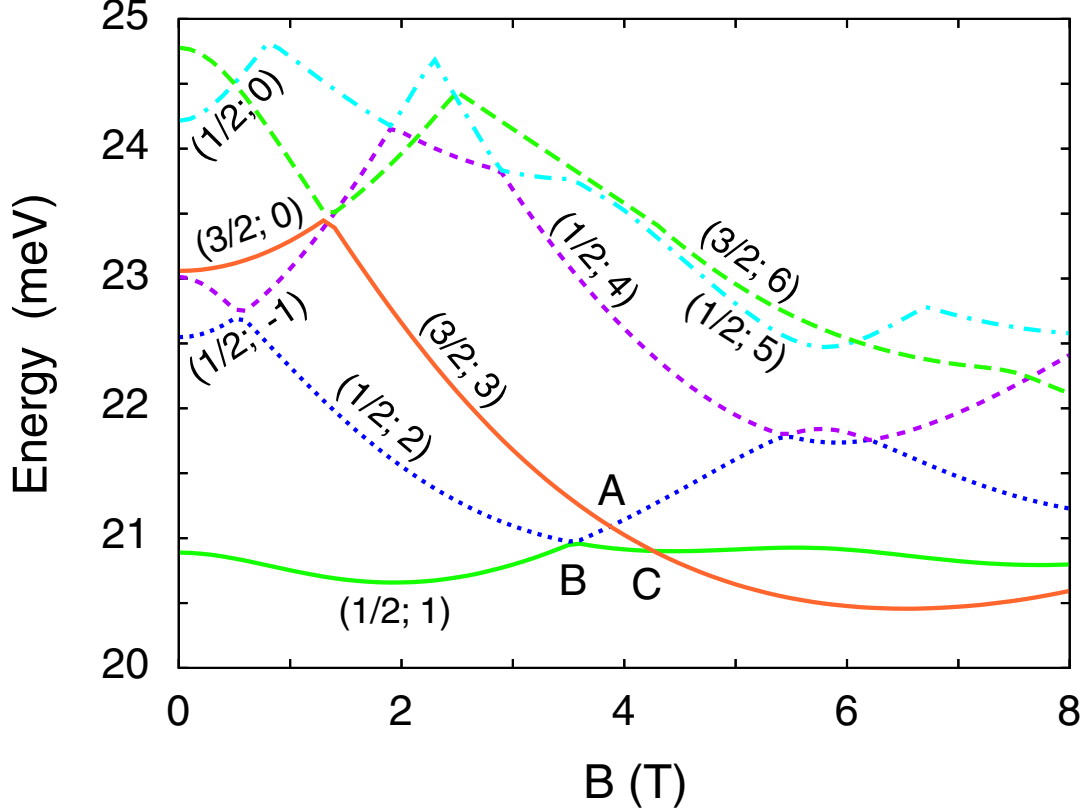
Figure 15: Ground-state and excitation energy spectra (after the substraction of $3\hbar\sqrt{(\omega_x^2 + \omega_y^2)/2 + \omega_c^2/4}$) as a function of the magnetic field for $N = 3$ interacting electrons in an elliptic quantum dot with intermediate anisotropy (anisotropy parameter $\eta = 0.724$). Parameters: external confinement $\hbar\omega_x = 4.23$ meV, $\hbar\omega_y = 5.84$ meV; dielectric constant $\kappa = 12.5$; effective mass $m^* = 0.070 m_e$; effective Landé coefficient $g^* = 0$. The labels $(S; L)$ denote the quantum numbers for the total spin and the total angular momentum in the corresponding circular quantum dot.

Another prominent difference between the non-interacting (Fig. 13) and interacting (Fig. 14) spectra is that the degeneracies at $B = 0$ between the $S = 3/2$ and $S = 1/2$ states are lifted in the interacting case [compare in particular the curves

with quantum numbers $(1/2; 2)$, $(1/2; 0)$, and $(3/2; 0)$]. On the contrary, the original degeneracies at $B = 0$ of the $S = 1/2$ states do maintain [compare the curves $(1/2, 1)$ and $(1/2, -1)$, as well as the ones labeled $(1/2, 2)$ and $(1/2, 0)$]. However, these $S = 1/2$ degeneracies at $B = 0$ are lifted as a result of an increasing anisotropy of the quantum dot, as seen in Fig. 15.
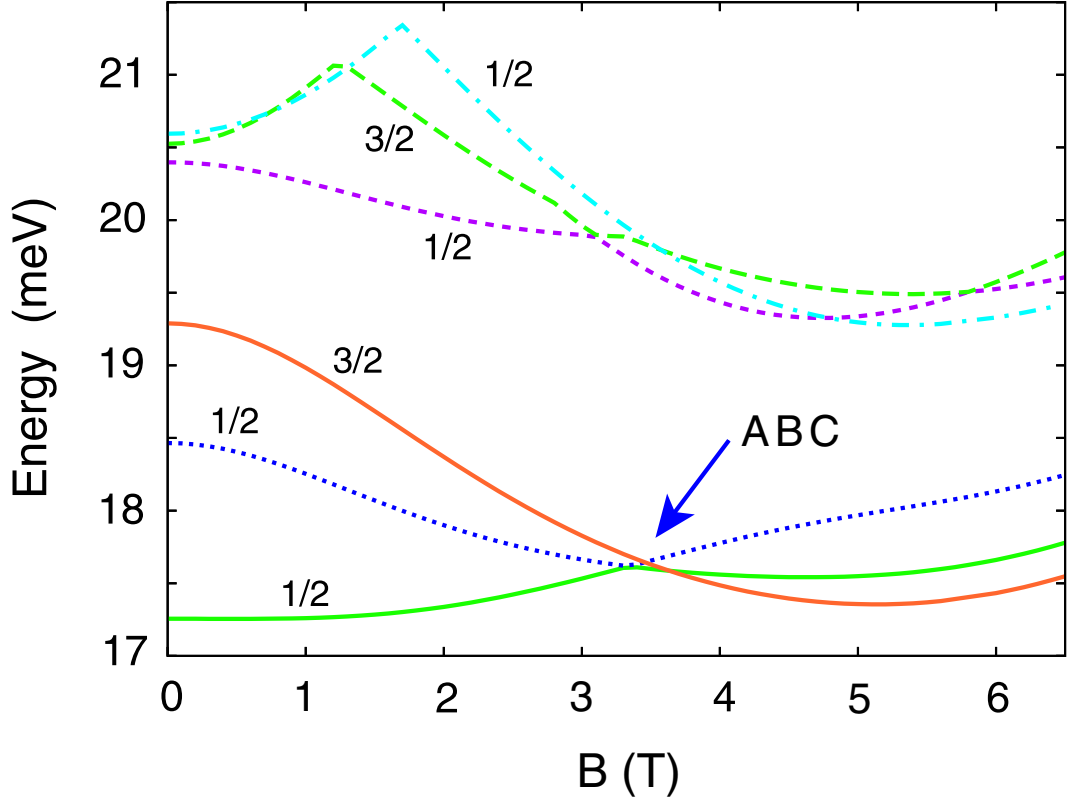
Figure 16: Ground-state and excitation energy spectra (after the substraction of $3\hbar\sqrt{(\omega_x^2 + \omega_y^2)/2 + \omega_c^2/4}$) as a function of the magnetic field for $N = 3$ electrons in an elliptic quantum dot with strong anisotropy (anisotropy parameter $\eta = 1/2$). Parameters: external confinement $\hbar\omega_x = 3.137$ meV, $\hbar\omega_y = 6.274$ meV; dielectric constant $\kappa = 12.5$; effective mass $m^* = 0.067m_e$; effective Landé coefficient $g^* = 0$. The single labels denote the quantum numbers for the total spin.

Next, we proceed with futher elaborating on our investigations regarding the effect of increasing anisotropy of the quantum dot. In particular, keeping the same strength for the Coulomb interaction ($\kappa = 12.5$), we present two representative anisotropy cases, i.e., $\eta = 0.724$ (intermediate anisotropy, see Fig. 15), and $\eta = 1/2$ (strong

anisotropy closer to a quasilinear case, see Fig. 16).

Inspecting the results for the case of intermediate anisotropy (Fig. 15), we see that compared to Fig. 14 the spectra are distorted, but they maintain the overall topology of the circular dot. As a result, we have been able to use the same pairs of labels in naming the different curves, even though the second label does not have the meaning of an angular momentum (the total angular momentum is not conserved for $\eta \neq 1$). There are two main differences for the circular case: i) the degeneracies at $B = 0$ between the $S = 1/2$ states are lifted, and ii) there is a marked rounding of all the $S = 1/2$ curves in the beginning, so that they do not cross the vertical energy axis at sharp angles as is the case with Fig. 14. This initial rounding and bending of the energy curves due to the anisotropy has been experimentally observed[25, 68] in two-electron quantum dots.

In the case of strong anisotropy (Fig. 16), the spectra have evolved to such an extent that little relation to the circular case can be traced, and as a result we use the single label of the total spin to distinguish them. An important feature is that the three curves with lowest energies (two $S = 1/2$ and one $S = 3/2$ curve) form a band that is well separated from the other excited states. The existence of such an isolated lowest-energy band is important for validating simple two-qubit and three-qubit models introduced in quantum computation and quantum information theory.[29, 69]

Another remarkable feature of the strong-anisotropy case is the appearance of a triple-point crossing in the ground-state curve (see arrow in Fig. 16), which is created from the collapse of the ABC triangle between the two $S = 1/2$ and the one $S = 3/2$ lowest-in-energy curves. We note that triple-point crossings have been recently observed experimentally in anisotropic quantum dots.[70]
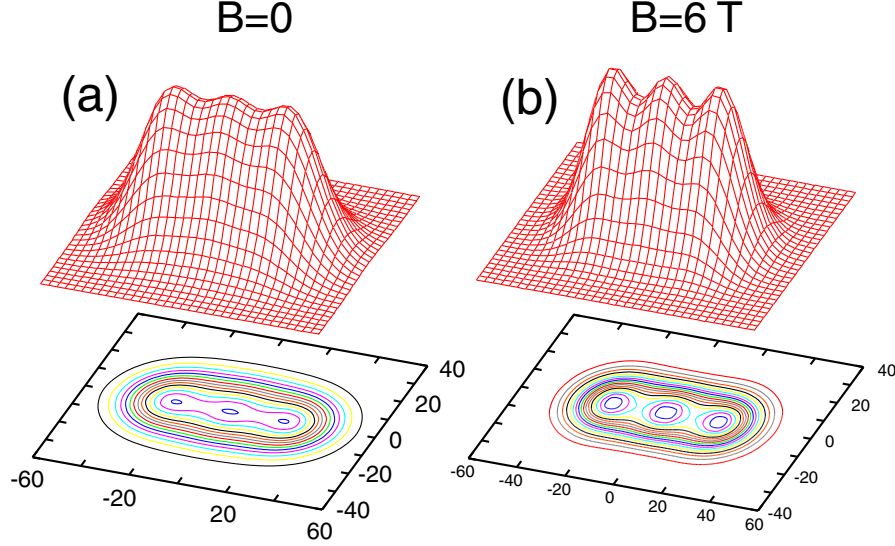
Figure 17: Exact-diagonalization electron densities for the ground states of $N = 3$ electrons in an anisotropic dot with parameters $\hbar\omega_x = 3.137$ meV, $\hbar\omega_y = 6.274$ meV ($\eta = 1/2$), effective mass $m^* = 0.067m_e$, dielectric constant $\kappa = 12.5$ (GaAs). (a): The case of zero magnetic field, $B = 0$. (b) The case with a magnetic field $B = 6$ T. Lengths in nm. The electron densities are in arbitrary units, but with the same scale in both panels.

3.3 Many-body wave functions for strong anisotropy ($\eta = 1/2$)

3.3.1 $S = 1/2$ ground states: Evolution of electron densities as a function of the inter-electron repulsion

When the confining potential lacks circular symmetry, charge localization is reflected directly in the single-particle electron densities. Indeed, electron localization is visible in Figs. 17 and 18, which display the electron densities for $N = 3$ electrons in an anisotropic quantum dot with $\eta = 1/2$. Fig. 17 illustrates the evolution of electron localization with increasing magnetic field in the case of a weaker Coulomb repulsion ($\kappa = 12.5$). One sees that already at $B = 0$, the electron density is linear for all practical purposes. However, the three peaks of the localized electrons are rather weak, which contrasts with the case of $B = 6$ T [Fig. 17(b)], where the three electron peaks are clearly stronger.

Fig. 18 [in conjunction with Fig. 17(a)] illustrates the strengthening of electron

56

localization as a function of increasing Coulomb repulsion, i.e., decreasing dielectric constant κ, from a value of 12.5 [Fig. 17(a)] to $\kappa = 3$ [Fig. 18(a)] and then to $\kappa = 1$ [Fig. 18(b)]. In this last case [Fig. 18(b)], the three electrons are almost fully localized, with orbitals that practically exhibit zero overlap.
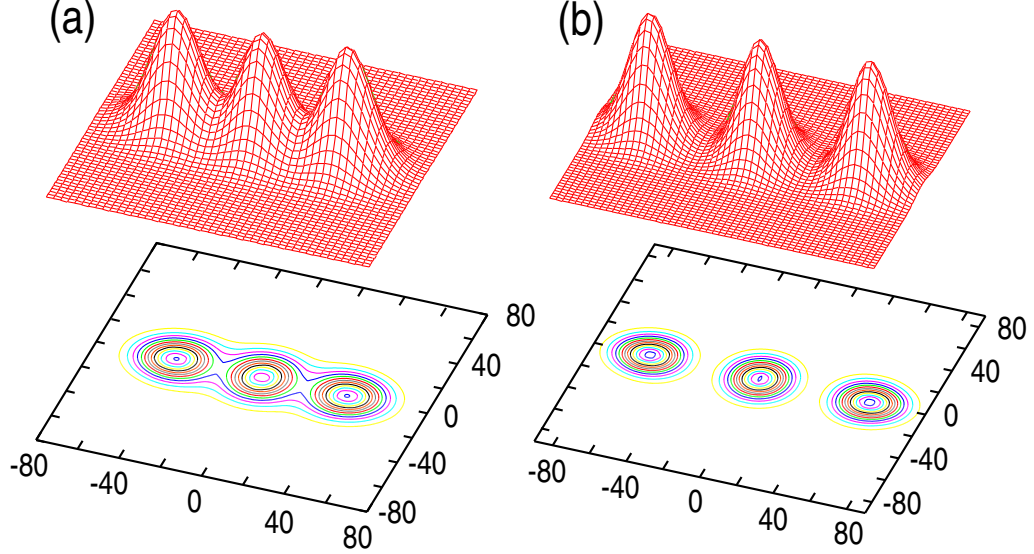
Figure 18: Exact-diagonalization electron densities at zero magnetic field ($B = 0$) for the ground state of $N = 3$ electrons in an anisotropic dot with parameters $\hbar\omega_x = 3.137$ meV, $\hbar\omega_y = 6.274$ meV ($\eta = 1/2$), $m^* = 0.067m_e$. (a): dielectric constant $\kappa = 3.0$. (b): dielectric constant $\kappa = 1.0$. Lengths in nm. The electron densities are in arbitrary units, but with the same scale as in Fig. 17 for both panels.

3.3.2 $S = 1/2$ ground state: Spin resolved intrinsic structure for strong repulsion ($\kappa = 1$).

In the previous section, we saw that the electron densities already provide partial information about the formation of a linear Wigner molecule within an elliptic quantum dot. Indeed, from the charge distributions in Figs. 17 and 18, one can guess that the electrons are localized in three separate positions $\mathbf{R}_1$, $\mathbf{R}_2$, and $\mathbf{R}_3$. If the electrons were spinless, this situation could be approximately reproduced by a single Slater determinant denoted as $|\bigcirc\,\bigcirc\bigcirc\rangle$. However, to probe the spin distribution of the electrons, the exact-diagonalization charge densities do not suffice; one needs to

consider spin-resolved two-point correlation functions, defined as

$$P_{\sigma\sigma_0}(\mathbf{r}, \mathbf{r}_0) =$$

$$\langle \Psi^{\text{EXD}} | \sum_{i \neq j} \delta(\mathbf{r} - \mathbf{r}_i)\delta(\mathbf{r}_0 - \mathbf{r}_j)\delta_{\sigma\sigma_i}\delta_{\sigma_0\sigma_j} | \Psi^{\text{EXD}} \rangle, \tag{37}$$

where naturally the EXD many-body wave function is given by equation (34).

Using a normalization constant

$$\mathcal{N}(\sigma, \sigma_0, \mathbf{r}_0) = \int P_{\sigma\sigma_0}(\mathbf{r}, \mathbf{r}_0)d\mathbf{r}, \tag{38}$$

we further define a related conditional probability distribution (CPD) as

$$\mathcal{P}_{\sigma\sigma_0}(\mathbf{r}, \mathbf{r}_0) = P_{\sigma\sigma_0}(\mathbf{r}, \mathbf{r}_0)/\mathcal{N}(\sigma, \sigma_0, \mathbf{r}_0), \tag{39}$$

having the property $\int \mathcal{P}_{\sigma\sigma_0}(\mathbf{r}, \mathbf{r}_0)d\mathbf{r} = 1$.

Before examining such numerical EXD CPDs, however, it is instructive to consider on a qualitative level the spin structure of the wave functions that can be formed with only three localized spin-orbitals. In particular, we focus on the case with a total spin projection $S_z = 1/2$, when the most general three-orbital wave function is given by the expression

$$\Phi(S_z = \tfrac{1}{2}) = a|\uparrow\downarrow\uparrow\rangle + b|\uparrow\uparrow\downarrow\rangle + c|\downarrow\uparrow\uparrow\rangle, \tag{40}$$

with the normalization $a^2 + b^2 + c^2 = 1$.

The general states (40) are a superposition of three Slater determinants and have attracted a lot of attention in the mathematical theory of entanglement. Indeed, they represent a prototypical class of three-qubit entangled states known as W-states.[35] For general coefficients a, b, and c, the states (40) are not eigenfunctions of the square of total spin $\hat{\mathbf{S}}^2$, as is always the case with the exact-diagonalization wave functions in Eq. (34). However, the special values of these coefficients that lead to good total-spin quantum numbers are known ([30, 71]). In particular, using the notation $\Phi(S, S_z; i)$

(where the index i is employed in case of a degeneracy), one has

$$\sqrt{3}\Phi(\tfrac{3}{2},\tfrac{1}{2}) = |\uparrow\downarrow\uparrow\rangle + |\uparrow\uparrow\downarrow\rangle + |\downarrow\uparrow\uparrow\rangle \tag{41}$$

(i.e., $a = b = c = 1/\sqrt{3}$),

$$\sqrt{6}\Phi(\tfrac{1}{2},\tfrac{1}{2};1) = 2|\uparrow\downarrow\uparrow\rangle - |\uparrow\uparrow\downarrow\rangle - |\downarrow\uparrow\uparrow\rangle \tag{42}$$

(i.e., $a = 2/\sqrt{6}$, $b = c = -1/\sqrt{6}$),

$$\sqrt{2}\Phi(\tfrac{1}{2},\tfrac{1}{2};2) = |\uparrow\uparrow\downarrow\rangle - |\downarrow\uparrow\uparrow\rangle \tag{43}$$

(i.e., $a = 0$, $b = 1/\sqrt{2}$, $c = -1/\sqrt{2}$).

For completeness, we list the case for three fully spin-polarized localized electrons (which of course is not a W-state).

$$\Phi(\tfrac{3}{2},\tfrac{3}{2}) = |\uparrow\uparrow\uparrow\rangle. \tag{44}$$

The wave functions with projections $S_z = -1/2$ and $S_z = -3/2$ are similar to the above, but with inverted single-particle spins.
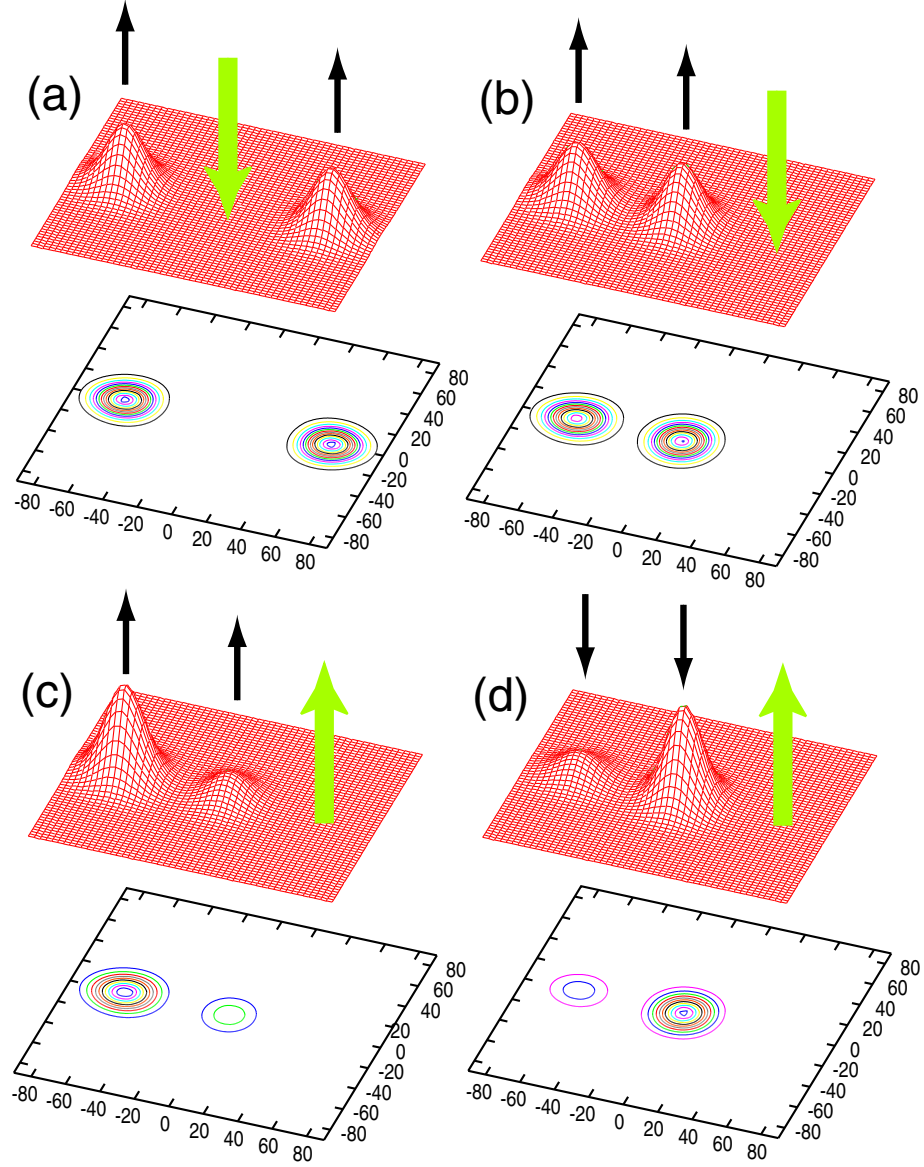
Figure 19: Spin-resolved conditional probability distributions for the (1/2,1/2) ground state of $N = 3$ electrons in an anisotropic dot at zero magnetic field ($B = 0$) with parameters $\hbar\omega_x = 3.137$ meV, $\hbar\omega_y = 6.274$ meV ($\eta = 1/2$), $m^* = 0.067m_e$ and $\kappa = 1$. (a) $\downarrow\uparrow$ CPD with the fixed spin-down electron located at the center. (b) $\downarrow\uparrow$ CPD with the fixed spin-down electron located on the right. (c) $\uparrow\uparrow$ CPD with the fixed spin-up electron located on the right. (d) $\uparrow\downarrow$ CPD with the fixed spin-up electron located on the right. The spin of the fixed electron is denoted by a thick arrow (green online). Lengths in nanometers. The vertical axes are in arbitrary units, but the scale is the same for all four panels.

In Fig. 19, we present several spin-resolved CPDs associated with the EXD ground state at $B = 0$ and strong anisotropy $\eta = 1/2$, which is a $\Psi^{\text{EXD}}(1/2, 1/2)$ state [see Fig. 16]. Although the EXD expansion in Eq. (34) consists of a large number of Slater determinants built from delocalized harmonic-oscillator orbitals, the CPD patterns in Fig. 19 reveal an intrinsic structure similar to that of the wave function $\Phi(\frac{1}{2}, \frac{1}{2}; 1)$ in Eq. (42), which is made out of only three localized spin-orbitals. In particular, when one requires that the fixed electron has a down spin and is located at the center of the quantum dot, the spin-up electrons are located on the left and right with equal weights [Fig. 19(a)]. Keeping the down spin-direction, but moving the fixed electron to the right, reveals that the spin-up electrons are located on the left and the center with equal weights [Fig. 19(b)]. Considering a spin-up direction for the fixed electron and placing it on the right reveals that the remaining spin-up electron is distributed on the left and the center of the quantum dot with unequal weights; approximately 4 (left) to 1 (center) following the square of the coefficients in front of the determinants $|\!\uparrow\downarrow\uparrow\rangle$ $(a = 2/\sqrt{6})$ and $|\!\downarrow\uparrow\uparrow\rangle$ $(c = 1/\sqrt{6})$ in the wave function $\Phi(\frac{1}{2}, \frac{1}{2}; 1)$. Similarly, considering a spin-up direction for the fixed electron and placing it on the right reveals that the spin-down electron is distributed on the left and the center of the quantum dot with unequal weights – approximately 1 (left) to 4 (center), in agreement with the weights of the Slater determinants in Eq. (42).

3.3.3 $S = 3/2$ excited state: Spin resolved intrinsic structure for strong repulsion ($\kappa = 1$).

In section 3.3.2, we investigated the intrinsic structure of the many-body three-electron wave functions with total spin $S = 1/2$ and for the case of a strong anisotropy $\eta = 1/2$. In this section, we analyze a case of an EXD wave function with total spin $S = 3/2$ and for the same strong anisotropy $\eta = 1/2$, again at $B = 0$ T. In particular, we analyze the intrinsic structure of a $\Psi^{\text{EXD}}(3/2, 1/2)$ wave function that is an excited state for these parameters.
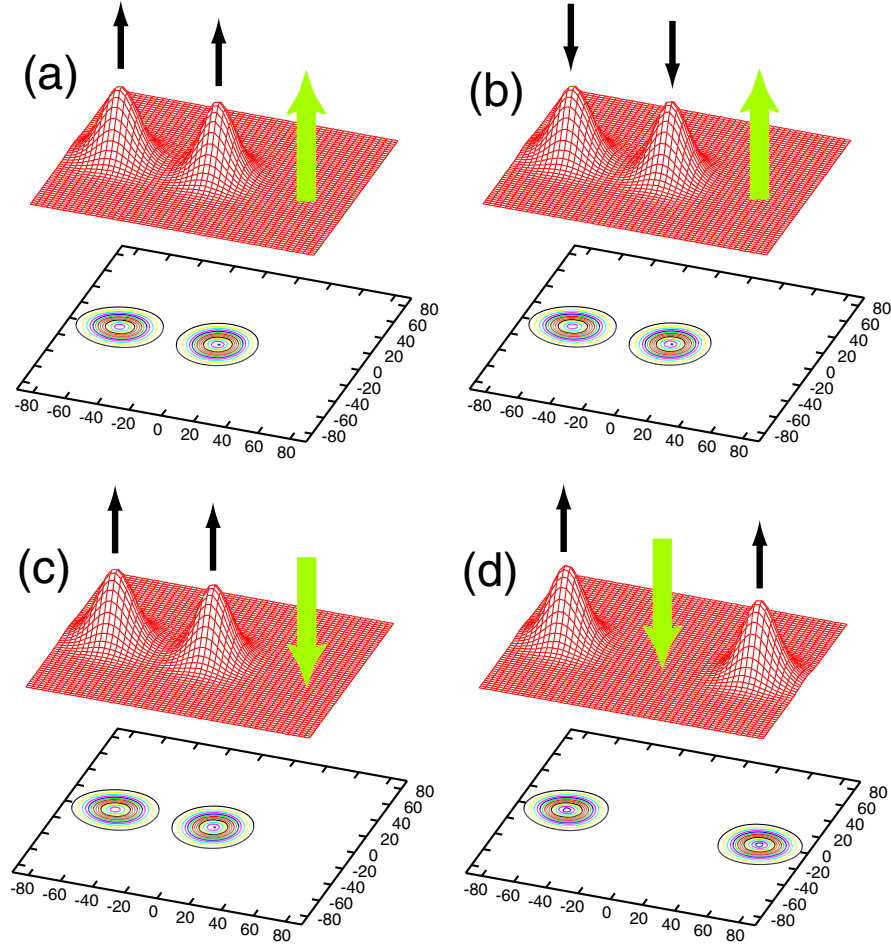
Figure 20: Spin-resolved conditional probability distributions for the $(3/2,1/2)$ second excited state of $N = 3$ electrons in an anisotropic dot at zero magnetic field ($B = 0$) with parameters $\hbar\omega_x = 3.137$ meV, $\hbar\omega_y = 6.274$ meV ($\eta = 1/2$), $m^* = 0.067m_e$ and $\kappa = 1$. (a) $\uparrow\uparrow$ CPD with the fixed spin-up electron located on the right at (70,0). (b) $\uparrow\downarrow$ CPD with the fixed spin-up electron located on the right at (70,0). (c) $\downarrow\uparrow$ CPD with the fixed spin-down electron located on the right at (70,0). (d) $\downarrow\uparrow$ CPD with the fixed spin-down electron located at the center. The spin of the fixed electron is denoted by a thick arrow (green online). Lengths in nanometers. The vertical axes are in arbitrary units, but the scale is the same for all four panels.

In Fig. 20, we display spin-resolved CPDs for this $S = 3/2$ excited state. A remarkable feature is that for a fixed electron placed on the right all three CPDS, ↑↑ [Fig. 20(a)], ↑↓ [Fig. 20(b)], and ↓↑ [Fig. 20(c)] coincide. This indicates that the intrinsic structure of the $\Psi^{\text{EXD}}(3/2, 1/2)$ wave function is close to that of $\Phi(\frac{3}{2}, \frac{1}{2})$ in Eq. (41), with all three coefficients $a = b = c$.

Taking into account the ↓↑ CPD with the fixed electron at the center of the quantum dot, it is clear that the geometric arrangement of the three localized electrons is linear. More complicated than linear geometric arrangements can emerge, however, for a range of different parameters, as is discussed in section 3.4 below.

3.4 Many-body wave functions for intermediate anisotropy ($\eta = 0.724$) and moderate repulsion ($\kappa = 12.5$).

In this section, we analyze a case of an EXD wave function with total spin $S = 3/2$ and for the intermediate anisotropy $\eta = 0.724$. In particular, we analyze the intrinsic structure of a $\Psi^{\text{EXD}}(3/2, 1/2)$ wave function that is the ground state at a magnetic field $B = 5$ T (see Fig. 15).

In Fig. 21, we display spin-resolved CPDs for this ground state. A remarkable feature is that for a fixed electron placed on the right all three CPDS, ↑↑ [Fig. 21(a)], ↑↓ [Fig. 21(b)], and ↓↑ [Fig. 21(c)] coincide. This indicates that the intrinsic structure of the $\Psi^{\text{EXD}}(3/2, 1/2)$ wave function is close to that of $\Phi(\frac{3}{2}, \frac{1}{2})$ in Eq. (41), with all three coefficients $a = b = c$.
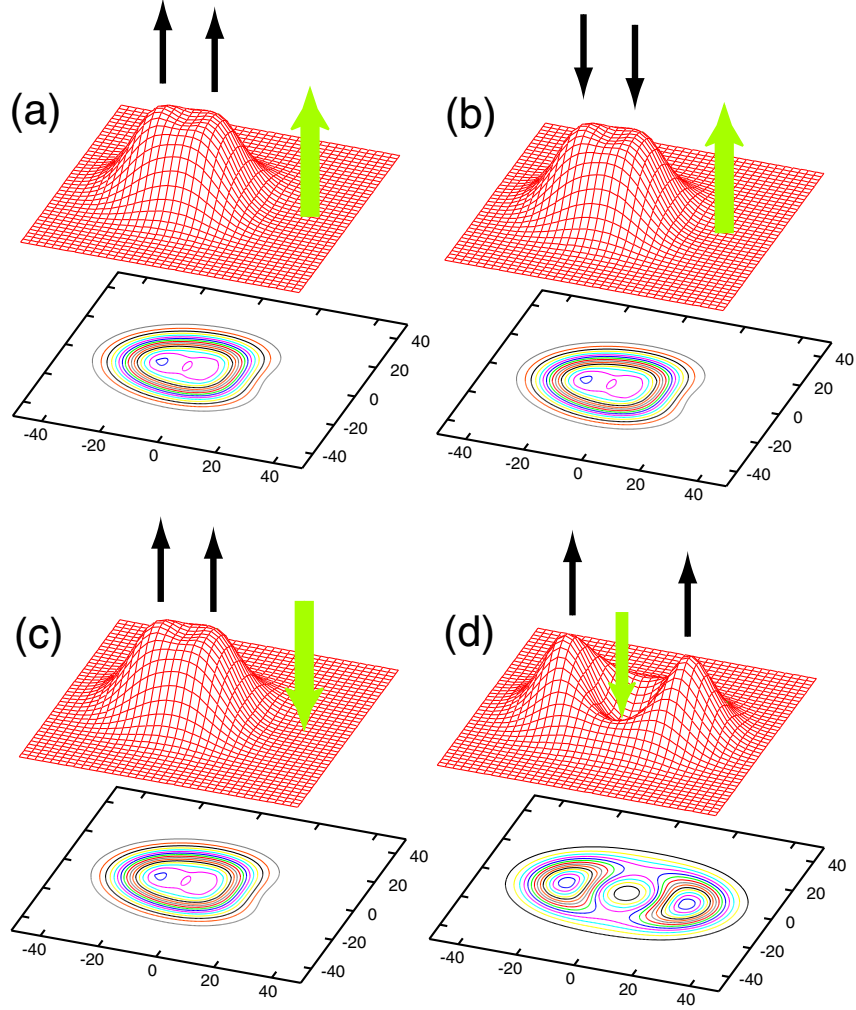
Figure 21: Spin-resolved conditional probability distributions for the (3/2,1/2) ground state of $N = 3$ electrons in an anisotropic dot at $B = 5$ T with parameters $\hbar\omega_x = 4.23$ meV, $\hbar\omega_y = 5.84$ meV ($\eta = 0.724$), $m^* = 0.070m_e$ and $\kappa = 12.5$. (a) $\uparrow\uparrow$ CPD with the fixed spin-up electron located on the right at (30,0). (b) $\uparrow\downarrow$ CPD with the fixed spin-up electron located on the right at (30,0). (c) $\downarrow\uparrow$ CPD with the fixed spin-down electron located on the right at (30,0). (d) $\downarrow\uparrow$ CPD with the fixed spin-down electron located at the center. The spin of the fixed electron is denoted by a thick arrow (green online). Lengths in nanometers. The vertical axes are in arbitrary units, but the scale is the same for all four panels.
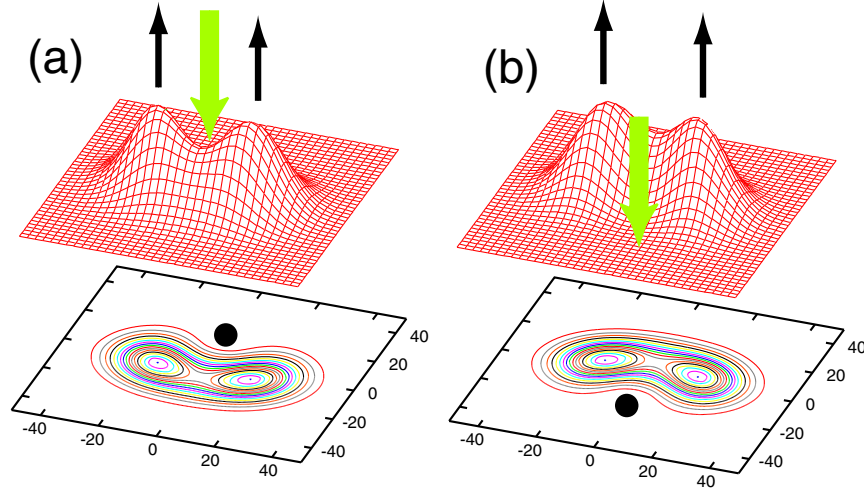
Figure 22: Spin-resolved conditional probability distributions for the $(3/2,1/2)$ ground state of $N = 3$ electrons in an anisotropic dot at $B = 5$ T with parameters $\hbar\omega_x = 4.23$ meV, $\hbar\omega_y = 5.84$ meV ($\eta = 0.724$), $m^* = 0.070m_e$ and $\kappa = 12.5$. (a) $\downarrow\uparrow$ CPD with the fixed spin-down electron located on the y-axis at $(0,20)$ (solid dot). (b) $\downarrow\uparrow$ CPD with the fixed spin-down electron located on the y-axis at $(0,-20)$ (solid dot). The spin of the fixed electron is denoted by a thick arrow (green online). Lengths in nanometers. The vertical axes are in arbitrary units, but the scale is the same for all panels in this figure and in Fig. 21.

However, the $\downarrow\uparrow$ CPD with the fixed spin-down electron at the center [Fig. 21(d)] differs from the one expected from a linear molecular arrangement [compare Fig. 20(d)], where there should be no maxima (along the y-direction) away from the x-axis. The presence of such maxima at points $(x, y \neq 0)$ in the $\downarrow\uparrow$ CPD in Fig. 21(d) suggests that the intrinsic structure of $\Psi^{\text{EXD}}(3/2, 1/2)$ is more complicated. Indeed, as demonstrated in Fig. 22 where the fixed spin-down electron is successively placed away from the x-axis at (0, 20 nm) and at (0, -20 nm), the intrinsic structure corresponds to a superposition of two molecular isomers, each one described by a three-orbital wave function $\Phi(\frac{3}{2}, \frac{1}{2})$, but with the three localized spin-orbitals located on the vertices of two isosceles triangles, each one being a mirror reflection (relative to the x-axis) of the other. The base of the first isosceles triangle lies -6 nm [Fig. 22(a)] and that of the second one at 6 nm [Fig. 22(a)] away from the x-axis.

The two-triangle configuration discussed for three electrons above may be seen as the embryonic precursor of a quasilinear structure of two intertwined "zig-zag" crystalline chains. Such *double* zig-zag crystaline chains may also be related to the *single* zig-zag Wigner-crystal chains discussed recently in relation to spontaneous spin polarization in quantum wires.[72, 73]

It is interesting to inquire of how this two-triangle structure is reflected in the charged densities. Indeed, in Fig. 23(a), we display the electron density associated with the (3/2,1/2) ground state at $B = 5$ T. To be noticed is the absence of a third peak at the center of the quantum dot. Instead, two rather small peaks appear at (0,20 nm) and (0,-20 nm), in agreement with the two-triangle internal structure revealed by the CPD analysis.

We further display in Fig. 23(b) the corresponding electron density for the $(1/2,1/2)$ ground state at $B = 0$. This latter density has the same features as the one in Fig. 23(a), which indicates that an $(1/2,1/2)$ state can have also a two-triangle internal configuration. Naturally, the regime of a linear configuration versus a two-triangle one depends on both the strength of the interaction and the anisotropy. Detailed studies of the phase boundary between these two intrinsic structures are, however, left for a future investigation.
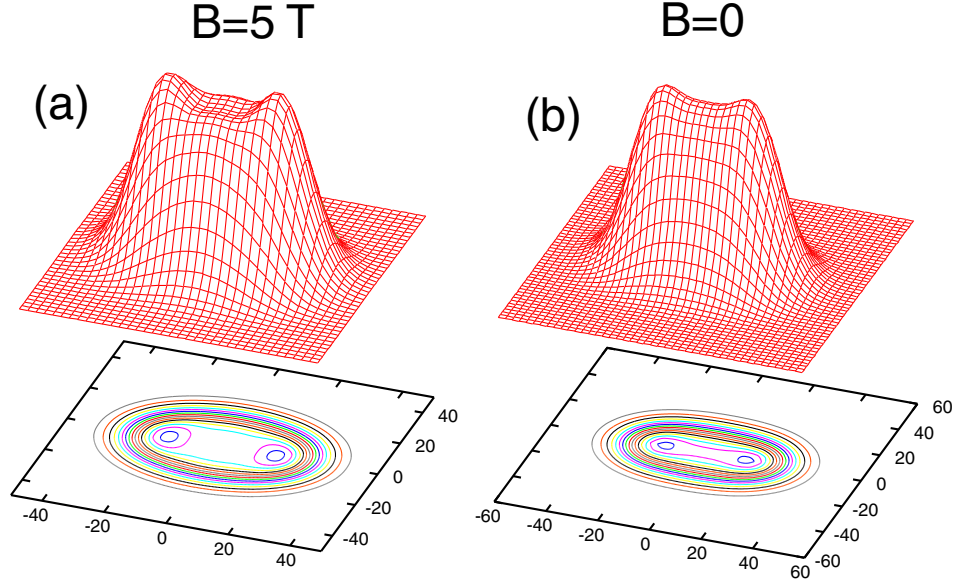
Figure 23: Exact-diagonalization electron densities for the ground state of $N = 3$ electrons in an anisotropic quantum dot with parameters $\hbar\omega_x = 4.23$ meV, $\hbar\omega_y = 5.84$ meV ($\eta = 0.724$), $m^* = 0.070 m_e$ and $\kappa = 12.5$. (a) the $(3/2,1/2)$ ground state at $B = 5$ T. (b) the $(1/2,1/2)$ ground state at $B = 0$. Lengths in nm. The electron densities are in arbitrary units, but with the same scale for both panels.

3.5   Degree of entanglement

The many-body wave functions for $N = 3$ electrons analyzed in previous sections are highly entangled states, since they cannot be reduced to a single Slater determinant. For special ranges of the dot parameters, we showed that they acquire the same internal structure as the prototypical W-states. In this section, we demonstrate that the degree of entanglement can be further quantified through the use of the von
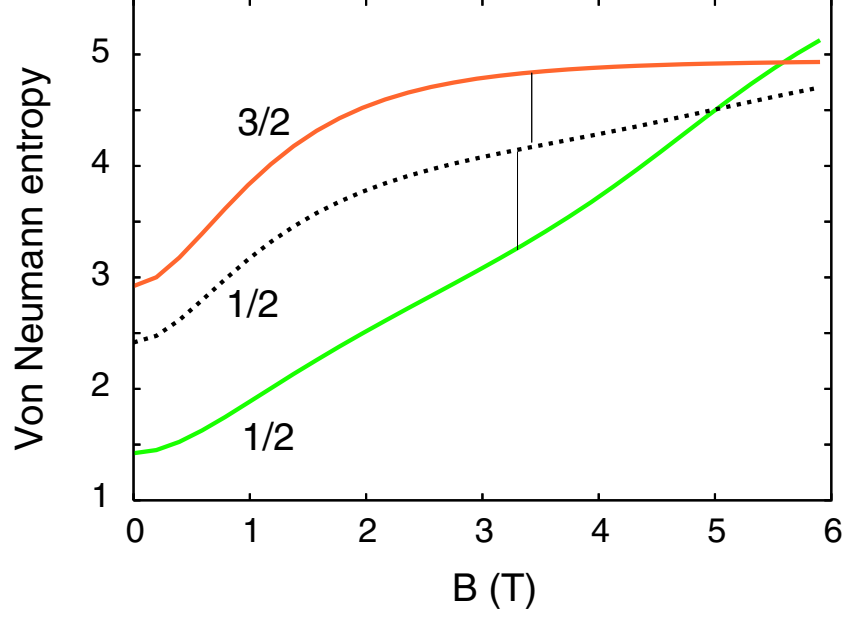
Figure 24: Von Neumann entropy for the three lowest EXD states with $S_z = 1/2$ as a function of the magnetic field for $N = 3$ electrons in an anisotropic quantum dot with strong anisotropy (anisotropy parameter $\eta = 1/2$). Parameters: external confinement $\hbar\omega_x = 3.137$ meV, $\hbar\omega_y = 6.274$ meV; dielectric constant $\kappa = 12.5$; effective mass $m^* = 0.067 m_e$. The single labels denote the quantum numbers for the total spin. The thin vertical lines indicate the magnetic fields where the ground state changes character, first from $(1/2, 1/2; 1)$ to $(1/2, 1/2; 2)$ and then from $(1/2, 1/2; 2)$ to $(3/2, 1/2)$. These changes in the intrinsic structure of the ground state are associated with discontinuous jumps in the Von Neumann entropy as a function of the magnetic field.

Neumann entropy $\mathcal{S}_{\mathrm{vN}}$, which is defined as

$$\mathcal{S}_{\mathrm{vN}} = -\mathrm{Tr}(\rho \ln \rho), \tag{45}$$

with $\rho_{\nu\mu} = \langle \Psi^{\mathrm{EXD}} | a_\mu^\dagger a_\nu | \Psi^{\mathrm{EXD}} \rangle$ being the single-particle density.[74, 75]

In Fig. 24, we plot the Von Neumann entropy for the three lowest EXD states with $S_z = 1/2$ as a function of the magnetic field for $N = 3$ electrons in an anisotropic quantum dot with the same parameters as the energy spectra in Fig. 16 (strong anisotropy with anisotropy parameter $\eta = 1/2$). We see that the von Neumann entropy increases for all three states as the magnetic field increases and the electrons become more localized. The thin vertical lines indicate the magnetic fields where the ground state changes character, first from $(1/2, 1/2; 1)$ to $(1/2, 1/2; 2)$ and then from $(1/2, 1/2; 2)$ to $(3/2, 1/2)$ [around $B = 3.5$ T, compare Fig. 16]. These changes in the intrinsic structure of the ground state are associated with discontinuous jumps in the Von Neumann entropy as a function of the magnetic field.

3.6   Summary

We have presented extensive exact-diagonalization calculations for $N = 3$ electrons in anisotropic quantum dots, and for a broad range of anisotropies and strength of inter-electron repulsion. We have analyzed the excitation spectra both as a function of the magnetic field and as a function of increasing anisotropy. A main finding was the appearance of triple-crossing points in the ground-state energy curves for stronger anisotropies.

Analysis of the intrinsic structure of the many-body wave functions through spin-resolved conditional probability distributions revealed that for all examined cases (including those with parameters corresponding to currently fabricated quantum dots) the electrons localize forming Wigner molecules. For certain ranges of dot parameters (mainly at strong anisotropy), the Wigner molecules acquire a linear geometry, and the associated wave functions with a spin projection $S_z = 1/2$ are similar to the socalled W-states that are a prototype of entangled states. For other ranges of parameters (mainly at moderate anisotropy), the Wigner molecules exhibit a more complex structure consisting of two mirror isosceles triangles. This latter structures

can be considered as an embryonic unit of a zig-zag Wigner crystal in quantum wires.

Finally, we demonstrated that the degree of entanglement in three-electron quantum dots can be quantified via the von Neumann entropy, in analogy with studies on two-electron quantum dots.

CHAPTER IV

EXACT DIAGONALIZATION FOR DOUBLE DOTS AT LOW MAGNETIC FIELD

4.1   Two-center-oscillator confining potentials

In the 2D two-center oscillator (TCO), the single-particle levels associated with the confining potential of the artificial molecule are determined by the single-particle hamiltonian

$$H = T + \frac{1}{2}m^*\omega_{xk}^2 x^2 + \frac{1}{2}m^*\omega_{yk}^2 y_k'^2 + V_{neck}(y) + h_k + \frac{g^*\mu_B}{\hbar}\mathbf{B}.\mathbf{s} \qquad (46)$$

where $y_k' = y - y_k$ with $k = 1$ for $y < 0$ (left) and $k = 2$ for $y > 0$ (right), and the $h_k's$ control the relative well-depth, thus allowing studies of hetero-QDMs. x denotes the coordinate perpendicular to the interdot axis(y). $T = (\mathbf{p} - e\mathbf{A}/c)^2/2m^*$, with $\mathbf{A} = 0.5(-By, Bx, 0)$, and the last term in Eq.(1) is the Zeeman interaction with g^* being the effective g factor, μ_B the Bohr magneton, and $\mathbf{s}$ the spin of an indivisual electron. Here we limit ourselves to systems with $\hbar\omega_{x1} = \hbar\omega_{x2} = \hbar\omega_x$. The most general shapes described by H are two semiellipses connected by a smooth neck$[V_{neck}(y)]$.$y_1 < 0$ and $y_2 > 0$ are teh centers of these semiellipses, $d = y_2 - y_1$ is the interdot distance, and m^* is the effective electron mass. For the smooth neck, we use

$$V_{neck}(y) = \frac{1}{2}m^*\omega_{yk}^2 \left[c_k y_k'^3 + d_k y_k'^4\right]\theta(|y| - |y_k|) \qquad (47)$$

Where $\theta(u) = 0$ for $u > 0$ and $\theta(u) = 1$ for $u < 0$. The four constants c_k and d_k cna expresssed via two parameters, as follows: $(-1)^k c_k = (2 - 4\epsilon_k^b)/y_k$ and $d_k = (1 - 3\epsilon_k^b)/y_k^2$, where the barrier-control parameters $\epsilon_k^b = (V_b - h_k)/V_{0k}$ are related to the actual(controlable) height of the bare barrier(V_b) between the two QDs, and

$V_{0k} = m^* \omega_{yk}^2 y_k^2 / 2 \text{(for } h_1 = h_2, \ V_{01} = V_{02} = V_0\text{)}.$

The single-particle levels of H, including an external perpendicular magnetic field B, are obtained by numerical diagonalization in a (variable-with-seperation) basis consisting of the eigenstates of the auxilliary hamilton:

$$H_0 = \frac{p^2}{2m^*} + \frac{1}{2}m^* \omega_x^2 x^2 + \frac{1}{2}m^* \omega_{yk}^2 y_k'^2 + h_k. \tag{48}$$

This eigenvalue problem is seperable in x and y; i.e.,the wave functions are written as $\Phi_{m\nu}(xy) = X_m(x)Y_\nu(y)$. The solutions for $X_m(x)$ are those of one-dimensional oscillator, and for $Y_\nu(y)$ they can be expressed through the parabolic cylinder functions $U[\alpha_k, (-1)^k \xi]$, where $\xi_k = y_k'\sqrt{2m^* w_{yk}/\hbar}$, $\alpha_k = (-E_y + h_k)/(\hbar\omega_{yk})$, and $E_y = (\nu + 0.5)\hbar\omega_{y1} + h_1$ denote the y-eigenvalues. The matching conditions at $y = 0$ for the left and right domains yield the y-eigenvalues and eigenfunctions $Y_\nu(y)$(m is integer and ν is in general real).

4.2 Structures for three-electron double dots at low magnetic field

In this section, we carry out exact diagonalization (EXD) studies for a three-electron double quantum dot under low and moderate magnetic fields. For the confining potential, please see the previous section. Below, we present the density and CPD figures for double quantum dots that contain three electrons at $B = 0$ and $B = 4\ T$. We use the same code as for the elliptical dots apart from different input files.

In all instances here, we use a moderate Coulomb repulsion ($\kappa = 12.5$). From Fig. 25, we see that the electrons form a dimer with the electrons distributed over the centers of the two dots. The first two electrons localize at the centers of the dots, the third electron will have a 50% probability to appear at each center. If we increase the magnetic field to $B = 4\ T$, the same localization effect appears, but it's more intense, see Fig. 26. In order to understand the spin configuration, we need to calculate CPDs to explore all the spin cases. We have fixed the spin projection along the magnetic
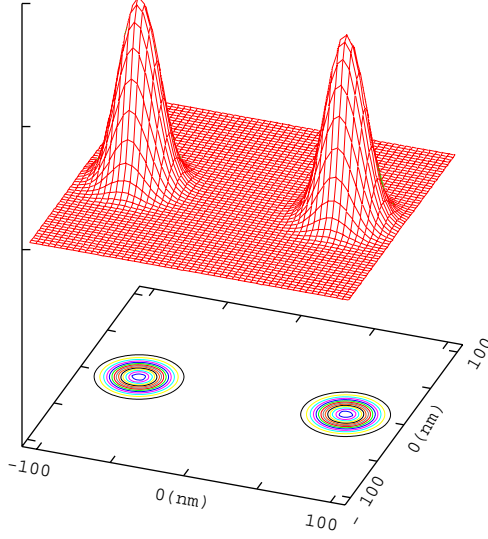
Figure 25: Charge density for the ground state (with $S_z = 1/2$) of a double dot with 3 electrons. The distance between the two dots is 70 nm; $\hbar\omega_x = \hbar\omega_y = 5 \; meV$; $\kappa = 12.5$; $B = 0$;

field direction with $S_z = 1/2$.

In Fig. 27, we fix the observation electron with spin up at the center of the right dot and find the conditional probability for the other spin up electron. We find that the remaining spin up electron is localized on the left dot. Futhermore in Fig. 28, we fix the observation electron with spin up at the center of the right dot and find the conditional probability for the spin down electron. We find that the spin down electron has equal probabilities to be on both dots. In Fig. 29, we fix the observation electron with spin down at the center of the right dots and find the conditional probability of spin up electrons. We find that the spin up electrons have different probabilities in the two centers of the dots. These three figures show that there are two localized electrons with spin up and one delocalized electron with spin down.
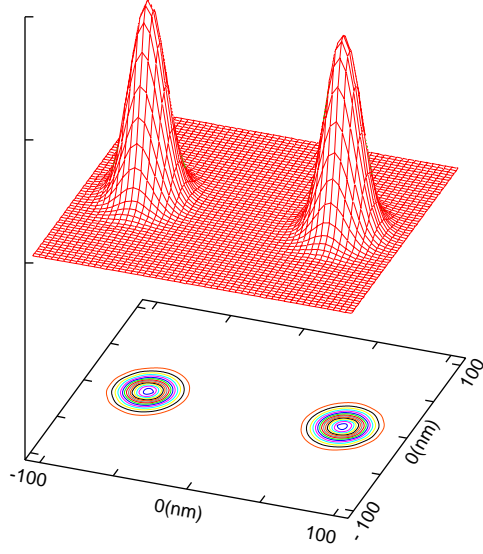
Figure 26: Charge density for the first excited state (with $S_z = 1/2$) of a double dot with 3 electrons. The distance between the two dots is 70 nm; $\hbar\omega_x = \hbar\omega_y = 5\ meV$; $\kappa = 12.5$; $B = 4\ T$;
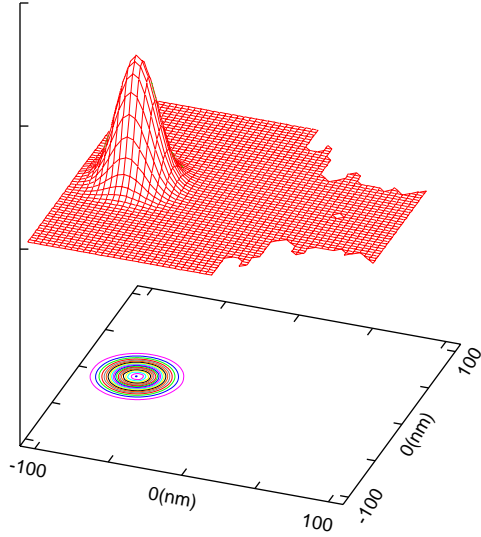
Figure 27: CPD for the ground state (with $S_z = 1/2$) of a double dot with 3 electrons. The distance between the two dots is 70 nm; $\hbar\omega_x = \hbar\omega_y = 5\ meV$; $\kappa = 12.5$; $B = 0$. The observation point is in 70nm (center of right dot) with spin up electron, and we look for the probability for the other spin up electron.
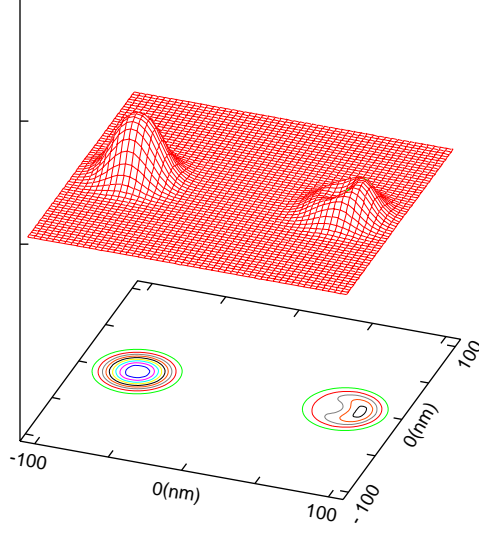
Figure 28: CPD for the ground state (with $S_z = 1/2$) of a double dot with 3 electrons. The distance between the two dots is 70 nm; $\hbar\omega_x = \hbar\omega_y = 5\ meV$; $\kappa = 12.5$; $B = 0$. The observation point is in 70nm (center of right dot) with spin up electron, and we look for the probability for the other spin down electron.
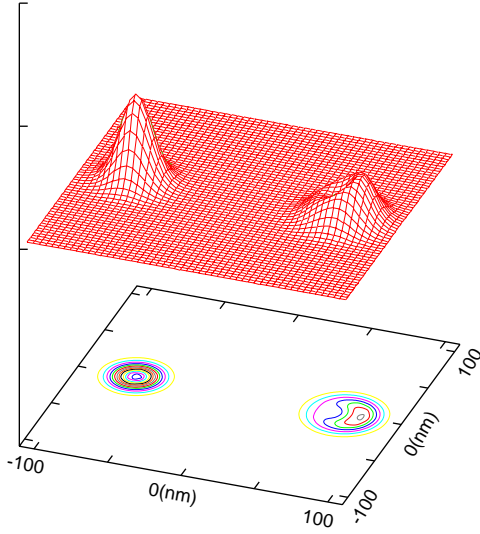
Figure 29: CPD for the ground state (with $S_z = 1/2$) of a double dot with 3 electrons. The distance between the two dots is 70 nm; $\hbar\omega_x = \hbar\omega_y = 5\ meV$; $\kappa = 12.5$; $B = 0$. The observation point is in 70nm (center of right dot) with spin down electron, and we look for the probability for the other spin up electrons.
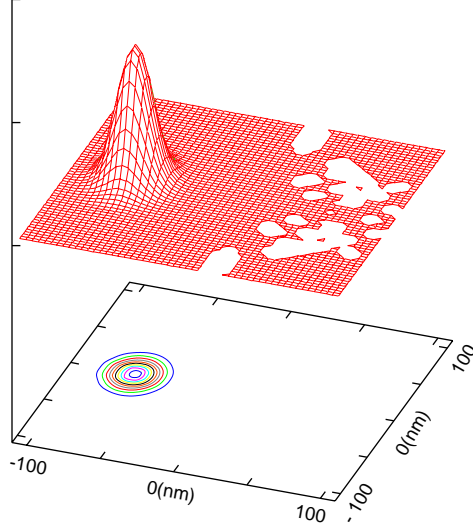
Figure 30: CPD for the first excited state (with $S_z = 1/2$) of a double dot with 3 electrons. The distance between the two dots is 70 nm; $\hbar\omega_x = \hbar\omega_y = 5\ meV$; $\kappa = 12.5$; $B = 4\ T$. The observation point is in 70nm (center of right dot) with spin up electron, and we look for the probability for the other spin up electron.

If we increase the magnetic field to $B = 4\ T$, the same spin configuration ($S_z = 1/2$) becomes the first excited state. In Fig. 30, we fix the observation electron with spin up at the center of the right dot and find the conditional probability of the other spin up electron. We find that the spin up electron is localized at the center of the left dot. Futhermore in Fig. 31, we fix the observation electron with spin up at the center of the right dot and find the conditional probability of the other spin down electron. We find that the spin down electron has equal probabilities to be on both dots. In Fig. 32, we fix the observation electron with spin down at center of the right dot and find the conditional probabilities of the spin up electrons. We find that the spin up electrons have equal probabilities to be on both dots. These three figures show that there are two localized electrons with spin up and one delocalized electron with spin down.
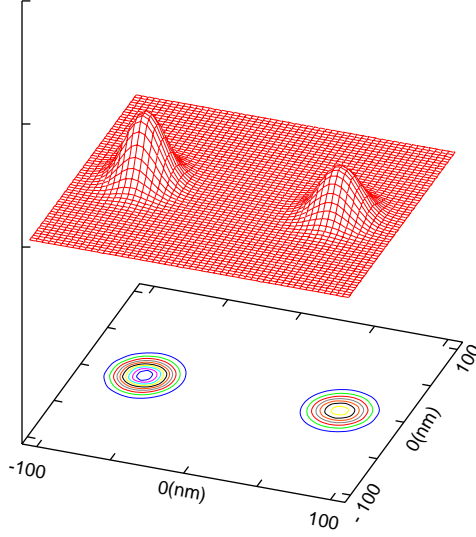
Figure 31: CPD for the first excited state (with $S_z = 1/2$) of a double dot with 3 electrons. The distance between the two dots is 70 nm; $\hbar\omega_x = \hbar\omega_y = 5 \ meV$; $\kappa = 12.5$; $B = 4 \ T$. The observation point is in 70nm (center of right dot) with spin up electron, and we look for the probability for the other spin down electron.
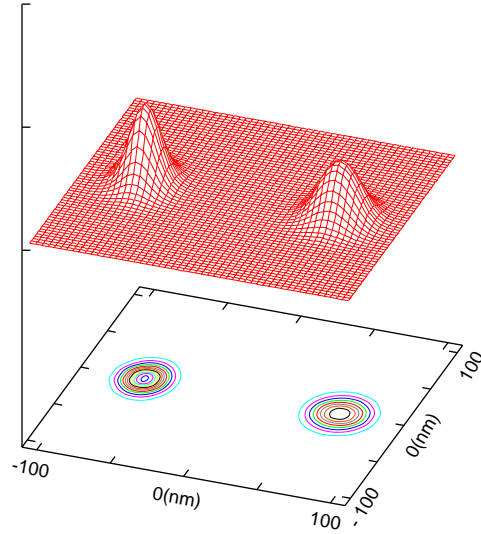
Figure 32: CPD for the first excited state (with $S_z = 1/2$) of a double dot with 3 electrons. The distance between the two dots is 70 nm; $\hbar\omega_x = \hbar\omega_y = 5 \ meV$; $\kappa = 12.5$; $B = 4 \ T$. The observation point is in 70nm (center of right dot) with spin down electron, and we look for the probability for the other spin up electrons.

CHAPTER V

EXACT DIAGONALIZATION IN THE LOWEST

LANDAU LEVEL

5.1   Introduction

Two-dimensional N electrons (up to 11) quantum dots under strong magnetic field
have been studied extensively. These methods include exact-diagnolization (EXD),
Rotating Electron Molecule (REM) and composit fermion model (CF). As EXD cal-
culates the ground and excited states numerically, it provide rich information about
formation of Wigner Molecules under strong magnetic field, where the wavefuntion
basis is restricted to the Lowest Landau level. The direct numerical diagonialza-
tion has been conducted by Maksym and Charkraborty for $N = 3, 4$ and Yang for
$N = 5, 6$.

In this chapter, using EXD, we study the properties of $N = 9$ electrons under
strong magnetic field to demonstrate the formation of Wigner Molecules. We have
used the basis of Fock-Darwin and the representation of Coulomb Matrix element of
Tsiper in the Lowest Landau Level(LLL). We also show the results obtained with
Lauglin's method. Our EXD results clearly show that the electrons under parabolic
confinement will form Wigner Molecules instead of liquid states.

5.2   Laughlin's theory

Laughlin has proposed a wavefunction to explain the Fractional Quantum Hall Effect
(FQHE) in 1983 for the ground state of $v = 1/3$. Single particle states in the Lowest
Landau level are given by

$$\eta_l(z) = (2\pi 2^l l!)^{-1/2} z^l e^{-\frac{1}{4}|z|^2}, \tag{49}$$

where $z = x - iy$ and l is the angular momentum. A LLL function for many electrons can, but not necceary, have the form

$$\psi = F_A \left[z_j \right] exp \left[-\frac{1}{4} \sum_i |z_j|^2 \right] \tag{50}$$

where $F_A \left[z_j \right]$ is a polynomial of z's antisymmetric under exchange of two coordinates. And the spin part of the wavefunction is symmetric under the exchange of electrons. Laughlin has determined the form for the polynomial under the following assumptions:

1. Following Jastow's variational wavefunction for superfluid helium, which has same pairwise correlations, he assume the polynomial part has the form of

$$F_A \left[z_j \right] = \prod_{j<k} f(z_j - z_k), \tag{51}$$

2. In order for the wavefuction to be an eigenstate of the total angular momentum, which commutes with the Coulomb interaction, the product $\prod_{j<k} f(z_j - z_k)$ must be a polynomial of $z_1, z_2, \ldots, z_N$ of degree of L, that the replacement $z_j \rightarrow z_i e^{-i\theta}$ is equivalent to multiplication by $e^{-iL\theta}$. This is possible only if $f(z_j - z_k)$ itself has a definite angular momentum.

3. f should be antisymmetric under the exchange of electrons. The only form that satisfies the above requirements and has an analytic expression

$$f(z) = z^m \tag{52}$$

where m is an odd interger and the corresponding filling factor v is expressed as $v = 1/m$.

The above three assumptions produces Laughlin's wavefunction

$$\psi_{1/m} = \prod_{j<k} (z_j - z_k)^m exp \left[-\frac{1}{4} \sum_i |z_j|^2 \right] \tag{53}$$

The wavefunction has explained the experiment well for specific filling factor $v = 1/3$.

5.3 REM analytic trial wave functions in LLL

The approach used in Ref. [16] for constructing the REM functions in high B consists of two-steps: First the breaking of the rotational symmetry at the level of the single-determinantal unrestricted Hartree-Fock approximation yields states representing electron molecules (or finite crystallites, also referred to as Wigner molecules, see Ref. [18] and Ref. [76]). Subsequently the rotation of the electron molecule is described through restoration of the circular symmetry via post Hartree-Fock methods, and in particular Projection Techniques. [77] Naturally, the restoration of symmetry goes beyond the single determinantal mean-field description and yields multi-determinantal wave functions. For QD's, we have shown that the method of symmetry restoration is applicable to both the zero [18, 78] and high[16] magnetic-field cases.

In the zero and low-field cases, the broken symmetry UHF orbitals need to be determined numerically, and, in addition, the restoration of the total-spin symmetry needs to be considered for unpolarized and partially polarized cases. The formalism and mathematical details of this procedure at $B = 0$ have been elaborated in Ref. [18] (see also Ref. [79] and Ref. [80] for the restoration of the total spin in the case of quantum dot molecules).

In the case of high magnetic fields, one can specifically consider the limit when the static electric confining potential can be neglected compared to the confinement induced by the magnetic field. Then, assuming a symmetric gauge, the UHF orbitals can be represented [16, 81] by displaced Gaussian functions, centered at different positions $Z_j \equiv X_j + \imath Y_j$ according to the equilibrium configuration of N classical point charges[82, 83] arranged at the vertices of nested regular polygons (each Gaussian representing a localized electron). Such displaced Gaussians are

written as (here and in the following $\iota \equiv \sqrt{-1}$)

$$u(z \quad , \quad Z_j) = (1/\sqrt{\pi})$$
$$\times \quad \exp[-|z - Z_j|^2/2] \exp[-\iota(xY_j - yX_j)], \tag{54}$$

where the phase factor is due to the gauge invariance. $z \equiv x + \iota y$ (see Ref. [84]), and all lengths are in dimensionless units of $l_B\sqrt{2}$ with the magnetic length being $l_B = \sqrt{\hbar c/eB}$.

In Ref. [16], we used these analytical orbitals to first construct the broken symmetry UHF determinant, Ψ_N^{UHF}, and then proceeded to derive analytical expressions for the many-body REM wave functions by applying onto Ψ_N^{UHF} an appropriate projection operator[16] $\mathcal{O}_L$ that restores the circular symmetry and generates *correlated*[85] wave functions with a total angular momentum L. These REM wave functions can be easily written down[16] in second-quantization form for any classical polygonal ring arrangement $(n_1, n_2, ...)$ by following certain simple rules for determining the coefficients of the determinants $D(l_1, l_2, ..., l_N) \equiv \det[z_1^{l_1}, z_2^{l_2}, \cdots, z_N^{l_N}]$, where the l_j's denote the angular momenta of the individual electrons. Since we will focus here on the case of $N = 6$ and $N = 3$ electrons, we list for completeness the REM functions associated with the $(0, N)$ and $(1, N-1)$ ring arrangements, respectively [here $(0, N)$ denotes a regular polygon with N vertices, such as an equilateral triangle or a regular hexagon, and $(1, N-1)$ is a regular polygon with $N-1$ vertices and one occupied site in its center],

$$
\begin{aligned}
\Phi_L(0, N) \quad &= \sum_{\substack{0 \leq l_1 < l_2 < \cdots < l_N}}^{l_1 + \cdots + l_N = L} \left(\prod_{i=1}^{N} l_i! \right)^{-1} \\
&\times \left(\prod_{1 \leq i < j \leq N} \sin\left[\frac{\pi}{N}(l_i - l_j) \right] \right) \\
&\times D(l_1, l_2, ..., l_N) \exp(-\sum_{i=1}^{N} z_i z_i^* / 2),
\end{aligned}
\tag{55}
$$

with

$$L = L_0 + Nm, \quad m = 0, 1, 2, 3, ..., \tag{56}$$

and

$$\Phi_L(1, \quad N \quad -1) = \sum_{\substack{1 \leq l_2 < l_3 < \cdots < l_N}}^{l_2 + \cdots + l_N = L} \left(\prod_{i=2}^{N} l_i! \right)^{-1}$$

$$\times \left(\prod_{2 \leq i < j \leq N} \sin \left[\frac{\pi}{N-1}(l_i - l_j) \right] \right)$$

$$\times D(0, l_2, ..., l_N) \exp\left(- \sum_{i=1}^{N} z_i z_i^* / 2\right), \tag{57}$$

with

$$L = L_0 + (N-1)m, \quad m = 0, 1, 2, 3, ..., \tag{58}$$

where $L_0 = N(N-1)/2$ is the minimum allowed total angular momentum for N (polarized) electrons in high magnetic fields. Notice that the REM wave functions [Eq. (55) and Eq, (57)] vanish identically for values of the total angular momenta outside the specific values given by Eq. (56) and Eq. (58), respectively. Generalizations of expression (55) to structures with a larger number r of rings involve, for each additional qth ring $(2 < q \leq r)$,(I) the inclusion of an additional product of sines with arguments containing n_q, and (II) a restriction on the summation of the associated n_q angular momenta.

5.4 Filling factor $\nu = 1/3$

For the fractional quantum hall effect (FQHE) in 2D parabolic quantum dots, Jain used the CF method to calculate states which show liquid-like character under strong magnetic fields. But with the EXD method, we find instead the formation of Wigner Molecules results for $3 \leq N \leq 11$ electrons. First, we show the CPD for Laughlin's wave functions which correspond to liquid-like states. We present EXD results for 9 electrons under a strong magnetic field with a total magic number

$L = 108$, where L is total angular momentum. The electrons organize in two concentric rings: an inner ring contains 2 electrons and an outer ring contains the remaining 7 electrons. The CPD with the observation point located on the inner ring is shown in Figure 33; it shows that the other electron in the inner ring is in a liquid state instead of forming Wigner molecule. The CPD with the observation point located on the outer ring is shown in Figure 34, the remaning electrons in the outer ring show very weak humps.
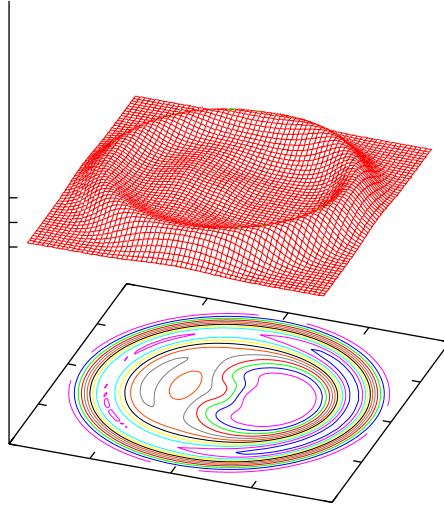
Figure 33: Laughlin's method; CPD for 9 electrons; $L = 108$ ($\nu = 1/3$). When the observation point is on the inner ring, the outer ring will be circular, but the inner ring is in a liquid state.

We see from the above figures that the electrons are not well localized on the same ring.

Now, we show the CPDs for EXD with the same magic number $L = 108$ under strong magnetic field. The CPD with the observation point located on the inner ring is shown in Fig. 35. The CPD with the observation point located on the outer ring is shown in Fig. 36.

These figures show that the EXD wave functions exhibit a stronger electron localization compared to the Laughlin case above. In particular, Fig. 36 displays 6 visible humps corresponding to a (2,7) Wigner molecule configuration.
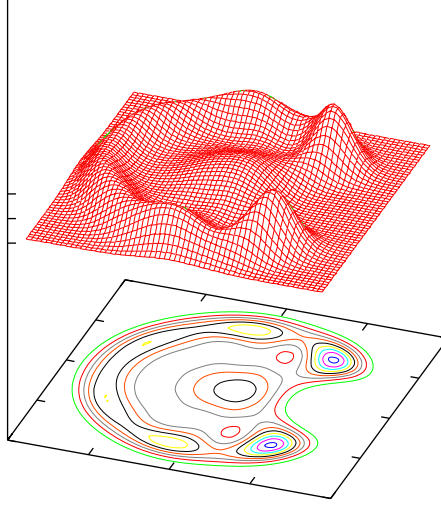
Figure 34: Laughlin's method; CPD for 9 electrons; $L = 108$ ($\nu = 1/3$). When the observation point is on the outer ring, the inner ring is circular, but the outer ring is in a liquid state.

5.5 *Filling factor* $\nu < 1/3$

For higher magic angular momenta, the formation of a Wigner molecule is stronger. We show the formation of WM for $N = 9$ electrons under magic numbers $L = 136$ and $L = 180$ in Figures 37, 38, 39, 40.

When we fix the observation point on the inner ring, another electron on the inner ring forms a two-electron Wigner molecule, which is clearly shown in Fig. 37. The outer ring is in a uniform density, which means that the two rings rotate independently of each other; this confirm our previous assumptions in the REM calculations. When we fix the observation point on the outer ring, six electrons on the outer ring form a Wigner molecule, which means six humps on the outer ring that are clearly visible in Fig. 38. Then the inner ring is in a uniform density since the rings rotate independently.
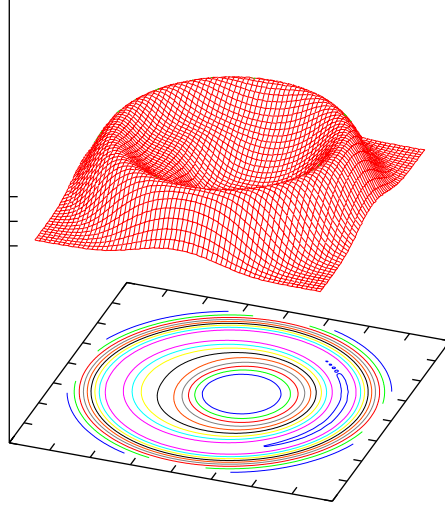
Figure 35: EXD method; CPD for 9 electrons; $L = 108$ ($\nu = 1/3$). The observation point is on the inner ring. The outer ring is circular.
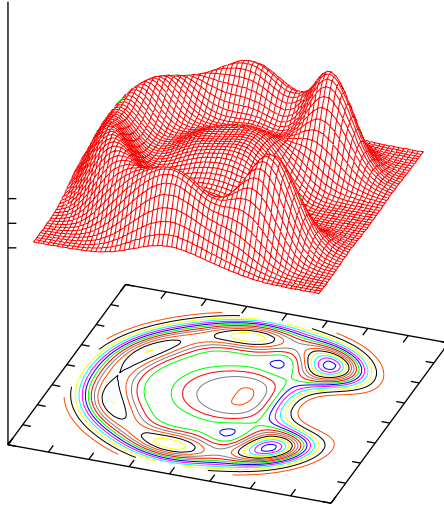
Figure 36: EXD method; CPD for 9 electrons; $L = 108$ ($\nu = 1/3$). The observation point is on the outer ring (visible humps; contrast with the Laughlin state in Fig. 34). The inner ring is circular.
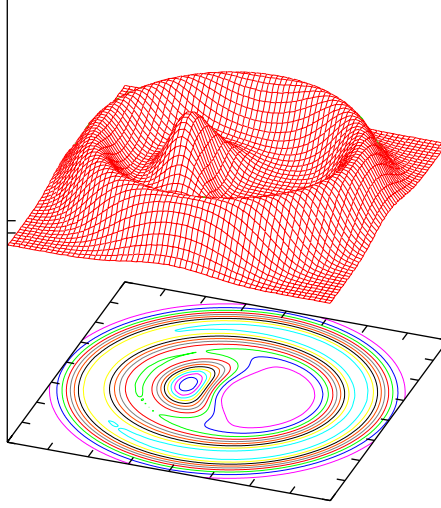
Figure 37: EXD method; CPD for 9 electrons; $L = 136$. The observation point is on the inner ring. The outer ring is circular, and the inner ring is in a Wigner molecule state, exhibiting one well-defined hump.
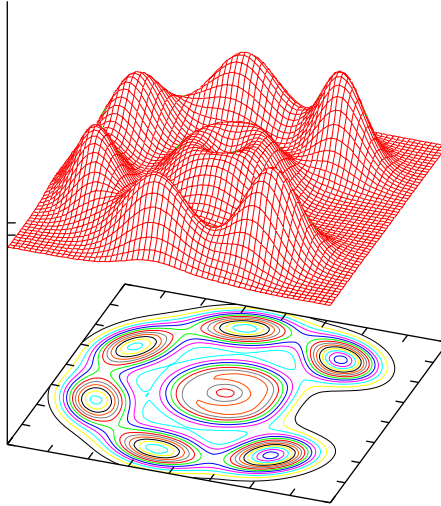
Figure 38: EXD method; CPD for 9 electrons; $L = 136$. The observation point is on the outer ring. The inner ring is circular, and the outer ring is in a Wigner molecule state, exhibiting 6 well defined humps.
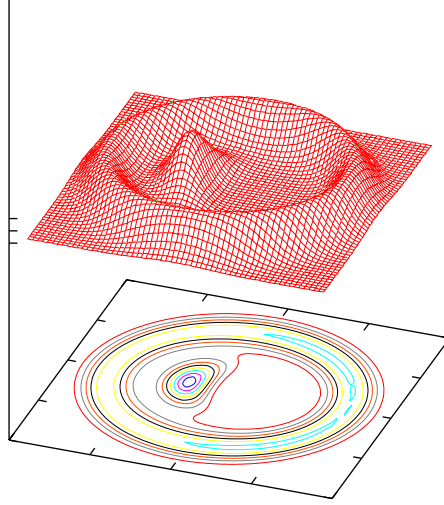
Figure 39: EXD method; CPD for 9 electrons; $L = 180$ ($\nu = 1/5$). The observation point is on the inner ring. The outer ring is circular, and the inner ring is in a Wigner molecule state.

The formation of Wigner molecule is more pronounced when we further increase the total magic angular momentum to $L = 180$ ($\nu = 1/5$). When we fix the observation point on the inner ring, the other electron in the inner ring forms a Wigner molecule, which is clearly shown in Fig. 39. The outer ring is in a uniform density, which means that the two ring rotate independently and confirm our previous assumptions in the REM calculations. When we fix the observation point on the outer ring, six electrons on the outer ring form a Wigner molecule, which means six humps on the outer ring are clearly seen in Fig. 40. Then the inner ring is in a uniform density since the rings rotate independently.

All the above examined cases for $N = 9$ electrons support the conclusion that Wigner molecules form in parabolic quantum dots in the LLL. The formation of Wigner molecules becomes more prominent with increasing magic angular momentum (decreasing filling factor ν).
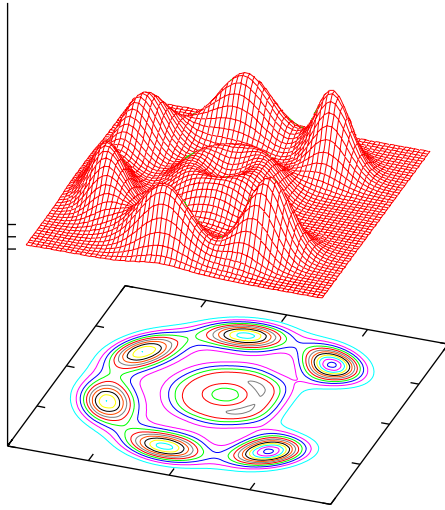
Figure 40: EXD method; CPD for 9 electrons; $L = 180$ ($\nu = 1/5$). The observation point is on the outer ring. The inner ring is circular, and the outer ring is in a Wigner molecule state, with 6 well defined electron humps.

CHAPTER VI

CONCLUSION

The focus of the first part of this thesis pertains to the development of methods that permit investigations of the energetic, structural, and excitation properties of quantum dots in strong magnetic fields with an (essentially) arbitrary number of electrons. Toward this aim, we utilized several computational methods, and have assessed their adequacy. The methods that we have used are: (1) Exact diagonalization which is limited to a rather small number of particles; (2) The "two-step" successive-hierarchical-approximations method (see section 2.2.1), in which a UHF step leading to broken-symmetry solutions (static electron molecule) is followed by restoration (via projection techniques) of circularly symmetric states with good angular momenta (rotating electron molecule; REM); (3) An approximation method based on diagonalization of the electron-electron interaction term restricted to the lowest Landau level (LLL). In this method, the total energy includes, in addition to the LLL diagonalization term, a contribution from the harmonic confinement that is linear in the total angular momentum; (4) An analytic expression [see Eq. (25)] whose derivation is based on the REM.

We performed comparative calculations for quantum dots with an increasing number of parabolically confined electrons ($N = 3, 4, 6, 9, 11$, and 17). The ground-state arrangements of the electrons become structurally more complex as the number of electrons in the dot increases. Using the notation $(n_1, n_2, n_3, ...)$ for the number of electrons located on concentric polygonal rings (see section 2.2.1), the ground-state arrangements are: (0,3) for $N = 3$, (0,4) for $N = 4$, (1,5) for $N = 6$, (2,7) for $N = 9$, (3,8) for $N = 11$, and (1,6,10) for $N = 17$.

Analysis of the results of our calculations revealed that, for all sizes studied by us, the two-step REM method provides a highly accurate description of electrons parabolically confined in quantum dots for a whole range of applied magnetic fields, starting from the neighborhood of the so-called maximum density droplet and extending to the $B \to \infty$ limit. In contrast, the LLL-diagonalization approximation was found to be rather inaccurate for weaker magnetic fields, where it grossly overestimates the total energies of the electrons; the accuracy of this latter method improves at higher field strengths.

The ground-state energy of the electrons in a QD oscillates as a function of the applied magnetic field, and the allowed values of the angular momenta are limited to a set of magic angular momentum values, L_m, which are a natural consequence of the geometrical arrangement of the electrons in the rotating electron molecule. Accordingly, the electrons are localized on concentric polygonal rings which rotate independently of each other (as observed from the conditional probability distributions, see section 2.4). Underlying the aforementioned oscillatory behavior is the incompressibility of the many-body states associated with the magic angular momenta. The general expression for L_m is given in Eq. (9), for a given number N and occupancy of the polygonal rings $\{n_q\}$. For the ground-state L_m's, the values of the non-negative integers k_q in Eq. (9) are taken such as to minimize the total kinetic energy of the electrons. Since the moment of inertia of an outer ring is larger than that of an inner ring of smaller radius, the rotational energy of the outer ring will increase more slowly with increasing angular momentum. Therefore, the k_q index in Eq. (9) of an outer ring will very up to relatively large values while the values corresponding to inner rings remain small (see section 2.4). As a consequence, we find through REM calculations with proper treatment of the confining potential that for $N > 6$, with increasing strength of the magnetic field, the maximum density droplet converts into states with no central vortex, in contrast

to earlier conclusions[24, 58, 59] drawn on the basis of approximate calculations restricted to the lowest Landau level. Instead we find that the break-up of the MDD with increasing B proceeds through the gradual detachment of the outer ring associated with the corresponding classical polygonal configuration.

In addition to the ground-state geometric arrangements, we have studied for certain sizes higher-energy structural isomers (see, e.g., the cases of $N = 6$ and $N = 9$ confined electrons in Fig. 2.3). We find that for all cases with $N \geq 7$ multi-ring confined-electron structures $(n_1, n_2, ..., n_r)$, with $n_1, n_2, ..., n_r \neq 0$ and $r \geq 2$, are energetically favored. For $N = 6$, a (1,5) structure is favored except for a small B-range (e.g., 6.1 T $< B <$ 7.7 T for the parameters in Fig. 2.3), where the (0,6) single-ring structure is favored. For $N \leq 5$ the $(0, N)$ single-ring structure is favored for all B values.

In the REM calculations, we have utilized an analytic many-body wave function [Eq. (8)] which allowed us to carry out computations for a sufficiently large number of electrons ($N = 17$ electrons having a nontrivial three-ring polygonal structure), leading to the derivation and validation of an analytic expression Eq. (25) for the total energy of rotating electron crystallites of arbitrary N.

The non-rigidity implied by the aforementioned independent rotations of the individual concentric polygonal rings motivated us to quantify (see section 2.6) the degree of non-rigidity of the rotating electron molecules at high B, in analogy with the concept of non-classical rotational inertia used in the analysis[40, 42] of supersolid ^{4}He. These findings for finite dots suggest a strong quantal nature for the extended Wigner crystal in the lowest Landau level, designating it as a useful paradigm for exotic quantum solids.

In the second part of this thesis , we present extensive exact-diagonalization calculations for $N = 3$ electrons in anisotropic quantum dots, and for a broad range of anisotropies and strength of inter-electron repulsion. We have analyzed the

excitation spectra both as a function of the magnetic field and as a function of increasing anisotropy. A main finding was the appearance of triple-crossing points in the ground-state energy curves for stronger anisotropies.

Analysis of the intrinsic structure of the many-body wave functions through spin-resolved conditional probability distributions reveals that for all examined cases (including those with parameters corresponding to currently fabricated quantum dots) the electrons localize forming Wigner molecules. For certain ranges of dot parameters (mainly at strong anisotropy), the Wigner molecules acquire a linear geometry, and the associated wave functions with a spin projection $S_z = 1/2$ are similar to the so called W-states that are a prototype of entangled states. For other ranges of parameters (mainly at moderate anisotropy), the Wigner molecules exhibit a more complex structure consisting of two mirror isosceles triangles. This latter structures can be considered as an embryonic unit of a zig-zag Wigner crystal in quantum wires.

Also, we demonstrate that the degree of entanglement in three-electron quantum dots can be quantified via the von Neumann entropy, in analogy with studies on two-electron quantum dots.

Furthermore, we examined the internal structure by EXD wave function of two separated circular dots, at a distance 70nm, that contain three electrons. Through the spin-resolved CPD, we find that the electrons are localized at the centers of the dots. The first two electrons localize at the centers of the dots, while the third electron will have 50% probability to appear at each center.

Finally, we compare the results of Laughlin's method with EXD results for circular dots that contains 9 electrons. While Laughlin's method states that the electrons are in a liquid state, EXD clearly shows that the electrons form Winger Molecules in the LLL, which confirms our previous results obtained with the REM method.

92

APPENDIX A

FORMULA DERIVATION

A.1 Proof that $u(z, Z)$ [Eq. (7)] lies in the LLL when $\lambda = l_B\sqrt{2}$

Using the identity $-i(xY - yX) = (zZ^* - z^*Z)/2$, one finds

$$u(z, Z; \lambda = l_B\sqrt{2}) =$$
$$\frac{e^{\frac{-zz^* - ZZ^* + 2zZ^*}{4l_B^2}}}{\sqrt{2\pi}l_B} = \frac{e^{\frac{-zz^* - ZZ^*}{4l_B^2}}}{\sqrt{2\pi}l_B} \sum_{l=0}^{\infty} \frac{1}{l!} \left(\frac{zZ^*}{2l_B^2}\right)^l =$$
$$\sum_{l=0}^{\infty} C_l(Z^*)\psi_l(z), \tag{59}$$

where $z = x + iy$, $Z = X + iY$, and

$$C_l(Z^*) = \frac{1}{\sqrt{l!}} \left(\frac{Z^*}{l_B\sqrt{2}}\right)^l e^{\frac{-ZZ^*}{4l_B^2}}, \tag{60}$$

with

$$\psi_l(z) = \frac{1}{\sqrt{2\pi l!}l_B} \left(\frac{z}{l_B\sqrt{2}}\right)^l e^{\frac{-zz^*}{4l_B^2}} \tag{61}$$

being the Darwin-Fock single-particle wave functions with zero nodes forming the LLL.

A.2 Coulomb matrix elements between displaced Gaussians [Eq. (7)]

We give here the analytic expression for the Coulomb matrix elements,

$$V_{ijkl} = \int\int d\mathbf{r}_1 d\mathbf{r}_2 u_i^*(\mathbf{r}_1)u_j^*(\mathbf{r}_2)\frac{e^2}{\kappa|\mathbf{r}_1 - \mathbf{r}_2|}u_k(\mathbf{r}_1)u_l(\mathbf{r}_2), \tag{62}$$

between displaced Gaussians [see Eq. (7)] centered at four arbitrary points Z_i, Z_j, Z_k, and Z_l.

One has

$$V_{ijkl} = \frac{e^2}{\kappa\lambda}\sqrt{\frac{\pi}{2}}e^{\vartheta}e^{-\varpi}I_0(\varpi), \tag{63}$$

with

$$\vartheta = -\frac{Z_iZ_i^* + Z_jZ_j^* + Z_kZ_k^* + Z_lZ_l^*}{2\lambda^2} + \zeta\eta + \sigma\tau, \tag{64}$$

and

$$\varpi = (\zeta - \sigma)(\eta - \tau)/4, \tag{65}$$

where

$$\zeta = \frac{Z_k + Z_i}{2\lambda} + \beta\frac{Z_k - Z_i}{2\lambda} \tag{66}$$

$$\eta = \frac{Z_i^* + Z_k^*}{2\lambda} + \beta\frac{Z_i^* - Z_k^*}{2\lambda} \tag{67}$$

$$\sigma = \frac{Z_l + Z_j}{2\lambda} + \beta\frac{Z_l - Z_j}{2\lambda} \tag{68}$$

$$\tau = \frac{Z_j^* + Z_l^*}{2\lambda} + \beta\frac{Z_j^* - Z_l^*}{2\lambda}. \tag{69}$$

The magnetic-field dependence is expressed through the parameter

$$\beta = \frac{\lambda^2}{2l_B^2}. \tag{70}$$

The length parameters λ and l_B (magnetic length) are defined in the text following Eq. (7). Note that $\beta = 0$ for $B = 0$ and $\beta = 1$ for $B \to \infty$. The latter offers an alternative way for calculating REM energies and wave functions in the lowest Landau level without using the *analytic* REM wave functions presented in Ref. [16].

A.3   Fock-Darwin Levels

In this appendix, we follow closely the presentation in the book of *Introduction to condensed matter physics* by F. Duan and J. Guojun [86]. For 2D parabolic Quantum Dots with lateral confinement, $V(x,y)$,the confinement potential can be written as

$$V(\mathbf{r}) = V_0 + \frac{1}{2}m^*\omega_0^2r^2, \tag{71}$$

94

where $\mathbf{r} = (x, y)$ is the position vector, m^* is the effective mass, and $\hbar\omega_0$ is the confinement potential. And if there is a pendicular magnetic field to the 2D quantum dots, then the Hamiltonian is

$$H = \frac{1}{2m^*}(\mathbf{p} - \frac{e}{c}\mathbf{A})^2 + \frac{1}{2}m^*\omega_0^2 r^2 = \frac{p^2}{2m^*} + \frac{1}{2}m^*(\omega_0^2 + \frac{1}{4}\omega_c^2)r^2 - \frac{1}{2}\omega_c l_z, \qquad (72)$$

where $\mathbf{p}$ is the momentum, $l_z = xp_y - yp_x$ is the projection of angular momentum on the z direction, which is also the direction of external magnetic field $\mathbf{B}$; $\mathbf{A}$ is the vector potential of $\mathbf{B}$ and defined here as $(By, -Bx, 0)/2$. And $\omega_c = e\mathbf{B}/m^*$ is the cyclotron frequency. To get the Fock-Dawin levels, new parameters are defined:

$$z = x + iy, \quad z^* = x - iy, \qquad (73)$$

The effective length is

$$l_0 = \frac{l_B}{(1 + 4\omega_0^2/\omega_c^2)^{\frac{1}{4}}} \qquad (74)$$

The partial differential operator is

$$\partial_z = \frac{1}{2}(\partial_x - i\partial_y), \quad \partial_z^* = \frac{1}{2}(\partial_x + i\partial_y), \qquad (75)$$

where $l_B = (\hbar c/eB)^{1/2}$ is the magnetic length in the absence of a confining potential. According to the new parameters, the Hamiltonian in (71) is the summation of two Harmonic oscillators with the frequencies

$$\omega_\pm = (\omega_0^2 + \frac{1}{4}\omega_c^2) \pm \frac{1}{2}\omega_c, \qquad (76)$$

and the eigenstates and eigenfunctions are

$$\psi_{n_+ n_-}(z, z^*) = \frac{1}{\sqrt{2\pi}}\exp(\frac{zz^*}{4l_0})\frac{(\partial_z)^{n_+}(\partial_z^*)^{n_+}}{(n_+! n_-!)^{1/2}}\exp(-\frac{zz^*}{2l_0^2}). \qquad (77)$$

and

$$E(n_+ n_-) = \hbar\omega_+(\frac{1}{2} + n_+) + \hbar\omega_-(\frac{1}{2} + n_-), \qquad (78)$$

which are called Fock-Dawin levels. When $B = 0$, these levels are degenerate, $\omega_+ = \omega_- = \omega_0$. And at strong magnetic field, the Landau level is in steps of $\hbar\omega_c$.

For parabolic confinment, $l_z = xp_y - yp_x = z\partial_z - z^*\partial_z^*$, and $l_z(n_+n_-) = n_+ - n_-$. Also the wavefunction can be written as

$$\psi_{nm}(r,\theta) = \phi_m(\theta)R_{nm}(r), \tag{79}$$

where $\phi_m(\theta) = (2\pi)^{-1/2}e^{im\theta}$ is the eigenfunction of the operator of the angular mementum projection with eigenvalue m. And the radius function is

$$R_{nm}(r) = \frac{\sqrt{2}}{l_0}\left[\frac{n_r}{(n_r+|m|)}\right](\frac{r}{l_0})^{|m|}\exp(-\frac{r^2}{2l_0^2})L_{nr}^{|m|}(\frac{r^2}{l_0}). \tag{80}$$

where $L_{nr}^{|m|}$ is the Laguerre polynomials

$$L_{nr}^{|m|}(u) = \frac{1}{m}u^{-|m|}e^u\frac{d^{n_r}}{du^{n_r}}(u^{n_r+|m|}e^{-u}), \tag{81}$$

where $n = 0, 1, 2, 3\ldots$ is the principle quantum number, and $m = -n, -n+2, \ldots, n-2, n$ is the azimuthal quantum number. $n_r = (n-|m|)/2$ is the radial quantum number, and u is real. Also n_+ and n_- can be expressed by (n, m) as

$$n_- = (n+m)/2, \quad n_+ = (n-m)/2 \tag{82}$$

The corresponding eneries are

$$E(nm) = (n+1)\hbar(\omega_0^2 + \frac{\omega_c^2}{4})^{1/2} - \frac{m\hbar\omega_c}{2}. \tag{83}$$

The Fock-Darwin levels are single-electron approach and have some agreement with experiment. But we need consider the Coulomb interaction when we require more exact results.

APPENDIX B

TECHNICAL PART

B.1 ARPACK

I have used the ARPACK extensively for Eigenvalue problem with real and complex matrix. As for the Exact Diagnolization Calculation of Quantum dots, the space will increase exponentially with the number of electrons and applied magnetic field. The required storage for matrix elements will become every large to dimension of million, though the matrix may become sparse for EXD. So established ARPACK provides a very good library for handle large system. Also as the current parallel ARPACK system is on the early stage and does not fit the need of my application, I have parallized the code by myself to meet specific requirement. The ARPACK uses Implicitly Restarted Arnoldi Method (IRAM), which is very closely related to the Implicitly Shifted QR-Algorithm for dense problems. Now I will give a broad overview of the theory and present some details in the implementation.

In describing ARPACK, I follow closely the documentations in the website of http://www.caam.rice.edu/software/ARPACK/ (accessed on 09/2005).

B.1.1 The Implicitly Restarted Arnoldi Method in ARPACK

Start: Build a length m Arnoldi factorization $\mathbf{AV}_m = \mathbf{V}_m\mathbf{H}_m + \mathbf{f}_m\mathbf{e}_m^T$ with the starting vector $\mathbf{v}_1$.

Iteration: Until convergence

1. Compute the eigenvalues $\{\lambda_j : j = 1, 2, \ldots, m\}$ of m. Sort these eigenvalues according to the user selection criterion into a wanted set $\{\lambda_j : j = 1, 2, \ldots, k\}$ and an unwanted set $\{\lambda_j : j = k + 1, k + 2, \ldots, m\}$.

2. Perform $m - k = p$ steps of the QR iteration with the unwanted eigenvalues $\{\lambda_j : j = k+1, k+2, \ldots, m\}$ as shifts to obtain $\mathbf{H}_m\mathbf{Q}_m = \mathbf{Q}_m\mathbf{H}_m^+$.

3. Restart: Postmultiply the length m Arnoldi factorization with the matrix $\mathbf{Q}_k$ consisting of the leading k columns of $\mathbf{Q}_m$ to obtain the length k Arnoldi factorization $\mathbf{AV}_m\mathbf{Q}_k = \mathbf{V}_m\mathbf{Q}_k\mathbf{H}_k^+ + \mathbf{f}_k^+\mathbf{e}_k^T$, where $\mathbf{H}_k^+$ is the leading principal submatrix of order k for $\mathbf{H}_m^+$. Set $\mathbf{V}_k \leftarrow \mathbf{V}_m\mathbf{Q}_k$.

4. Extend the length k Arnoldi factorization to a length m factorization.

The following discussion begins with a very brief review of the structure of the algebraic eigenvalue problem and some basic numerical methods that either influence or play a direct role in the IRAM. Overcoming the basic disadvantages of the simple power method motivates the introduction of Krylov subspaces along with the important projection idea and the related approximation properties. The Lanczos/Arnoldi factorization is introduced as a concrete way to construct an orthogonal basis for a Krylov subspace and provides a means to implement the projection numerically. Implicit restarting is introduced as an efficient way to overcome the often intractable storage and computational requirements in the original Lanczos/Arnoldi method. This new technique turns out to be a truncated form of the implicitly shifted QR algorithm and hence implementation issues and ultimate behavior are closely tied to that well understood method. Because of its reduced storage and computational requirements, the technique is suitable for large scale eigenvalue problems. Implicit restarting provides a means to approximate a few eigenvalues with user specified properties in space proportional to where k is the number of eigenvalues sought.

B.1.2   Krylov Subspaces and Projection Methods

The methods that underly the ARPACK software are derived from a class of algorithms called Krylov subspace projection methods. These methods take full

advantage of the intricate structure of the sequence of vectors naturally produced by the power method. An examination of the behavior of the sequence of vectors produced by the power method suggests that the successive vectors may contain considerable information along eigenvector directions corresponding to eigenvalues other than the one with largest magnitude. The expansion coefficients of the vectors in the sequence evolve in a very structured way. Therefore, linear combinations of the these vectors can be constructed to enhance convergence to additional eigenvectors. A single vector power iteration simply ignores this additional information, but more sophisticated techniques may be employed to extract it. If one hopes to obtain additional information through various linear combinations of the power sequence, it is natural to formally consider the Krylov subspace and to attempt to formulate the best possible approximations to eigenvectors from this subspace. It is reasonable to construct approximate eigenpairs from this subspace by imposing a Galerkin condition : A vector is called a Ritz vector with corresponding Ritz value if the Galerkin condition is satisfied. For details, please refer to [87].

B.1.3 The Arnoldi Factorization

Definition : If $\mathbf{AV} = \mathbf{VH}$, where V is an orthogonal matrix and H is an upper Hessenberg matrix of order k with positive subdiagonal elements and called a k-step Arnoldi Factorization of $\mathbf{A}$, If $\mathbf{A}$ is Hermitian then is real, symmetric and tridiagonal and the relation is called a k-step Lanczos Factorization of The columns of H are referred to as the Arnoldi vectors or Lanczos vectors, respectively. The preceding development of this factorization has been purely through the consequences of the orthogonal projection imposed by the Galerkin conditions. (A more straightforward but less illuminating derivation is to equate the first k columns of the Hessenberg decomposition)

The purpose here is to investigate the use of this factorization to obtain

approximate eigenvalues and eigenvectors. The discussion of the previous section implies that Ritz pairs satisfying the Galerkin condition are immediately available from the eigenpairs of the small projected matrix.

B.1.4 Restarting the Arnoldi Method

An unfortunate aspect of the Lanczos/Arnoldi process is that one cannot know in advance how many steps will be required before eigenvalues of interest are well approximated by the Ritz values. This is particularly true when the problem has a wide range of eigenvalues but the eigenvalues of interest are clustered. Without a spectral transformation, many Lanczos steps are required to obtain the selected eigenvalues. In order to recover eigenvectors, one is obliged either to store all of the Lanczos basis vectors (usually on a peripheral device) or to re-compute them. Also, very large tridiagonal eigenvalue problems will have to be solved at each step. In the Arnoldi process that is used in the non-Hermitian case, not only do the basis vectors have to be stored, but the cost of the Hessenberg eigenvalue subproblem is at the k-th step. The obvious need to control this cost has motivated the development of restarting schemes. The ARPACK software is based upon another approach to restarting that offers a more efficient and numerically stable formulation. This approach called implicit restarting is a technique for combining the implicitly shifted QR scheme with a k-step Arnoldi or Lanczos factorization to obtain a truncated form of the implicitly shifted QR-iteration. The numerical difficulties and storage problems normally associated with Arnoldi and Lanczos processes are avoided. The algorithm is capable of computing a few (k) eigenvalues with user specified features such as largest real part or largest magnitude using storage. No auxiliary storage is required. The computed Schur basis vectors for the desired k-dimensional eigen-space are numerically orthogonal to working precision. The suitability of this method for the development of mathematical software stems from this concise and

automatic treatment of the primary difficulties with the Arnoldi/Lanczos process. Implicit restarting provides a means to extract interesting information from large Krylov subspaces while avoiding the storage and numerical difficulties associated with the standard approach. It does this by continually compressing the interesting information into a fixed size k-dimensional subspace.

B.1.5 Stopping Criterion

Ritz pair is a good approximation to an eigenpair of **A** if the last component of an eigenvector for is small. If the upper Hessenberg matrix is unreduced (has no zero subdiagonal elements) then standard results imply that However, this quantity can be quite small even if all of the subdiagonal element of are far from zero. Usually, this is how convergence takes place, but it is also possible for to become small. If the quantity is small enough, then all m eigenvalues of are likely to be good approximations to m eigenvalues of In the Hermitian case, this estimate on the residual can be turned into a precise statement about the accuracy of the Ritz value as an approximation to the eigenvalue of A that is nearest to.

B.1.6 Naming Conventions, Precisions and Types

ARPACK has two interface routines that must be invoked by the user. They are aupd that implements the IRAM and eupd to post process the results of aupd. The user may request an orthogonal basis for a selected invariant subspace or eigenvectors corresponding to selected eigenvalues with eupd. If a spectral transformation is used, eupd transforms the computed eigenvalues for the problem. Both aupd and eupd are available for several combinations of problem type (symmetric and non-symmetric), data type (real, complex), and precision (single, double). The first letter (s,d,c,z) denotes precision and data type. The second letter denotes whether the problem is symmetric (s) or non-symmetric (n).

I mainly used the subroutines dnaupd,dneupd,znaupd,zneupd. The descriptions are

the following:

dnaupd Top level reverse communication interface to solve real double precision non-symmetric problems.

dneupd Post processing routine used to compute eigenvectors and/or Schur vectors corresponding to the invariant subspace associated with the computed eigenvalues. This requires output from a converged application of dnaupd.

znaupd Top level reverse communication interface to solve double precision complex arithmetic problems. This routine should be used for both Hermitian and Non-Hermitian problems.

zneupd Post processing routine used to compute eigenvectors and/or Schur vectors corresponding to the invariant subspace associated with the computed eigenvalues in complex arithmetic. This requires output from a converged application of znaupd. Thus dnaupd is the routine to use if the problem is a double precision nonsymmetric (standard or generalized) problem and dneupd is the post-processing routine to use in conjunction with dnaupd to recover eigenvalues and eigenvectors of the original problem upon convergence. For complex matrices, one should use naupd and neupd with the first letter either c or z regardless of whether the problem is Hermitian or non-Hermitian.

B.1.7 Code usage and Parallelization

The following is the code that is part of my Eigenvalue problem.There are several aspects that I have modified. First of all, I parallized it for more large system. Second, I set the dimension directly to nn to suit my specific application.

!// Code for ARPACK
!//allocate matrix instead of static declaration; maximize memory usage
allocate(ax(maxn)) !//maxn is the max dimension that ARPACK can handle

allocate(v(ldv,maxncv)) !//even after MPI

allocate(workd(3*maxn)) !//work matrix

allocate(resid(maxn))

allocate(w(nmax))

allocate(workdr(3*maxn)) !//real part of workd; for MPI purpose

allocate(workdi(3*maxn)) !//imaginary part of workd

!// ARPACK subroutine to find eigenvalue and eigenstates !//The following include
statement and assignments initiate trace output from the
!//internal actions of ARPACK. See debug.doc in the DOCUMENTS directory for
usage.
!//Initially, the most useful information will be a breakdown of time spent in the
!//various stages of computation given by setting mcaupd =1

ndigit = -3;logfil = 6;mcaitr = 0;mcapps = 0;mcaupd = 1;mcaup2 = 0

mceigh = 0;mceupd = 0

!//The following sets dimensions for this problem

!//nx = 10; n= nx*nx !//I change the dimension here, not useful anymore

nx=icount; n=nx !//n refer to the dimension of matrix; not nx*nx

!Specifications for ARPACK usage are set

!1) NEV = 4 asks for 4 eigenvalues to be computed

!2) NCV = 20 sets the length of the Arnoldi factorization

!3) This is a standard problem (indicated by bmat = 'I')

!4) Ask for the NEV eigenvalues of largest magnitude (indicated by which = 'LM')

! See documentation in ZNAUPD for the other options SM, LR, SR, LI, SI.

!Note: NEV and NCV must satisfy the following conditions:

! $NEV \leq MAXNEV; NEV + 2 \leq NCV \leq MAXNCV$

nev=maxnev; ncv = maxncv; bmat ='I';which = 'SR'

if ($n \geq maxn$) then

print *, ' ERROR with NSIMP: N is greater than MAXN'

go to 9000

else if ($nev \geq maxnev$) then

print *, ' ERROR with NSIMP: NEV is greater than MAXNEV'

go to 9000

else if ($ncv \geq maxncv$) then

print *, ' ERROR with NSIMP: NCV is greater than MAXNCV'

go to 9000

end if

!//Specification of stopping rules and initial conditions before calling ZNAUPD

!//TOL determines the stopping criterion.Expect

$|lambdaC - lambdaT| < TOL * |lambdaC|$

!//computed true If TOL .le. 0, then $TOL < -macheps(machineprecision)$

!//is used. IDO is the REVERSE COMMUNICATION parameter used to specify actions

!//be taken on return from ZNAUPD.(see usage below) It MUST initially be set to 0

!//before the first call to ZNAUPD.INFO on entry specifies starting vector information

!//and on return indicates error codes.Initially, setting INFO=0 indicates that a

!//random starting vector is requested to start the ARNOLDI iteration. Setting INFO

!//to a nonzero value on the initial call is used. if you want to specify your own

!//starting vector (This vector must be placed in RESID). The work array WORKL is

!//used in ZNAUPD as workspace. Its dimension LWORKL is set as illustrated below.

lworkl = 3*ncv**2+5*ncv; tol=.0d-8; ido = 0; ifo= 0

!//Specification of Algorithm Mode:This program uses the exact shift strategy

!//(indicated by setting IPARAM(1) = 1).IPARAM(3) specifies the maximum number

!//of Arnoldi iterations allowed. Mode 1 of ZNAUPD is used (IPARAM(7) = 1). All

!//these options can be changed by the user. For details see the documentation in

!//ZNAUPD.

ishfts = 1

maxitr = 25000; !//convergency steps; more enery levels,it should increase;

mode1 = 1; iparam(1) = ishfts; iparam(3) = maxitr; iparam(7) = mode1

!//M A I N L O O P (Reverse Communication Loop)

10 continue

!//Repeatedly call the routine ZNAUPD and take actions indicated by parameter IDO

!//until either convergence is indicated or maxitr has been exceeded.

!//znaupd has floating underflow problem,which I haven't figured out.

call znaupd (ido, bmat, n, which, nev, tol, resid, ncv,v,ldv,iparam,ipntr,&

& workd, workl, lworkl,rworkl,info)

if (ido .eq. -1 .or. ido .eq. 1) then

!//Perform matrix vector multiplication $y \leftarrow Ax$

!//The user should supply his/her own matrix vector multiplication routine here

!//that takes workd(ipntr(1)) as the input vector x , and returns the resulting

!//matrix-vector product $y = Ax$ in the array workd(ipntr(2)).

!//The following parts are parallelized according to the need of my computation

```
call mpiav(icount,workd(1),workd(ipntr(2)),my_rank,total,rankcount)
```

```
if(my_rank==total-1) then
```

istart=ipntr(2)+total*int(icount/total)

j=icount-total*int(icount/total)

do i=0,j-1

workd(istart+i)=workd(ipntr(2)+int(icount/total)+i)

end do

end if

workdr=dble(workd) !//transfer to real and imaginary part for BCAST

workdi=dimag(workd) !//transfer to real and imaginary part for BCAST

```
call mpi_gather(workdr(ipntr(2)),int(icount/total),&
```

```
& mpi_double_precision,&
```

```
& workdr(ipntr(2)),int(icount/total),mpi_double_precision, &
```

```
& 0,mpi_comm_world,mpierr)
```

```
call mpi_gather(workdi(ipntr(2)),int(icount/total), &
```

```
& mpi_double_precision,&
```

```
& workdi(ipntr(2)),int(icount/total),mpi_double_precision, &
```

```
& 0,mpi_comm_world,mpierr)
```

!//processor total-1 may have different number of workd to broadcast

istart=ipntr(2)+total*int(icount/total)

j=icount-total*int(icount/total)

!//broadcast the w(i)s that the rank (total-1) has calculated after the average
allocation

```
call mpi_bcast(workdr(istart),j,mpi_double_precision,&
```

```fortran
 & total-1,mpi_comm_world,mpiierr)
call mpi_bcast(workdi(istart),j,mpi_double_precision,&
 & total-1,mpi_comm_world,mpiierr)
call mpi_bcast(workdr(ipntr(2)),icount,mpi_double_precision,&
 & 0,mpi_comm_world,mpiierr)
call mpi_bcast(workdi(ipntr(2)),icount,mpi_double_precision,&
 & 0,mpi_comm_world,mpiierr)
```

workd=dcmplx(workdr,workdi) !//get back to double complex

!// L O O P B A C K to call ZNAUPD again

go to 10

end if

```fortran
if(my_rank==0) then
```

sumc=0.0d0

do i=1,icount

sumc=sumc+v(i,1)*conjg(v(i,1))

if(i==1) write(213,*)i,v(i,1)

end do

write(213,*)"coefficient:",sumc

end if

!//Either we have convergence or there is an error.

if (info .lt. 0) then

!// Error message, check the documentation in ZNAUPD

print *, ' Error with naupd, info = ', info

print *, ' Check the documentation of naupd'

else

107

!// No fatal errors occurred. Post-Process using ZNEUPD.

!// Computed eigenvalues may be extracted. Eigenvectors may be also computed now if

!// desired. (indicated by rvec = .true.) The routine ZNEUPD now called to do this

!// post processing (Other modes may require more complicated post processing than mode1.)

rvec = .true.

call zneupd (rvec, 'A', select, D, V, ldv, sigma, workev, bmat, n, which,&

& nev, tol, resid, ncv, v, ldv, iparam, ipntr, workd, workl, &

& lworkl, rworkl, ierr)

!// Eigenvalues are returned in the one dimensional array D and the corresponding

!// eigenvectors are returned in the first NCONV (=IPARAM(5)) columns of the two

!// dimensional array V if requested.Otherwise, an orthogonal basis for the

invariant !// subspace corresponding to the eigenvalues in D is returned in V.

if (ierr .ne. 0) then

!// Error condition: Check the documentation of ZNEUPD.

print *, ' Error with neupd, info = ', ierr

print *, ' Check the documentation of neupd. '

else

nconv = iparam(5)

do 20 j=1, nconv

!// Compute the residual norm deter(A*x - lambda*x)for the NCONV accurately

!// computed eigenvalues and eigenvectors. (iparam(5) indicates how many are

!// accurate to the requested tolerance)

call av(nx, v(1,j), ax) call zaxpy(n, -d(j), v(1,j), 1, ax, 1)

```fortran
      rd(j,1) = dble(d(j))

      rd(j,2) = dimag(d(j))

      rd(j,3) = dznrm2(n, ax, 1)

      rd(j,3) = rd(j,3) / dlapy2(rd(j,1),rd(j,2))

20    continue

!// Display computed residuals.

      call dmout(6, nconv, 3, rd, maxncv, -6, &
      & 'Ritz values (Real, Imag) and relative residuals')

      end if

!// Print additional convergence information.

      if ( info .eq. 1) then

      print *, ' Maximum number of iterations reached.'

      else if ( info .eq. 3) then

      print *, ' No shifts could be applied during implicit &
      & Arnoldi update, try increasing NCV.'

      end if

      print *, ' Size of the matrix is ', n

      print *, ' The number of Ritz values requested is ', nev

      print *, ' The number of Arnoldi vectors generated',' (NCV) is ', ncv

      print *, ' What portion of the spectrum: ', which

      print *, ' The number of converged Ritz values is ',nconv

      print *, ' The number of Implicit Arnoldi update', &
      & ' iterations taken is ', iparam(3)

      print *, ' The number of OP*x is ', iparam(9)

      print *, ' The convergence criterion is ', tol

      end if

!// Done with program znsimp.
```

9000 continue

B.2 Fast Fourier Transform

B.2.1 Fourier Transform of Discrete Data

In this section, I follow closely the book of *Numerical Recipes: The Art of Scientific Computing* .

The Fourier transform of a function $h(t)$ or $H(f)$ are given by the following equations

$$H(f) \;=\; \int_{\infty}^{-\infty} h(t)e^{2\pi i f t}dt \tag{84}$$

$$h(t) \;=\; \int_{\infty}^{-\infty} H(f)e^{-2\pi i f t}df \tag{85}$$

In the above equations, if t is measured in seconds, then f, frequecny, is in unit of Hertz. When function $h(t)$ is sampled at evenly spaced intervals in time,suppose N consecutive values, then $h(t)$ can be specifcied as

$$h_n = h(t_n), t_n = n\Delta, n = 0, 1, 2, \ldots, N-1 \tag{86}$$

where Δ is the sampling interval. If the function is nonzero only in a finite interval of time, then the whole interval of time is supposed to be contained in the range of N points. With N numbers of input, we will be able to have the same number of output. Here, we will only estimate $H(f)$ in discrete values, N is assumed even number here.

$$f_n = \frac{n}{N\Delta}, n = -\frac{N}{2}, \ldots, \frac{N}{2} \tag{87}$$

The extreme values of n in 87 correspond to the lower and upper limits of the Nyquist critical frequecny range. It will turn out that the two extreme values of n are not independent but equal. This reduces the count to N. So the intergral of 85

can be approximated by discrete summation:

$$H(f_n) = \int_{\infty}^{-\infty} h(t)e^{2\pi ift}dt \approx \sum_{k=0}^{N-1} h_k e^{2\pi if_n t_k}\Delta = \Delta \sum_{k=0}^{N-1} h_k e^{2\pi ikn/N} = \Delta H_n \qquad (88)$$

Where $H_n = \sum_{k=0}^{N-1} h_k e^{2\pi ikn/N}$. The 88 is called the *discrete Fourier transform* of the N points of h_k.

B.2.2 Fast Fourier Transform in One and Two Dimension

The computation time for DFT is $O(N^2)$, but it can reduced to $O(Nlog_2 N)$ with the method of *Fast Fourier Transform*. The difference of computing time is huge when N is large enough, like 10^5. Here I will show the derivation of FFT by Denielson and Lanczos. They showed that a discrete Fourier transform of length N can be rewritten as the sum of two discrete Fourier transforms, each of length $N/2$. One of the two is formed from the even-numbered points of the original N, the other from the odd-numbered points. So

$$F_k = \sum_{j=0}^{N-1} e^{2\pi ijk/N} f_j \qquad (89)$$

$$= \sum_{j=0}^{N/2-1} e^{2\pi i(2j)k/N} f_{2j} + \sum_{j=0}^{N/2-1} e^{2\pi i(2j+1)k/N} f_{2j+1} \qquad (90)$$

$$= \sum_{j=0}^{N/2-1} e^{2\pi ijk/(N/2)} f_{2j} + W^k \sum_{j=0}^{N/2-1} e^{2\pi ijk/(N/2)} f_{2j+1} \qquad (91)$$

$$= F_k{}^e + W^k F_k{}^0 \qquad (92)$$

Where $W = e^{2\pi i/N}$, and $F_k{}^e$ denotes the kth component of the Fourier transform of length $N/2$ formed from the even components of the original $f'_j s$, while $F_k{}^o$ is the corresponding transform of length $N/2$ formed from the odd components. The transforms $F_k{}^e$ and $F_k{}^o$ are periodic in k with length $N/2$. So each is repeated through two cycles to obtain F_k. When this method is used recursively, we will reduce the calculation of $F_k{}^e$ to the summation of $F_k{}^{ee}$ and $F_k{}^{eo}$, which corresponding to the discrete Fourier transforms of the points which are respectively even-even and even-odd on the successive subdivisions of the data.

111

When this method is used repeatedly, the transform will be optimal when N is power of 2. With this restriction on N, we can continue applying the Danielson-Lanczos method until we have subdivided the data all the way down to transform of length 1. So it is just the identity operation that copies its one input to its output. For evey pattern of $log_2 N$ e and o, there is a one-point transform that is just one of the input number f_n

$$F_k^{eoeo...eoe} = f_n \tag{93}$$

The value n happens to be the binary value of the suquence of $eoeo \ldots eoe$. The algorithm can be listd as below: We take the original vector of f_j and rearrange it into bit-reversed order, so that the indivisual numbers are in the order bit-reversing j. Then points as given are the one-point transforms. We combine adjacent pairs to get tow-point transforms, then combine adjacent pairs of pairs to get 4-point transform, and so on, until the first and second halves of the whole data set are combined into the final transform. Each combination takes of order N operations, and there are $log_2 N$ combination, so the whole algorithm is in $O(N log_2 N)$.

Given a complex function $h(k_1, k_2)$ defined over the two dimensional grid $0 \leq k_1 \leq N_1 - 1$, $0 \leq k_2 \leq N_2 - 1$, we can defines the two dimension discrete complex function $H(n_1, n_2)$, defined over the same grid,

$$H(n_1, n_2) = \sum_{k_2=0}^{N_2-1} \sum_{k_1=0}^{N_1-1} \exp(2\pi i k_2 n_2/N_2) \exp(2\pi i k_1 n_1/N_1) h(k_1, k_2) \tag{94}$$

So the corresponding FFT is

$$
\begin{aligned}
H(n_1, n_2) &= FFT - on - index - 1(FFT - on - index - 2\left[h(k_1, k_2)\right]) &\text{(95)} \\
&= FFT - on - index - 2(FFT - on - index - 1\left[h(k_1, k_2)\right]) &\text{(96)}
\end{aligned}
$$

112

B.2.3 FFT application in the project

In our REM microscopic method, we have the electron molecule state:

$$|\Phi_L^{\text{REM}}\rangle = \int_0^{2\pi} \!\!\! ... \int_0^{2\pi} d\gamma_1 ... d\gamma_r$$

$$\times |\Psi^{\text{SEM}}(\gamma_1, ..., \gamma_r)\rangle \exp\left(i \sum_{q=1}^r \gamma_q L_q \right). \tag{97}$$

Here $L = \sum_{q=1}^r L_q$ and $|\Psi^{\text{SEM}}[\gamma]\rangle$ is the original Slater determinant with *all the single-electron wave functions of the qth ring* rotated (collectively, i.e., coherently) by the *same* azimuthal angle γ_q. The corresponding enery of REM is given by

$$E_L^{\text{REM}} = \int_0^{2\pi} h([\gamma]) e^{i[\gamma]\cdot[L]} d[\gamma] \Big/ \int_0^{2\pi} n([\gamma]) e^{i[\gamma]\cdot[L]} d[\gamma], \tag{98}$$

with the hamiltonian and overlap matrix elements $h([\gamma]) = \langle\Psi^{\text{SEM}}([0])|H|\Psi^{\text{SEM}}([\gamma])\rangle$ and $n([\gamma]) = \langle\Psi^{\text{SEM}}([0])|\Psi^{\text{SEM}}([\gamma])\rangle$, respectively, and $[\gamma]\cdot[L] = \sum_{q=1}^r \gamma_q L_q$. The SEM energies are simply given by $E_{\text{SEM}} = h([0])/n([0])$.

For electrons $2 \leq N \leq 8$, the integration of energy in 98 is one dimension, for they just forms one ring. Then we just need to restore the symmetry of one ring, though the $N = 6, 7, 8$ will have one electron in the center of the ring. As there is no symmetry restoring for one point, I used here one dimensional FFT to get the integration results. For electrons $9 \leq N$, they will form two or more rings, so I used 2D FFT for 2 rings to restore the whole symmetry, which means each ring will rotate independently. (All the FFT codes are taken from online modules). Here I choose that each parameters in the FFT that are power of 2 and larger than the maximum magic numbers of each ring. For quantum dots that forms up to 3 rings, it requires 3 dimensional FFT. Though we choose the parameters that are power of 2 for FFT and parallelize the code, it is still very slow for 3D FFT computation. For example, it requires 8 hours to get 1 enery point for 3D FFT by 32 UNIX processors. And for 2D FFT, it will require about 1 hour to get 1 energy point for 32 processors, which is reasonable to get the full spectrum when B range from $0T$ to

$8T$. But for the density calculation, it requires at least 30×30 points, approximately the same time as enery point calculation. Though the computation time is still under control, it's very time-consuming and resoure-consuming. And it is not possible for us to carry 3D FFT for full enery spectrum or density calculation. In the above integrations, we assume that each ring rotate independently. So in order to restore the whole symmetry, the dimensions of FFT equal the number of rings. For example, $N = 9$ electrons will form one ring with the configuration (1,8) or two ring configuration (2,7). We need 1D FFT for the configuration (1,8) and 2D FFT for the configuration of (2,7). And teh configuration of (2,7) has lower energy, a more stable state. Accidently, when I try to test my results for 2D FFT, I decide to form 1D FFT for the configuration (2,7). The eneries turns out to be exactly the same for 2D FFT. Then I calculated the energies by 1D FFT for electrons up to 29, which has already formed 3 rings. Thereafter I found that all the energies by 1D FFT are the same for 2D FFT or 3D FFT, except for $N = 16$ and $N = 19$. And for the density(just for 2 rings), the results of 1D FFT and 2D FFT are the same with no exceptions. According to the above results, I can save a lot of computation time and make it possible to handle electrons up to 34 with 64 processors. Though there is no proved explanations, we can treat all the rings rotate collectively in the same direction instead of rotating independently, so we just need to restore one symmetry. As for $N = 16$ and $N = 19$, they form the configuration of (1,5,10) and (1,6,12). The number of electrons in outer ring is exactly twice the number of inner ring, so the magic number of outer ring, 12 , is twice the magic number of inner ring,6. This configuration will mix up each magic number given a specific total magic number and cause the energy higher. But for other number of electrons, there is no such condition.(Above explanation is just our assumption)

REFERENCES

[1] L.P. Kouwenhoven, D.G. Austing and S. Tarucha Rep. Prog. Phys. **64**, 701, (2001)

[2] M. Reed Sci.Am. **268**, 118, (1993); R.C. Ashoori Nature **379**, 413, (1996)

[3] M. Alonso and E.J. Finn, Quantum and Statistical Physics (Addison-Wesley) (1968)

[4] D.G. Austing, T. Honda, Y. Tokura and S. Tarucha Japan. J. Appl. Phys. **34**, 1320 (1995)

[5] S. Tarucha, D.G. Austing , T. Honda, R.J. van der Hage and L.P. Kouwenhoven Phys. Rev. Lett **77**, 3613 (1996)

[6] K. Keren, A. Stern and U. Sivan Preprint cond-mat/9903377 (1999)

[7] See webpage http://vortex.tn.tudelft.nl/ (03/2007)

[8] H. Grabert and M.H. Deroret Single Charge Tunnelling(New York: Plenum) (1991);
Jacak : Harylak P and Wojs A Quantum Dots(Berling: Springer) (1998)

[9] G.J. Iafrate, K. Hess, J.B. Krieger and M. Macucci Phys. Rev. B **52** , 10737 (1995)

[10] L.P. Kouwenhoven, D.G. Austing, and S. Tarucha, Rep. Prog. Phys. **64**, 701 (2001).

[11] M. Ciorga, A.S. Sachrajda, P. Hawrylak, C. Gould, P. Zawadzki, S. Jullian, Y. Feng, and Z. Wasilewski, Phys. Rev. B **61**, R16315 (2000).

[12] D.M. Zumbühl, C.M. Marcus, M.P. Hanson, and A.C. Gossard, Phys. Rev. Lett. **93**, 256801 (2004).

[13] P.A. Maksym, H. Imamura, G.P. Mallon, and H. Aoki, J. Phys.: Condens. Matter **12**, R299 (2000).

[14] W.Y. Ruan and H.-F. Cheung, J. Phys.: Condens. Matter **11**, 435 (1999).

[15] W.Y. Ruan, K.S. Chan, H.P. Ho, and E.Y.B. Pun, J. Phys.: Condens. Matter **12**, 3911 (2000).

[16] C. Yannouleas and U. Landman, (a) Phys. Rev. B **66**, 115315 (2002); (b) Phys. Rev. B **68**, 035326 (2003); (c) Phys. Rev. B **69**, 113306 (2004).

[17] M.B. Tavernier, E. Anisimovas, F. M. Peeters, B. Szafran, J. Adamowski, and S. Bednarek, Phys. Rev. B **68**, 205305 (2003).

[18] C. Yannouleas and U. Landman, (a) Phys. Rev. Lett. **82**, 5325 (1999); (b) J. Phys.: Condens. Matter **14**, L591 (2002); (c) Phys. Rev. B **68**, 035325 (2003).

[19] S.R.E. Yang, A.H. MacDonald, and M.D. Johnson, Phys. Rev. Lett. **71**, 3194 (1993).

[20] A. W'ojs and P. Hawrylak, Phys. Rev. B **56**, 13 227 (1997).

[21] P. Hawrylak and D. Pfannkuche, Phys. Rev. Lett. **70**, 485 (1993)

[22] Detailed *ab initio* calculations – involving EXD for three Landau levels and variational Monte Carlo methods [see A.D. Güclü and C.J. Umrigar, Phys. Rev. B **72**, 045309 (2005)] – for $N = 4$ and $N = 6$ electrons for a confinement of 3.32 meV and a range of magnetic fields above 3 T have concluded that only fully polarized states with magic angular momenta are involved in the transition from the MDD ($\nu = 1$) to the subsequent ground states (i.e., for $\nu < 1$) as B

increases, when the effective Landé factor takes the value for GaAs, $g^* = -0.44$. This finding is in agreement with our treatment of considering only fully polarized states for all values $\nu \leq 1$. [In our results presented in this paper for fully polarized states, the (non-vanishing) Zeeman energy contribution was not included. However, this contribution can be easily added.] We note that the value of 3.32 meV used in the above study falls within the range of currently achievable experimental confinements (as is our value of 3.60 meV). We further note that our method can address the case of non-fully-polarized states, as discussed for two electrons in Ref. 9(b). Such non-fully-polarized states are interesting in their own right and are necessary for weak confinements and weak magnetic fields [see, e.g., M-C. Cha and S.R.E. Yang, Phys. Rev. B **67**, 205312 (2003)], but they fall outside the scope of our present paper.

[23] A. Harju, S. Siljamäki, and R.M. Nieminen, Phys. Rev. B **60**, 1807 (1999).

[24] H. Saarikoski, A. Harju, M.J. Puska, and R.M. Nieminen, Phys. Rev. Lett. **93**, 116802 (2004).

[25] C. Ellenberger, T. Ihn, C. Yannouleas, U. Landman, K. Ensslin, D. Driscoll, and A.C. Gossard, Phys. Rev. Lett. **96**, 126806 (2006).

[26] D.M. Zümbuhl, C.M. Marcus, M.P. Hanson, and A.C. Gossard, Phys. Rev. Lett. **93**, 256801 (2004).

[27] S. Tarucha, D.G. Austing, T. Honda, R.J. van der Hage, and L.P. Kouwenhoven, Phys. Rev. Lett. **77**, 3613 (1996).

[28] M. Ciorga, A.S. Sachrajda, P. Hawrylak, C. Gould, P. Zawadzki, S. Jullian, Y. Feng, and Z. Wasilewski, Phys. Rev. B **61** R16315 (2000).

[29] F. Meier, J. Levy, and D. Loss, Phys. Rev. Lett. **90**, 047901 (2003).

[30] R. Woodworth, A. Mizel, and D.A. Lidar, J. Phys.: Condens. Matter **18**, S721 (2006).

[31] V.N. Gorbachev and A.I. Trubilko, Laser Phys. Lett. **3**, 59 (2006).

[32] P. Hawrylak, Phys. Rev. Lett. **71** 3347 (1993).

[33] S.A. Mikhailov and N.A. Savostianova, Phys. Rev. B **66**, 033307 (2002).

[34] W. Dür, G. Vidal, and J.I. Cirac, Phys. Rev. A **62**, 062314 (2000).

[35] V. Coffman, J. Kundu, and W.K. Wootters, Phys. Rev. A **61**, 052306 (2000).

[36] C.F. Roos, M. Riebe, H. Häffner, W. Hänsel, J. Benhelm, G.P.T. Lancaster, C. Becher, F. Schmidt-Kaler, and R. Blatt, Science **304**, 1478 (2004).

[37] A.H. MacDonald, S.R.E. Yang, and M.D. Johnson, Aust. J. Phys. **46**, 345 (1993).

[38] A.F. Andreev and I.M. Lifshitz, Sov. Phys. JETP **29**, 1107 (1969).

[39] G.V. Chester, Phys. Rev. A **2**, 256 (1970).

[40] A.J. Leggett, Phys. Rev. Lett. **25**, 1543 (1970).

[41] E. Kim and M.H.W. Chan, Nature **427**, 225 (2004); Science **305**, 1941 (2004).

[42] T. Leggett, Science **305**, 1921 (2004).

[43] M. Tiwari and A. Datta, Phys. Rev. Lett. **94**, 155302 (2005).

[44] N. Prokof'ev and B. Svistunov, Phys. Rev. Lett. **94**, 165301 (2005).

[45] D.M. Ceperley and B. Bernu, Phys. Rev. Lett. **93**, 155303 (2004).

[46] H. Falakshahi and X. Waintal, Phys. Rev. Lett. **94**, 046801 (2005).

[47] M. Kong, B. Partoens, and F.M. Peeters, Phys. Rev. E **65**, 046602 (2002).

[48] Y. Li, C. Yannouleas, and U. Landman, Phys. Rev. B **73**, 075301 (2006).

[49] D.J. Yoshioka and P.A. Lee, Phys. Rev. B **27**, 4986 (1983).

[50] C. Yannouleas and U. Landman, Phys. Rev. B **70**, 235319 (2004).

[51] For multiple rings, see Ref. [16]. For the simpler cases of $(0, N)$ or $(1, N - 1)$ rings, see, e.g., W.Y. Ruan, Y.Y. Liu, C.G. Bao, and Z.Q. Zhang, Phys. Rev. Lett. **51**, 7942 (1995) and Ref. [13].

[52] G.S. Jeon, C.-C. Chang, and J.K. Jain, Phys. Rev. B **69**, R241304 (2004).

[53] The REM energies are slightly lower than the EXD ones in several subranges. According to the Rayleigh-Ritz variational theorem, this indicates that the hyperspherical-harmonics calculation of Ref. [14] did not converge fully in these subranges.

[54] P.-O. Löwdin, Rev. Mod. Phys. **34**, 520 (1962).

[55] B. Szafran, S. Bednarek, and J. Adamowski, J. Phys.: Condens. Matter **15**, 4189 (2003).

[56] In addition, Ref. [55] performs the UHF variation within the LLL. As a result, the electron-molecule configurations found therein beyond the MDD resemble those appearing in EXD calculations in the LLL. For $N \leq 14$, however, proper consideration of higher Landau levels yields different polygonal-ring configurations.

[57] Previous studies that used the approximation characterized as LLL in our paper did not specify magnetic-field lower bounds for its applicability. To do so, one needs to be able to compare the LLL approximation to another "better"

approximation. In our paper, the REM approximation is a "better" approximation, since it is a variational method that yields ground-state energies lower than those of the LLL approximation. From comparisons of the REM and LLL energies in our Fig. 4 (N=9) and from an analysis of the ground-state angular momenta (see corresponding Table II and text), it can be seen that the regime of validity of the LLL approximation does not extend *above* the fractional filling $\nu = 1/5$. Furthermore, to reach this conclusion, one does not need to consider partially polarized or non-polarized states. Consideration of fully polarized states is sufficient because of (1) the rather large magnetic field associated with the $\nu = 1/5$ ground state compared to the magnetic field associated with the MDD ($\nu = 1$), and (2) the fact that the lowering of the REM energies is due to a quenching of the matrix elements of the Coulomb force between displaced Gaussians as the magnetic field decreases and this effect is independent of the spin polarization.

[58] S.-R. Eric Yang and A.H. MacDonald, Phys. Rev. B **66**, 041304 (2002).

[59] M. Toreblad, M. Borgh, M. Koskinen, M. Manninen, and S.M. Reimann, Phys. Rev. Lett. **93**, 090407 (2004); M. Toreblad, Y. Yu, S.M. Reimann, M. Koskinen, and M. Manninen, Phys. Rev. Lett. **93**, 090407 (2004).

[60] See in particular the plots labeled as (6,2) in figures 6 and 7 of Ref. [17].

[61] The composite-fermion wave functions for the main fractions $\nu = 1/(2j + 1)$ (i.e., the Laughlin functions) fail to exhibit an internal crystalline structure in the LLL, in contrast to findings fron exact diagonalization and the rotating electron molecule theory (discussed here and in earlier publications, see Ref. [50]). Away from the main fractions, it was reported most recently [see G.S. Jeon, C.C. Chang, and J.K. Jain, J. Phys.: Condens. Matter **16**, L271 (2004)] that some CF functions [e.g., for $N = 19$ and $L = 1845$ and $N = 19$ and

$L = 3555$] may exhibit CPDs resembling the REM and EXD conditional probability distributions. The physical interpretation of independently rotating polygonal rings was not proposed in the above paper. Instead, an interpretation of "melting" was suggested following A.V. Filinov *et al.* [Phys. Rev. Lett. **86**, 3851 (2001)] who expanded the earlier results of Ref. 9(a). We note that the "melting" interpretation is inconsistent with the behavior of the CPDs at strong B, since (i) A.V. Filinov *et al.* considered Wigner molecules at *zero* magnetic field and (ii) the azimuthal "melting" they describe appears simultaneously in all polygonal rings, and it is independent of the choice of the observation point $\mathbf{r}_0$ [see Eq. (14)].

[62] P.A. Maksym, Phys. Rev. B **53**, 10 871 (1996).

[63] For the classical equilibrium structure of $N = 17$ point charges, the inner radius is $0.9696R_0$, while the outer one is $1.8418R_0$.[47]

[64] R.B. Lehoucq, D.C. Sorensen, and C. Yang, *ARPACK Users' Guide: Solution of Large-Scale Eigenvalue Problems with Implicitly Restarted Arnoldi Methods* (SIAM, Philadelphia, 1998).

[65] A. Szabo and N.S. Ostlund, *Modern Quantum Chemistry* (McGraw-Hill, New York, 1989).

[66] When the orbitals $\varphi_i(\mathbf{r})$ are eigenfunctions of a 2D oscillator, analytic expressions for the Coulomb matrix elements in Eq. (36) have been reported by, e.g., S.M. Girvin and T. Jach [Phys. Rev. B **28**, 4506 (1983)] for a circular oscillator, and by J. Kyriakidis and S.J. Penney [Phys. Rev. B **71**, 125332 (2005)] for an anisotropic one.

[67] L.P. Kouwenhoven, D.G. Austing, and S. Tarucha, Rep. Prog. Phys. **64**, 701 (2001).

[68] J. Kyriakidis, M. Pioro-Ladriere, M. Ciorga, A.S. Sachrajda, and P. Hawrylak, Phys. Rev. B **66**, 035320 (2002).

[69] J. Kyriakidis and G. Burkard, Phys. Rev. B **75**, 115324 (2007).

[70] D.G. Austing, APS March 2007 meeting in Denver.

[71] R. Pauncz, *The Construction of Spin Eigenfunctions: An Excercise Book V* (Kluwer Academic, Plenum Publishers, New York, 2000).

[72] A.D. Klironomos, J.S. Meyer, and K.A. Matveev, Europhys. Lett. **74**, 679 (2006).

[73] G. Piacente, I.V. Schweigert, J.J. Betouras, and F.M. Peeters, Phys. Rev. B **69**, 045324 (2004).

[74] R. Paskauskas and L. You, Phys. Rev. A **64**, 042310 (2001).

[75] For EXD calculations of the von Neumann entropy in a two-electron anisotropic quantum dot, see T. Ihn, C. Ellenberger, C. Yannouleas, U. Landman, K. Ensslin, D. Driscoll, A.C. Gossard, arXiv:cond-mat/0610019v2.

[76] C. Yannouleas and U. Landman, Phys. Rev. B **61**, 15895 (2000).

[77] P. Ring and P. Schuck, *The Nuclear Many-body Problem* (Springer, New York, 1980) Ch. 11, and references therein.

[78] C. Yannouleas and U. Landman, Phys. Rev. B **68**, 035325 (2003).

[79] C. Yannouleas and U. Landman, Eur. Phys. J. D **16**, 373 (2001).

[80] C. Yannouleas and U. Landman, Int. J. Quantum Chem. **90**, 699 (2002).

[81] K. Maki and X. Zotos, Phys. Rev. B **28**, 4349 (1983).

[82] V.M. Bedanov and F.M. Peeters, Phys. Rev. B **49**, 2667 (1994).

[83] F. Bolton and U. Rössler, Superlatt. Microstruct. **13**, 139 (1993).

[84] The definition $z \equiv x + \imath y$ is associated with positive angular momenta for the single-particle states in the lowest Landau level. In Ref. [16], we used $z \equiv x - \imath y$ and negative single-particle angular momenta in the lowest Landau level. The final expressions for the trial wave functions do not depend on these choices.

[85] Both the finite-size REM molecule and several sophisticated bulk Wigner crystal (BWC) approaches at high B (listed at the end of this footnote) start with a single-determinantal UHF wave function constructed out of the orbitals in Eq. (54), and both do improve it by introducing additional correlations; however, the nature of these correlations is quite different between the REM and the BWC approaches. Indeed, due the the finite-size of the system, the REM approach includes correlations associated with fluctuations in the *azimuthal* angle (see Ref. [16] and Ref. [78]); these correlations arise from the restoration of the circular symmetry and result in states with good total angular momenta (in particular *magic* angular momenta. Naturally, in the BWC approaches, angular-momentum conservation and magic angular momenta are not considered; for example, Lam and Girvin include correlations from *vibrational*-type fluctuations of the BWC that are more in tune with the expected translational invariance of a bulk system. As a result, the REM exhibits drastically different properties from the properties of an N-electron piece of the bulk Wigner crystal. Rather, the REM wave functions exhibit properties associated with the incompressible magic-angular-momenta states in the spectra of QD's, which are finite-size *precursors* to the "correlated-liquid" fractional quantum Hall states of the bulk. For sophisticated BWC approaches at high B, see, e.g., P.K. Lam and S.M. Girvin, Phys. Rev. B **30**, 473 (1984); H. Yi and H.A. Fertig, Phys. Rev. B **58**, 4019 (1998).

[86] F. Duan and J. Guojun: Introduction to condensed matter physics (Nanjing University, China)

[87] Y. Saad. Numerical Methods for Large Eigenvalue Problems. Halsted Press, 1992.